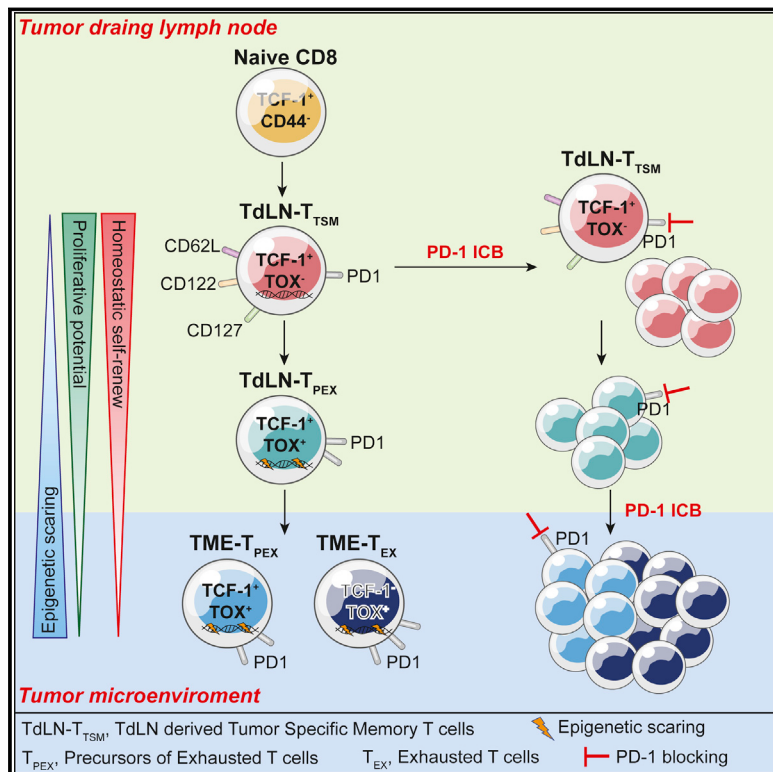


The primordial differentiation of tumor-specific memory CD8⁺ T cells as bona fide responders to PD-1/PD-L1 blockade in draining lymph nodes

Graphical abstract



Authors

Qizhao Huang, Xia Wu, Zhiming Wang, ..., Lifan Xu, Zhonghui Tang, Lilin Ye

Correspondence

sunbc@nju.edu.cn (B.S.),
xlfoto@sina.com (L.X.),
tangzhh99@mail.sysu.edu.cn (Z.T.),
yelilinlcmv@tmmu.edu.cn (L.Y.)

In brief

Huang et al. demonstrate different functional states of tumor-reactive CD8⁺ T cells in the TdLN where TCF-1⁺TOX⁻ CD8⁺ T cells are bona fide memory T cells and function as the genuine responders to PD-1/PD-L1 ICB.

Highlights

- TdLN-T_{TSM} cells are bona fide memory T cells
- Exhaustion-associated epigenetic scarring marks T_{PEX} but not TdLN-T_{TSM} cells
- Adoptive transfer of TdLN-T_{TSM} represents a promising immunotherapy strategy
- TdLN-T_{TSM} cells are primary responders to PD-1/PD-L1 ICB



Article

The primordial differentiation of tumor-specific memory CD8⁺ T cells as bona fide responders to PD-1/PD-L1 blockade in draining lymph nodes

Qizhao Huang,^{1,7,8} Xia Wu,^{2,8} Zhiming Wang,^{3,8} Xiangyu Chen,^{1,8} Lisha Wang,³ Yijun Lu,⁴ Dan Xiong,² Qiao Liu,³ Yuhan Tian,² Huayu Lin,³ Junyi Guo,⁵ Shuqiong Wen,⁵ Wei Dong,² Xiaofan Yang,¹ Yuchen Yuan,² Zhengliang Yue,³ Shun Lei,³ Qing Wu,³ Ling Ran,³ Luoyingzi Xie,³ Yifei Wang,¹ Leiqiong Gao,¹ Qin Tian,³ Xinyuan Zhou,³ Beicheng Sun,^{4,6,*} Lifan Xu,^{3,*} Zhonghui Tang,^{2,*} and Lilin Ye^{3,7,9,*}

¹ Provincial Key Laboratory of Immune Regulation and Immunotherapy, School of Laboratory Medicine and Biotechnology, Southern Medical University, Guangzhou 510515, China

²Zhongshan School of Medicine, Sun Yat-sen University, Guangzhou 510080, China

³Institute of Immunology, Third Military Medical University, Chongqing 400038, China

⁴Department of Hepatobiliary Surgery, Affiliated Drum Tower Hospital, Medical School of Nanjing University, Nanjing 210008, China

⁵Guanghua School of Stomatology, Guangdong Provincial Key Laboratory of Stomatology, Stomatological Hospital, Sun Yat-Sen University, Guangzhou 510080, China

⁶Department of Hepatobiliary Surgery, The First Affiliated Hospital of Anhui Medical University, Hefei 230022, China

⁷Changping Laboratory, 102206 Beijing, China

⁸These authors contributed equally

⁹Lead contact

*Correspondence: sunbc@nju.edu.cn (B.S.), xlftofu@sina.com (L.X.), tangzhh99@mail.sysu.edu.cn (Z.T.), yelilinlcmv@tmmu.edu.cn (L.Y.)

<https://doi.org/10.1016/j.cell.2022.09.020>

SUMMARY

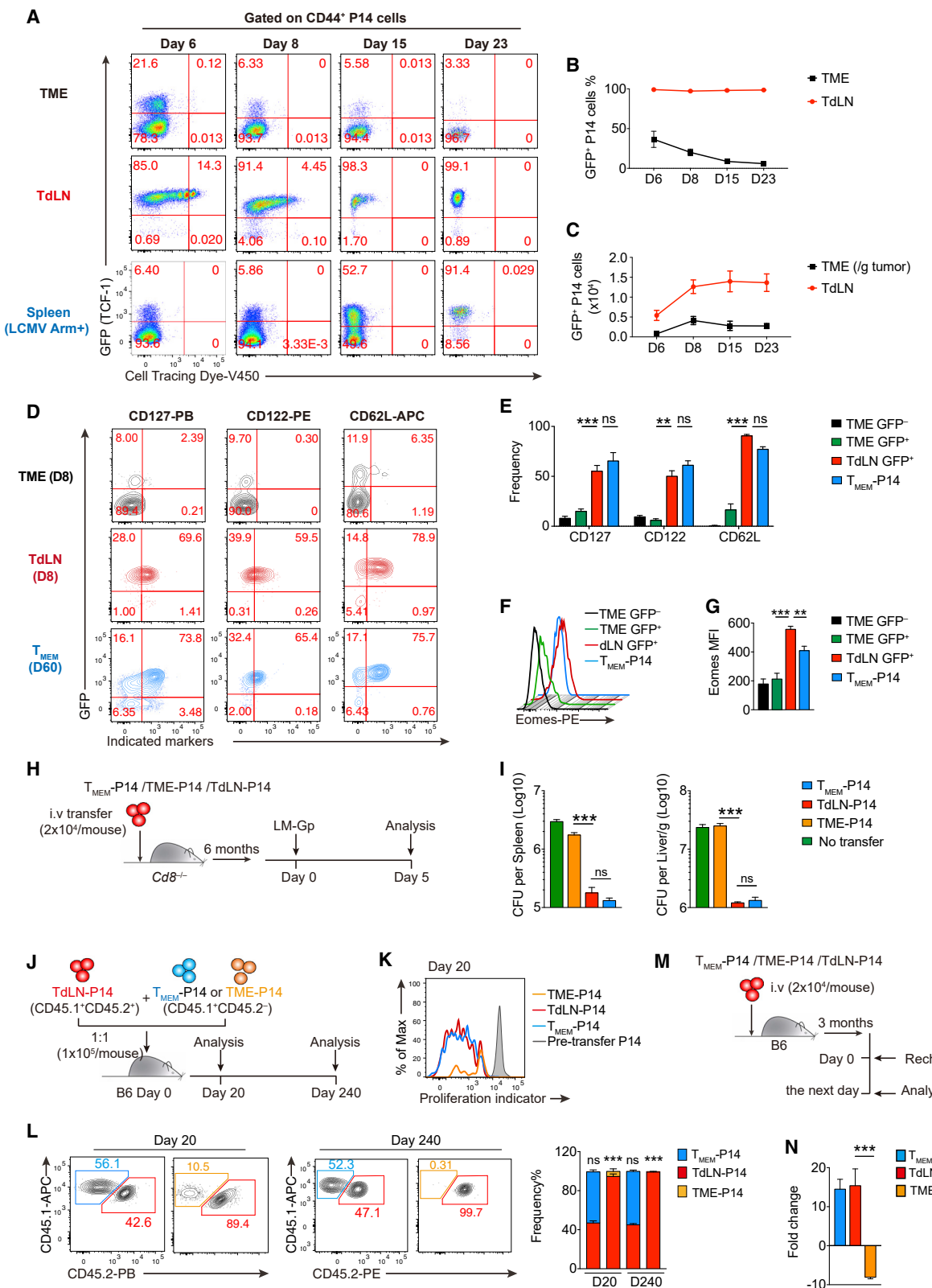
Blocking PD-1/PD-L1 signaling transforms cancer therapy and is assumed to unleash exhausted tumor-reactive CD8⁺ T cells in the tumor microenvironment (TME). However, recent studies have also indicated that the systemic tumor-reactive CD8⁺ T cells may respond to PD-1/PD-L1 immunotherapy. These discrepancies highlight the importance of further defining tumor-specific CD8⁺ T cell responders to PD-1/PD-L1 blockade. Here, using multiple preclinical tumor models, we revealed that a subset of tumor-specific CD8⁺ cells in the tumor draining lymph nodes (TdLN) was not functionally exhausted but exhibited canonical memory characteristics. TdLN-derived tumor-specific memory (T_{TSM}) cells established memory-associated epigenetic program early during tumorigenesis. More importantly, TdLN-T_{TSM} cells exhibited superior anti-tumor therapeutic efficacy after adoptive transfer and were characterized as bona fide responders to PD-1/PD-L1 blockade. These findings highlight that TdLN-T_{TSM} cells could be harnessed to potentiate anti-tumor immunotherapy.

INTRODUCTION

The long-term persistence by antigen independent self-renewal, potent proliferative burst and rapid conversion into effector CD8⁺ T cells upon antigen reencounter constitute the canonical characteristics of memory CD8⁺ T cells developed from acute viral infection (Ahmed and Gray, 1996; Kaech and Wherry, 2007). However, chronic viral infection or cancer generally drives the differentiation of exhausted CD8⁺ T cells, which lose memory differentiation potential and exhibit hierarchical functional deficits (McLane et al., 2019; Philip and Schietinger, 2022). Concomitantly, exhausted CD8⁺ T cells upregulate an array of co-inhibitory receptors, such as PD-1, Tim-3, and TIGIT (McLane et al., 2019; Wherry, 2011) and establish a unique epigenetic program with irreversible epigenetic scars at gene loci associated with exhaustion, such as *Tox* and *Pdcd1* (Abdel-Hakeem et al., 2021; Philip and Schietinger, 2022; Tonnerre et al., 2021; Yates

et al., 2021). Immune-checkpoint blockade (ICB) targeting the PD-1/PD-L1 pathway mediates durable remissions in a subset of cancer patients, with these effects generally attributed to the reversal of CD8⁺ T cell exhaustion in tumor microenvironment (TME) (Brahmer et al., 2012; Hashimoto et al., 2018; McLane et al., 2019; Sharma and Allison, 2015; Topalian et al., 2012). However, not all exhausted CD8⁺ T cells can respond to PD-1/PD-L1 ICB (Kallies et al., 2020). Exhausted CD8⁺ T cells within the TME are highly heterogeneous, at least comprising subsets of progenitors of exhausted T (T_{PEX}) cells and terminally exhausted CD8⁺ T (T_{EX}) cells (He et al., 2016; Im et al., 2016; Kurtulus et al., 2018; Leong et al., 2016; Siddiqui et al., 2019; Utzschneider et al., 2016; Wu et al., 2016). Although several studies have indicated that transcription factor (TF) TCF-1-expressing T_{PEX} cells in TME are likely primary responders to PD-1/PD-L1 ICB (Kurtulus et al., 2018; Miller et al., 2019; Sade-Feldman et al., 2018; Siddiqui et al., 2019), recent accumulating evidence





(legend on next page)

also highlights the potential role of systemic CD8⁺ T cells in responding to PD-1/PD-L1 ICB (Chamoto et al., 2017; Spitzer et al., 2017; Wu et al., 2020; Yost et al., 2019).

The draining lymph nodes (dLN) accommodate systemic CD8⁺ T cell responses, which have been implicated in the efficacy of PD-1/PD-L1 ICB in tumors (Buchwald et al., 2020; Chamoto et al., 2017; Dammeijer et al., 2020; Fransen et al., 2018). However, in tumor dLN (TdLN), the differentiation state of tumor-reactive CD8⁺ T cells and their potential responses to ICB remain largely unknown.

RESULTS

Memory features of tumor-specific CD8⁺ T cells in TdLN

To characterize the differentiation of tumor-specific CD8⁺ T cells in TdLN, C57BL/6J (hereafter referred to as B6) mice were subcutaneously engrafted with B16F10 cells expressing the lymphocytic choriomeningitis virus (LCMV) glycoprotein (hereafter referred to as B16.Gp cells). Then, naive P14 cells (CD44⁻GFP⁺, GFP indicating TCF-1 expression) harboring transgenic TCRs specific to H-2D^b Gp33-41 epitope from P14-Tcf7 (encoding TCF-1 protein)-GFP-P14 reporter mice (Figure S1A) were adoptively transferred and activated CD44⁺ P14 cells (Figure S1B) were analyzed longitudinally. Notably, nearly all activated P14 cells in the TdLN exhibited high levels of the TF TCF-1 expression at all time points examined (Figures 1A and 1B). Furthermore, the number of TCF-1⁺ P14 cells in the TdLN reached a peak on D8 post cell transfer and remained steady afterward (Figure 1C).

Besides naive T cells, memory CD8⁺ T cells also abundantly express TCF-1 (Zhao et al., 2022; Zhou et al., 2010). We next examined whether tumor-specific TCF1⁺CD8⁺ T cells in the TdLN possessed certain characteristics of memory T (T_{MEM}) cells. Remarkably, TCF-1-expressing GFP⁺P14 cells in the TdLN expressed canonical T_{MEM}-associated markers, including IL7R α (CD127), IL2R β (CD122) and CD62L, while P14 cells from the TME, including TCF-1⁺T_{PEX} cells, barely expressed these memory signatures (Figures 1D and 1E). Further-

more, the abundance of memory related TF Eomes was even higher in TdLN-P14 cells than in conventional memory counterparts (Figures 1F and 1G).

Moreover, TdLN-derived P14 cells produced comparable TNF- α , IFN- γ , and CD107 production to conventional memory P14 cells upon rechallenge with recombinant *Listeria monocytogenes* expressing the LCMV-GP₃₃₋₄₁ epitope (Lm-Gp₃₃₋₄₁), while TME-derived P14 cells showed lower cytokine production and degranulation (Figure S1C). Consistently, we found that TdLN-derived P14 cells conferred similar protective immunity as their conventional memory counterparts upon Lm-Gp₃₃₋₄₁ rechallenge, while TME-derived P14 cells failed to provide robust protection to recipients (Figures 1H and 1I).

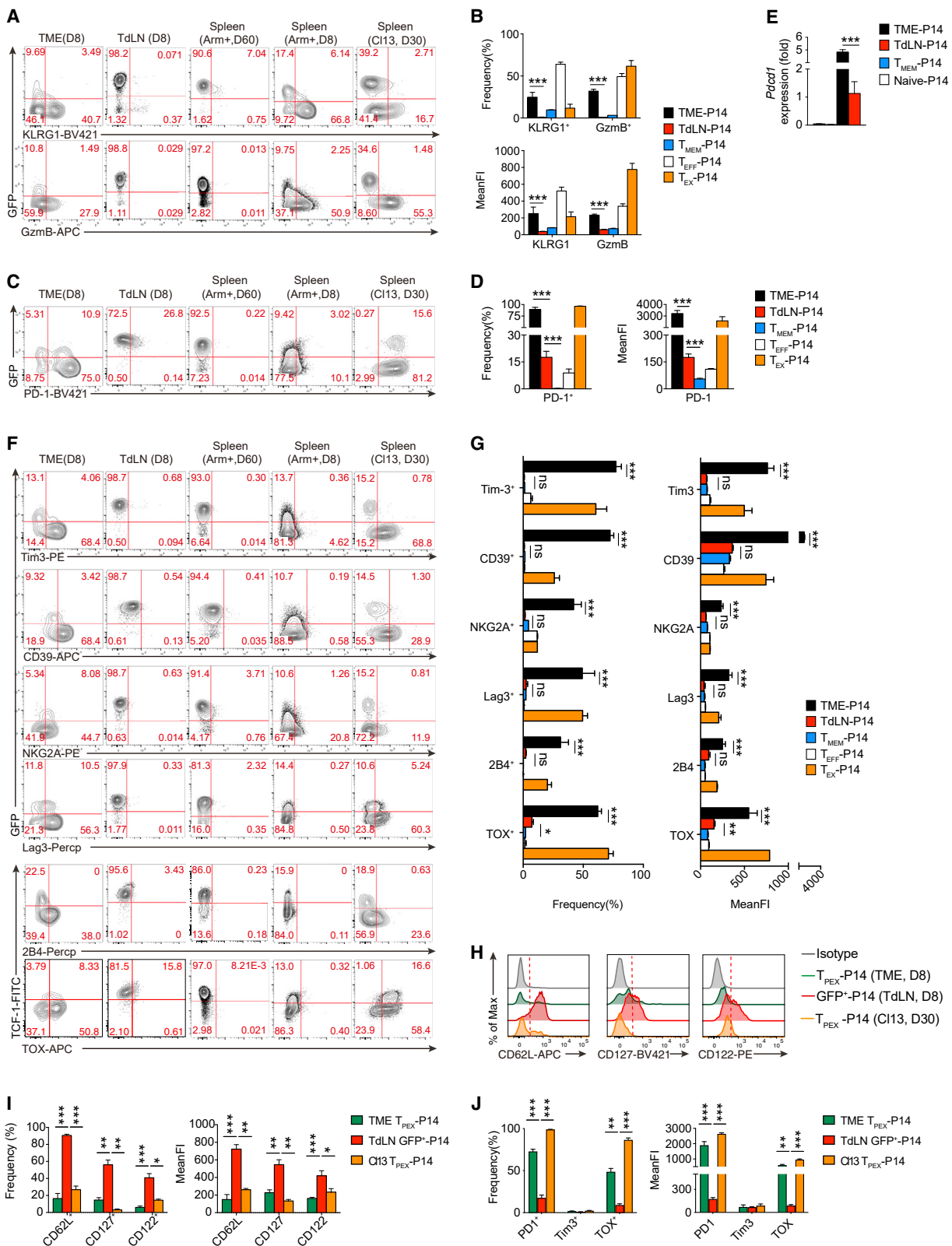
Long-term persistence and potent proliferative burst upon antigen reencounter, two fundamental features of T_{MEM} cells, may account for the protective immunity mediated by TdLN-derived P14 cells. To test this point, we co-transferred cell tracer-labeled TdLN-derived P14 cells (CD45.1⁺CD45.2⁺) with TME-derived P14 cells (CD45.1⁺CD45.2⁻) or with conventional T_{MEM} P14 cells (CD45.1⁺CD45.2⁻) into naive recipients (Figure 1J). On day 20 post transfer, we found that TdLN-derived P14 cells and T_{MEM} P14 cells underwent similar homeostatic proliferation, while TME-derived counterparts exhibited minimal homeostatic proliferation (Figure 1K). Consequently, the ratio between TdLN-derived P14 cells and T_{MEM} P14 cells was maintained approximately at 1:1 ratio on both day 20 and day 240, while TME-derived P14 cells almost vanished on day 240 post transfer (Figure 1L). Next, we sought to examine whether TdLN-derived P14 cells can undergo a proliferative burst upon antigenic re-stimulation. To this end, we sorted TdLN-derived P14 cells, TME-derived P14 cells, and T_{MEM} P14 cells and transferred them separately into naive B6 recipients, followed by LCMV Armstrong strain (LCMV-Arm⁺) rechallenge after resting for 3 months (Figure 1M). We visualized approximately 15-fold increase in the number of TdLN-derived P14 cells and T_{MEM} P14 cells; however, TME-derived P14 cells were unable to expand upon rechallenge (Figure 1N). Collectively, these results demonstrated that TdLN-derived P14 cells phenotypically and functionally resembled canonical T_{MEM} cells.

Figure 1. Tumor-specific CD8⁺ T cells in tumor-draining LN acquire features of memory T cells

- (A) Flow-cytometry analyses of TCF-1 expression (GFP) versus cell proliferation tracing dye in the TME, TdLN, and Arm⁺ infection derived P14 cells at indicated time points. Gated on donor-derived CD44⁺ P14 cells.
- (B) Frequencies of GFP⁺P14 cells relative to CD44⁺ P14 population in the TME (black) and TdLN (red). n = 4 for each time point.
- (C) Number of GFP⁺ P14 cells in the TdLN (red) and tumor per gram (g tumor) (black). n = 4 for each time point.
- (D) Flow-cytometry plots of the co-expression of TCF-1 (GFP) with different memory T cell associated markers in P14 cells from the TME, TdLN (8 days post P14 transfer) and day 60 memory P14 cells (T_{MEM}).
- (E) The percentage of each marker in the indicated subsets of P14 cells as in (D). n ≥ 4 (TME-GFP⁺, TME-GFP⁻, TdLN-GFP⁺); n = 3 (T_{MEM}-P14).
- (F) FACS analyses of Eomes expression in indicated populations of P14 cells.
- (G) The MFIs (mean fluorescence intensity) of Eomes in each population. n ≥ 5 (TME-GFP⁺, TME-GFP⁻, TdLN-GFP⁺); n = 3 (T_{MEM}-P14).
- (H and I) Listeria protection assay. (H) Experiment design. (I) Bacteria loads of Lm-Gp in the spleen (n = 4/group) and liver/g (n = 4/group) of Cd8^{-/-} mice transferred with different donor cells (2 × 10⁴/mice), day 5 post infection, (p.i.); CFU, colony-forming unit.
- (J–L) Long-term persistence of P14 cells from tumor-bearing or Arm⁺-infected mice. (J) Experiment design. (K) Flow-cytometry analyses of the dilution pattern of the cell proliferation dye on gated donor P14 cells at day 20. (L) Flow-cytometry analyses of TdLN-P14 (CD45.1⁺CD45.2⁺, gated with red line) versus T_{MEM} (CD45.1⁺CD45.2⁻, gated with blue line) or TME-P14 cells (CD45.1⁺CD45.2⁻, gated with yellow line) in the spleen of the same host mouse, at day 20 (left) and day 240 (right) post cell transfer. Frequency of each population is summarized beside. n = 4 for each group.
- (M and N) Recall assay. (M) Experiment design. (N) Fold changes relatively to initial cell number of each group (n = 4/group).

p < 0.01, *p < 0.001, ns stands for not significant, one-way ANOVA (E, G, I, L, and N) or two-way ANOVA analysis (B and C). Data are representative of ≥2 independent experiments (mean ± SEM).

See also Figure S1.



(legend on next page)

TdLN-residing tumor-specific TCF1⁺ CD8⁺ T cells are distinct from T_{PEX} cells in TME

Furthermore, we noted that both TdLN-derived P14 cells and T_{MEM} P14 cells lacked effector molecules KLRG1 and granzyme B expression (Figures 2A and 2B). Compared with classic T_{MEM} cells, TdLN-derived P14 cells maintained a low level of PD-1 expression (Figures 2C–2E). However, they scarcely expressed other exhaustion-associated molecules, such as Tim-3, CD39, and Lag3 (Figures 2F and 2G).

Compared with TdLN-derived P14 cells, TCF-1⁺ T_{PEX} P14 cells differentiated either in the TME or during chronic infection barely expressed memory markers CD122, CD127, and CD62L but substantially expressed key exhaustion markers PD-1 and TOX (Figures 2H–2J). These results together demonstrated that TdLN-derived tumor-specific CD8⁺ T cells were phenotypically different from TME-T_{PEX} cells.

Furthermore, we validated that the initial transfer of different number of naive P14 cells (GFP⁺CD44⁻) prior to B16.Gp cell engraftment had little influence on the memory properties of TdLN-derived P14 cells (Figures S1D–S1H). We further confirmed that non-TCR-transgenic, endogenous tumor epitope (H-2D^b GP_{33–41}) specific CD8⁺ T cells in the TdLNs also displayed typical memory phenotypes (Figures S1I and S1J).

Transcriptional and epigenetic profiling of TdLN-derived tumor-specific TCF1⁺CD8⁺ T cells

To define the unique molecular traits of TdLN-derived tumor-specific CD8⁺ T cells, we performed single-cell RNA sequencing (scRNA-seq) of P14 cells from the TdLNs and TME of B16.Gp engrafted mice. Conventional T_{MEM} P14 cells (day 200 post-acute LCMV-Arm⁺ infection) and exhausted GP_{33–41} tetramer-positive CD8⁺ T cells (D28 post Cl13 infection, GEO: GSE122713) (Miller et al., 2019) were introduced as controls. Additionally, the external scRNA-seq datasets (GEO: GSE182509) of GP_{33–41} specific CD8⁺ T cells from TdLNs at 8- or 17-week post tumor induction (LN-8W/17W) in a lentivirus induced KRAS mutant and P53 loss associated lung adenocarcinoma (K/P LUAD) model (Connolly et al., 2021) were also incorporated. Totally, 22,376 cells from 6 samples were further categorized into seven major clusters (Figures 3A, 3B, S2A, and S2B). We found that TdLN-P14 cells and T_{MEM} P14 cells commingled and were generally distributed in clusters 1 and 2, while exhausted CD8⁺ T cells were mainly categorized into clusters 4–7 (Figures 3A, 3B, S2B, and S2C). The majority of tetramer-specific CD8⁺ T cells from the TdLNs of LUAD mice were distributed in clusters 1–3 (Figures 3A, 3B, S2B, and S2C). In agreement with this clustering, principal-component analysis (PCA) applied to the

pseudo-bulk RNA-seq data of each scRNA-seq sample further highlighted that TdLN-derived tumor-specific CD8⁺ T cells from both B16.Gp and LUAD bearing mice and conventional T_{MEM} cells were more closely neighbored but explicitly distal from exhausted CD8⁺ T cells from chronic LCMV-Cl13 infection or B16.Gp TME (Figure 3C).

We next investigated the differentially expressed genes across the 7 clusters to define subpopulation-specific transcriptional signatures. Cluster 1, termed as memory T cells 1 (T_{TMEM} 1), highly expressed genes characteristic of central memory T cells (T_{CM}) (*Il7r*, *Ccr7*, *Sell*, *Tcf7*, *Lef1*, and *Foxp1*) (Feng et al., 2011). Cluster 2, termed as memory T cells 2 (T_{TMEM} 2), also enriched similar memory signatures, while displayed higher level of *Cd69* (Figures 3A, 3D, 3E, and S2D). We also observed that clusters T_{TMEM} 1 and T_{TMEM} 2 accounted for about 50% of tumor-specific CD8⁺ T cells in TdLNs at 8 weeks after tumor induction, while declined to less than 20% at 17 weeks after LUAD induction (Figures 3A and 3B). Cluster 3 was defined as the T_{PEX} subset due to the co-expression of *Tcf7* and *Tox*, encompassing both TdLN- and TME-derived T_{PEX} cells (Figures 3A, 3D, 3E, S2C, and S2D). Clusters 4–6 expressed genes encoding inhibitory receptors (*Pdcd1*, *Entpd1*, and *Havcr2*) and the exhaustion-related TFs *Id2* and *Tox* (Figures 3A, 3D, 3E, and S2D). Consistent with this, antigen-specific CD8⁺ T cells from LCMV-Cl13 infection and TME were predominantly distributed into these clusters (Figures 3A, 3B, S2B, and S2C). Cluster 4 was distinguished from other subsets by *Cx3cr1* expression (Figure 3E), a marker for proliferating transitory exhausted CD8⁺ T cells (Hudson et al., 2019). Consistently, genes encoding effector molecules (*Klrg1*, *Klrc1*, *Gzmb*, *Gzma*, and *Ifng*) were also enriched in cluster 4 (Figures 3A, 3D, 3E, and S2D). Clusters 5 and 6 were further categorized as terminally (T_{EX}) and intermediate (Int-T_{EX}) exhausted subsets, respectively, according to the upregulated levels of *Pdcd1*, *Lag3*, *Entpd1*, *Cd160*, and *Tox* (Figures 3A, 3D, and 3E). Cluster 7 mainly expressed cell-cycle genes (*Cdc45*, *Mki67*, and *Clspn*) (Figures 3A, 3B, and S2B–S2D).

Furthermore, clusters 1 and 2 showed significant enrichment of gene ontology (GO) terms related to T cell proliferation involved in the immune response, likely reflecting a better proliferative potential of T_{MEM} cells and TdLN-derived tumor-specific CD8⁺ T cells (Figure S2E). Clusters 4–6 showed preferential enrichment in GO terms reflecting the functions of cytotoxicity and negative regulation of T cell activation, consistent with the individual gene expression data and sample distribution (Figures 3D, 3E, S2D, and S2E).

Next, we re-clustered TdLN-P14 cells and conventional T_{MEM} P14 cells (see details in STAR Methods) to explore the

Figure 2. TdLN-residing tumor-reactive TCF1⁺ CD8⁺ T cells are distinct from exhausted CD8⁺ T cells in TME

(A–D) Flow-cytometry analyses of the co-expression of TCF-1 (GFP) with effector molecules (A) or PD-1 (C) in CD44⁺P14 cells from indicated groups. Frequencies and MFIs are summarized in (B) and (D). n ≥ 4 (TME-P14, TdLN-P14); n = 3 (T_{EFF}-P14, T_{MEM}-P14, and T_{EX}-P14).

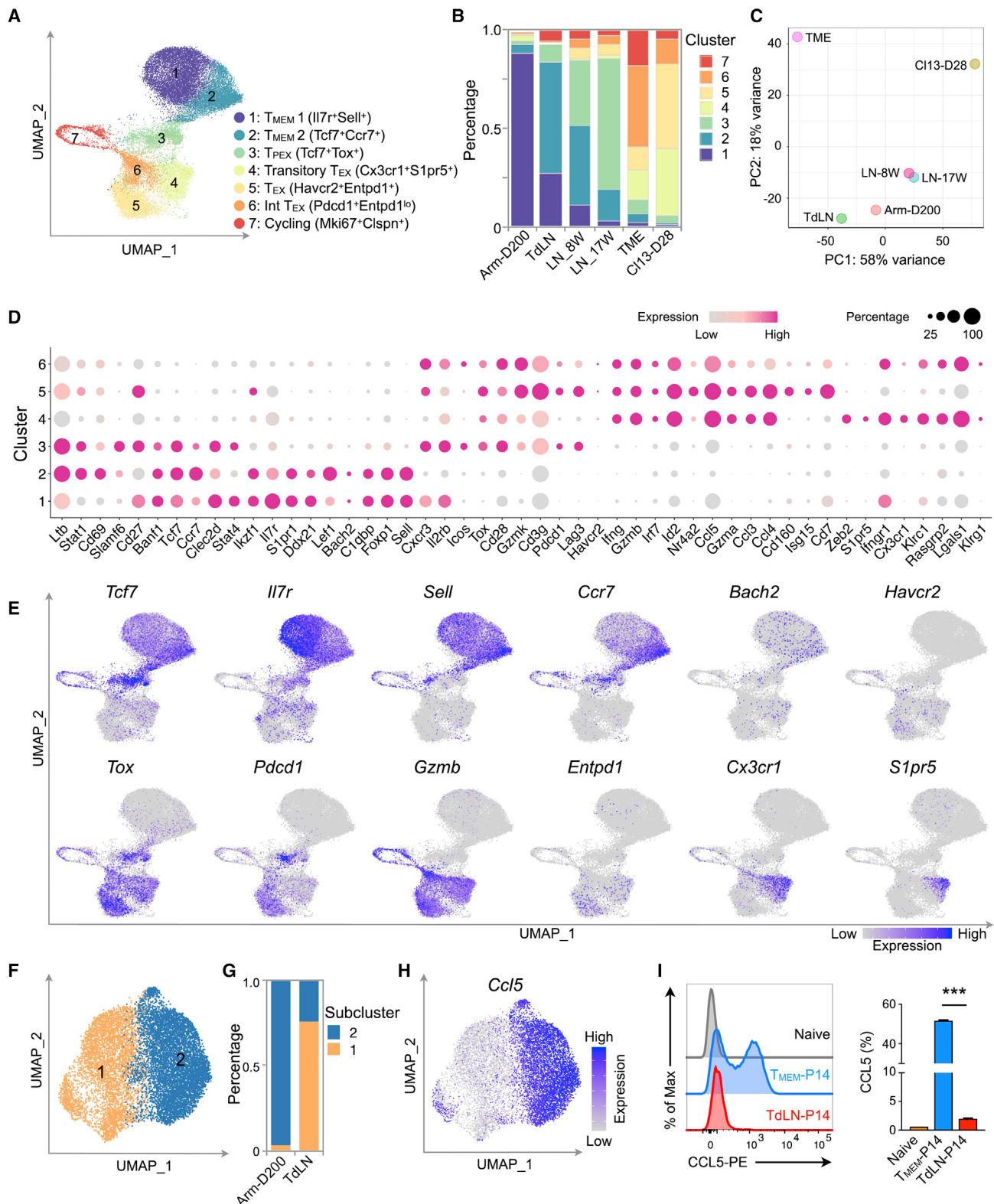
(E) *Pdcd1* mRNA expression analyzed by qPCR.

(F and G) Representative plots of the co-expression pattern of TCF-1 and exhaustion-related molecules in CD44⁺P14 cells from indicated groups (F). Frequencies and MFIs are summarized in (G). n ≥ 4 (TME-P14 and TdLN-P14); n = 3 (T_{EFF}-P14, T_{MEM}-P14, and T_{EX}-P14).

(H–J) Flow-cytometry analyses of CD62L, CD127, and CD122 in CD44⁺ P14 cells (H). Statistical analyses of the frequency and MFIs of memory-associated markers (I), and exhaustion-related markers (J) in TME-T_{PEX} (green, n ≥ 4), TdLN GFP⁺ (red, n ≥ 4), and Cl13 T_{PEX} P14 cells (yellow, n = 3).

*p < 0.05, **p < 0.01, and ***p < 0.001 versus control (one-way ANOVA). Data are representative of ≥2 independent experiments (mean ± SEM).

See also Figure S1.

**Figure 3. Transcriptional profiling of TdLN-derived tumor-specific CD8⁺ T cells by scRNA-seq**

(A) Uniform manifold approximation and projection (UMAP) visualization of the scRNA-seq clusters of antigen-specific CD8⁺ T cells (n = 22,376) from 6 samples.

(B) Bar plot demonstrating percentages of cells in clusters as a fraction of total cells for each sample, related to the UMAP plot in (A).

(legend continued on next page)

transcriptional differences that could distinguish these two populations. We obtained two robust subclusters, representing distinct distributions for TdLN-derived P14 cells (subcluster 1) and T_{MEM} P14 cells (subcluster 2), further confirmed by different clustering approaches and the distinct transcriptional signatures (Figures 3F, 3G, and S2F–S2I). Notably, subcluster 1 exhibited upregulation of activation-related transcripts such as *Junb*, *Cd69*, and *Stat1*. By contrast, memory-associated genes (*IIRb*, *IIR7*, *Bcl2*, and *Ccl5*) (Marçais et al., 2006) were more enriched in subcluster 2 (Figures S2H and S2I). Remarkably, *Ccl5* expression was specifically confined to subcluster 2 (Figures 3H, S2H, S2I, and S2K), further confirmed at the protein level (Figure 3I). Moreover, *Cd69/Junb* exhibited a mutually exclusive expression pattern with *Ccl5* (Figures S2L–S2O). Additionally, GO terms including T cell extravasation and chemotaxis were less enriched in subcluster 1 (Figure S2J), indicating the potentially distinct circulating features between these two subsets.

Next, we compared the chromatin accessibility regions (ChARs) of TdLN-P14 cells (days 4, 8, and 21 post adoptive cell transfer) with other CD8⁺ T cell subsets. PCA analysis identified that TdLN-derived P14 cells from three time points were highly identical to each other in terms of the epigenetic profile but differed from the remaining subsets (Figure S3A). We identified 6,316 loci with differential ChARs between TdLN-derived P14 cells and the other subsets. Hierarchical clustering of those loci showed that the TdLN-derived P14 subsets from different time points established identical epigenetic landscapes as early as Day 4 and maintained afterward, which clearly distinguished TdLN-derived P14 subset from T_{MEM} , T_{MP} , T_{EFF} , T_{PEX} , and T_{EX} subsets (Figure S3B). Cluster 1 included a large number (36% of 6,316 loci) of open ChARs almost unique to the TdLN-P14 subsets, which were significantly mapped to proximal genes related to the functions of T cell activation, cytokine production, and lymphocyte differentiation (Figures S3B and S3C). Moreover, the TdLN-P14 cells shared certain open chromatin loci with the T_{PEX} subset in cluster 2 (613 of 6,316 loci) and the T_{MEM} subset in cluster 6 (660 of 6,316 loci) (Figure S3B) but were excluded from sharing open chromatin loci with T_{EX} (cluster 4) and T_{EFF} (cluster 5) subsets (Figure S3B). At peaks more open in TdLN-P14 cells, we found motifs for members of the ETS, Runx, and HMG Box TF families to be the most significantly enriched. The top hits encompassed RUNX1, RUNX2, ETS1, ELKs, and TCF7L2 (Figure S3D), most of which are associated with T_{MEM} differentiation (Chang et al., 2014; Kaech and Cui, 2012).

- (C) Principal-component analysis (PCA) plot of aggregated signal in scRNA-seq. Single-cell level measurements for each sample were aggregated to obtain pseudo-bulk counts for the PCA analysis, related to the UMAP plot in (A).
- (D) Dot plot representing the relative average expression of a subset of marker genes across all clusters except cluster 7 (cell-cycling cluster). The marker genes in each cluster were identified by log fold change compared with the remaining clusters (see details in STAR Methods).
- (E) Single-cell transcription levels of representative genes illustrated in the UMAP plot from (A). Transcription levels are color coded: gray, not expressed; blue, expressed.
- (F) TdLN- and Arm-day 200 cells selected from clusters 1 (T_{MEM} 1) and cluster 2 (T_{MEM} 2) in the UMAP plot (A) were sub-clustered in the UMAP plot.
- (G) Bar plot showing percentages of cells in clusters as a fraction of total cells for each sample, related to the UMAP plot in (F).
- (H) Single-cell transcription level of *Ccl5* illustrated in the UMAP plot in (F). For TME and TdLN, cells are pooled from 20 mice. For Arm⁺ T_{MEM} , cells are pooled from 8 mice.
- (I) Flow-cytometry analysis of the expression of CCL5 in naive, T_{MEM} (day 60) and TdLN (day 15 post tumor inoculation) derived P14 cells. $n \geq 3$ /group. Frequencies of CCL5 positive P14 cells were summarized beside.
- *** $p < 0.001$. One-way ANOVA analysis (I). Data are representative of ≥ 2 independent experiments (mean \pm SEM).
- See also Figures S2 and S3.

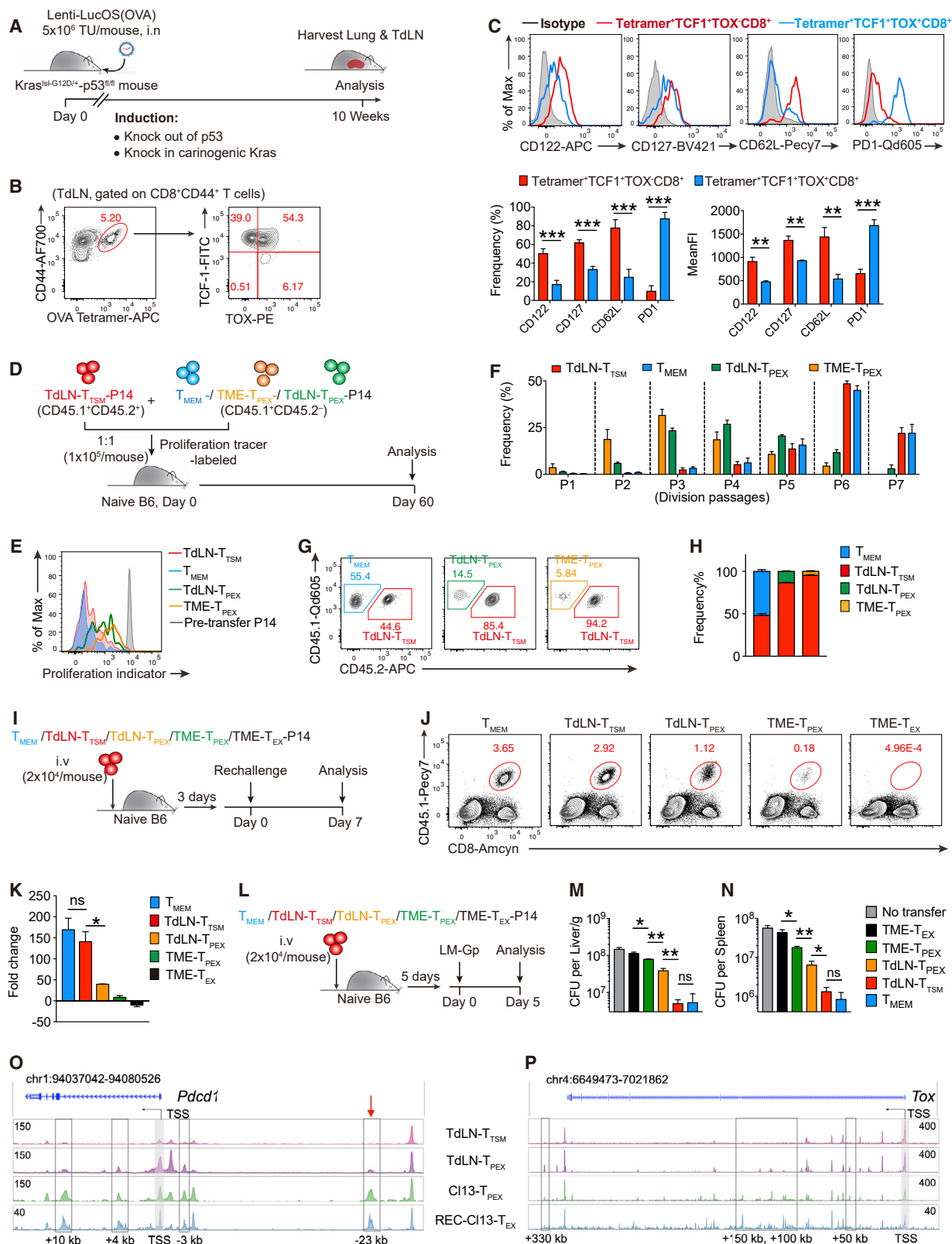
Additionally, open chromatin peaks were found at the transcription start sites (TSSs) and/or its proximal loci of genes related to memory properties (*Tcf7* and *IIR7*) in TdLN-P14 cells, T_{MEM} P14 cells, and T_{MP} P14 cells but not in T_{EX} or T_{EFF} subsets (Figures S3G and S3H). Genes encoding inhibitory receptors (*Pdcld1* and *Havcr2*) were less open in those subsets with memory properties, while became more accessible during the transition from T_{EFF} to T_{EX} subsets (Figures S3I and S3J). Notably, the TdLN-derived P14 subset had greater chromatin accessibility at the TSS of *Cd69* than did other subsets but less chromatin accessibility at the TSS of *Ccl5* (Figures S3E and S3F), further corroborating both genes as core transcriptional signatures for distinguishing TdLN-P14 cells from conventional T_{MEM} cells.

TCF1⁺TOX[−] tumor-specific CD8⁺ T cells in TdLNs are bona fide memory cells, distinct from TCF1⁺TOX⁺ counterparts

TCF1⁺ T_{PEX} cells were also recently identified in TdLNs of LUAD mice (Connolly et al., 2021; Schenkel et al., 2021). As an exhaustion-specific TF, TOX is predominantly expressed by both TCF-1⁺ T_{PEX} cells and TCF-1[−] T_{EX} cells, but not by memory subsets (Alfei et al., 2019; Khan et al., 2019; Scott et al., 2019; Seo et al., 2019; Yao et al., 2019). Consistently, we have observed that around 20% of TdLN-derived TCF⁺P14 cells expressed exhaustion-specific marker TOX in B16.Gp bearing mice (Figures 2F and S1H). The presence of both TCF1⁺TOX[−] and TCF1⁺TOX⁺ subsets was further recapitulated in endogenous TdLN-derived tumor-specific CD8⁺T cells (Figures S1I and S1J).

To further compare endogenous tumor-specific TCF1⁺TOX[−]CD8⁺ T cells and TCF1⁺TOX⁺ counterparts in TdLNs of non-subcutaneous tumor models, we set up mouse model of K/P LUAD expressing ovalbumin (OVA) (Connolly et al., 2021; Schenkel et al., 2021) (Figure 4A). We observed the presence of both OVA_{257–264} H-2K^b tetramer⁺ TCF1⁺TOX[−] and TCF1⁺TOX⁺ CD8⁺ T cell subsets in TdLNs (Figure 4B), and the former exhibited memory phenotypes, evidenced by higher levels of memory-associated markers CD122, CD127, and CD62L but relatively lower expression of PD-1 than TCF1⁺TOX⁺TdLN- T_{PEX} cells (Figure 4C).

Based on their phenotypic characteristics of canonical T_{MEM} cells, we reasoned that tumor-specific TCF1⁺TOX[−]CD8⁺ T cells in TdLN likely represented a distinct memory T cell subset, which was termed as TdLN-residing tumor-specific



(legend on next page)

memory T (TdLN-T_{TSM}) cells thereafter. Accordingly, tumor-specific TCF-1⁺TOX⁺CD8⁺ T cells in TdLN_s were named as TdLN-T_{PEX} cells based on TCF-1 and TOX co-expression. To further validate TdLN-T_{TSM} cells, but not TdLN-T_{PEX} cells, as a bona fide memory T cell subset, we compared both subsets in terms of canonical memory properties. First, we observed that PD-1 expression was positively correlated with TOX expression in TdLN-derived P14 cells, which can be used as a surrogate for TOX expression when sorting TdLN-P14 cells (Figures S4A and S4B). Subsequently, we co-transferred TdLN-T_{TSM} P14 cells with TdLN-T_{PEX} or TME-T_{PEX} P14 cells or with conventional T_{MEM} P14 cells into naive B6 recipients at 1:1 ratio (Figure 4D). On day 60 post transfer, we found that both TdLN-T_{TSM} and T_{MEM}-P14 cells underwent more pronounced homeostatic proliferation than did TdLN- and TME-T_{PEX} counterparts (Figures 4E and 4F). Consequently, the ratio between TdLN-T_{TSM} and T_{MEM} cells was maintained approximately at 1:1 ratio, while the ratio of TdLN- or TME-T_{PEX} to TdLN-T_{TSM} was profoundly decreased on D60 post transfer (Figures 4G and 4H). Moreover, to evaluate the proliferative potential of TdLN-T_{TSM} cells upon rechallenge, TdLN-T_{TSM}, TdLN-T_{PEX}, and T_{MEM} P14 cells were sorted and transferred separately into naive recipients with the same number, which were then rechallenged with LCMV-Arm⁺ (Figure 4I). At 7 days post rechallenge, we visualized 150- to 180-fold increase in the number of TdLN-T_{TSM} cells and T_{MEM} P14 cells, while only about 40-fold increase was observed in TdLN-derived T_{PEX} cells (Figures 4J and 4K). Consistently, we found that TdLN-T_{TSM} P14 cells conferred much stronger protection against Lm-Gp_{33–41} rechallenge than both TdLN-T_{PEX} P14 cells and TME-T_{PEX} P14 cells, while equivalent to that mediated by conventional T_{MEM} counterparts (Figures 4L–4N). Taken together, these results demonstrated that TdLN-T_{TSM} cells, but not TdLN-T_{PEX} cells, possessed canonical memory features.

Next, we performed ATAC-seq to examine whether TdLN-T_{TSM} cells obtained a distinct epigenetic profile from TdLN-T_{PEX} cells. PCA identified that TdLN-T_{TSM} P14 cells substantially differed from TdLN-T_{PEX} and CI13-T_{PEX} counterparts (Jadhav et al., 2019) in open ChARs (Figure S4C). Furthermore, hierarchical clustering revealed that although TdLN-T_{TSM} and TdLN-T_{PEX}

P14 cells largely shared open chromosome accessibility pattern in cluster 2 (3,736 loci) (Figure S4D) that contained memory-associated signatures (*Tcf7*, *Bach2*, *Foxp1*, *Ccr7*, *Sell*, *Id3*, and *Lef1*), they were distinguished by cluster 4 (5,257 loci) that comprised exhaustion molecules, including *Pdcid1*, *Tox*, *Id2*, *Havcr2*, *Ctla4*, and *Lag3* (Figure S4D). Consistently, GO analysis revealed that cluster 2 was mapped to gene loci associated with survival and positive regulation of activation, differentiation, and cytokine, whereas cluster 4 was enriched in gene loci related to programmed cell death and negative regulation of cytokine production and immune process (Figure S4E). Furthermore, we found binding motifs for several members of the ETS, Runx, and HMG Box TF families to be the most significantly enriched in cluster 2 (Figure S4F), most of which are associated with memory CD8⁺ T cell differentiation (Chang et al., 2014; Kaech and Cui, 2012). By contrast, cluster 4 significantly enriched AP-1 complex-related and EGR family motifs (Figure S4F), in keeping with the regulatory role of AP-1 family TFs in T cell exhaustion (Martinez et al., 2015). Consistently, chromatin accessibility profiles of individual genes associated with T cell memory (*Tcf7*, *Ccr7*, *Sell*, *Id3*, and *Lef1*) were largely comparable among these three subsets, while those with exhaustion-related gene signatures (*Pdcid1*, *Havcr2*, and *Tox*) clearly distinguished the TdLN-T_{TSM} subset from TdLN-T_{PEX} and CI-13 T_{PEX} subsets (Figures 4O, 4P, and S4I–S4N).

Recently, several studies demonstrated that virus-specific T_{PEX} cells were irreversibly associated with epigenetic scarring on the loci of important exhaustion regulators, including *Tox* and *Pdcid1* (Abdel-Hakeem et al., 2021; Tonnerre et al., 2021; Yates et al., 2021). In tumor scenario, we observed that TdLN-T_{TSM} cells were not marked by epigenetic scars at *Tox* and *Pdcid1* loci, while TdLN-T_{PEX} cells, together with CI13-T_{PEX} cells and recovered T_{EX} cells (REC-T_{EX}, recovered from antigen removal) (Abdel-Hakeem et al., 2021) exhibited epigenetic scars at both *Tox* and *Pdcid1* loci (Figures 4O and 4P). Consequently, TdLN-T_{PEX} cells could not differentiate into authentic effector cells after antigen removal and ensuing antigen rechallenge, shown by profoundly compromised KLRL1 expression and the differentiation into IFN- γ ⁺/TNF- α ⁺ effector cells as compared with both TdLN-T_{TSM} cells

Figure 4. TdLN-T_{TSM} are distinct from TdLN-T_{PEX} cells

(A–C) Kras^{LSL-G12D/+}-p53^{f/f} lung adenocarcinoma model (K/P model). (A) Experimental design. (B) Representative plots of H-2K^b OVA_{257–264}-specific CD8⁺CD44⁺ T cells in TdLN_s (left) and the co-expression pattern of TCF-1 and TOX in tetramer⁺ CD8⁺CD44⁺ T cells (right). (C) Histogram showing the expression levels of CD122, CD127, CD62L, and PD-1 in OVA-specific TCF1⁺TOX[−] (red), TCF1⁺TOX⁺ CD8⁺ T cells in TdLN (blue) and isotype control (gray) from the K/P model. The frequencies and MFIs of indicated makers in each population are summarized below. n = 5 mice/group.

(D–H) Homeostatic proliferation and long-term persistence of TdLN-T_{TSM}, TdLN-T_{PEX}, TME-T_{PEX}, or T_{MEM} P14 cells. (D) Experiment design. (E) Histogram demonstrating the dilution patterns of the cell proliferation indicating dye on gated CD44⁺ P14 cells originated from indicated donors. Proliferation indicating dye labeled P14 cells before transfer were incorporated as control (gray). (F) Summary of the frequencies of P14 cells at each division passage. (G) Flow-cytometry analyses of the percentages of TdLN-T_{TSM} (CD45.1⁺CD45.2⁺, red line) versus T_{MEM} (CD45.1⁺CD45.2[−], blue line), TdLN-T_{PEX} (CD45.1⁺CD45.2[−], green line) or TME-T_{PEX} cells (CD45.1⁺CD45.2[−], yellow line) in the spleens of the host mouse, at day 60 post cell transfer. Proportions of each population are summarized at (H), n = 4 for each group.

(I–K) Rechallenge assay. (I) Experiment design. (J) Representative flow-cytometry plots of CD45.1⁺ P14 cells in the spleens of recipient mice transferred with indicated populations at day 7 p.i. (K) Summary of numerical fold changes of each group relatively to its initial cell number of each group. n = 6 (T_{MEM}); n = 4 (TdLN-T_{TSM}); n = 3 (TdLN-T_{PEX}); n = 4 (TME-T_{PEX}); and n = 5 (TME-T_{EX}).

(L–N) Listeria protection assay. (L) Experiment design. Bacteria loads of Lm-Gp in the liver/g (n = 3/group, M) and spleen (n = 3/group, N) of Cd8^{−/−} mice transferred with different donor cells (2 × 10⁴/mice), 5 days post infection. *p < 0.05, **p < 0.01, and ***p < 0.001 versus control, ns stands for not significant, two-tailed Student's t test (C and H) or one-way ANOVA (F, K, M, and N). Data are representative of ≥2 independent experiments (mean ± SEM).

(O and P) The ATAC-seq track views for *Pdcid1* (O) and *Tox* (P) in indicated subset. Gray boxes, TSS positions; highlighted rectangles, open peaks indicating epigenetic scars at promoter-proximal regions. Red arrow indicating the well-defined exhaustion-related enhancer for *Pdcid1* gene (Abdel-Hakeem et al., 2021). See also Figure S4.

and conventional T_{MEM} cells, while still maintaining high PD-1 and TOX expression (Figures S4G and S4H).

Collectively, these data strengthened the notion that TdLN-T_{TSM} cells were bona fide memory T cells, while TdLN-T_{PEX} cells were epigenetically defined as an exhaustion subset due to epigenetic scarring.

TdLN-derived tumor-reactive memory CD8⁺ T cells in HCC patients

Next, we sought to explore the existence of TdLN-T_{TSM} cells in human hepatocellular carcinoma (HCC). Toward this end, we first sorted activated CD8⁺ T cells potentially comprising tumor-reactive memory CD8⁺ T cells from TdLNs by using CD45RA⁻CD8⁺CCR7⁺PD-1^{dim} gating strategy and putative tumor-reactive exhausted CD8⁺ T cells from paired TME by using CD45RA⁻CD8⁺PD-1⁺CD39⁺ gating strategy to exclude bystander CD8⁺ T cells (Simoni et al., 2018) and then performed scRNA-seq and sc-TCR sequencing to investigate the transcriptional profiles of the TCR clones shared between paired samples. We noticed that those sorted cells displayed enormous heterogeneity and were categorized into 9 distinct subsets (Figures S5A, S5B, and S5D), and both T_{MEM} and T_{PEX} subsets were shown in the sorted TdLN-derived CD8⁺ T cells (Figures S5B–S5E). Then we used the TCR α - and β -chain sequences (Table S2) as clonal markers to trace shared CD8⁺ T cell clones between paired TdLNs and TME. Only those clones with identical TCR α - and β -chain sequences shared by TdLN- and TME-derived CD8⁺ T cells from the same patient and expanded at least twice in TME samples were regarded as reactive to tumor antigens (Figures S5F and S5G). We obtained 207 TCR clonotypes concomitantly shown up in paired TdLNs and TME, representing 1,165 and 2,203 CD8⁺ T cells from TdLNs and TME, respectively (Figures S5G and S5H). These shared TCR clones were clearly categorized into three clusters (Figure 5A). Based on TCF7 and TOX expression, cluster 1 was assigned as T_{TSM} like (TCF7⁺TOX⁻), while clusters 2 and 3 as T_{PEX} (TCF7⁺TOX⁺) and T_{EX} (TCF7⁻TOX⁺), respectively (Figure 5A). The TCR clones derived from TdLNs were primarily grouped into cluster 1 (Figures 5A–5C), while the corresponding TCR clones from TME were preferably allocated into cluster 2 and 3 (Figures 5A–5C and S5I). Notably, we observed about 30% of TCR clones in TdLNs were identified as T_{PEX} cells by TCF7 and TOX co-expression (cluster 2) (Figures 5A–5C and S5I), consistent with the results in mouse tumor models.

Furthermore, pseudotime trajectory analysis revealed that these shared TCR clones possessed a continuous differentiation trajectory that started from the clones predominantly derived of TdLNs toward the end of the clones from TME (Figure 5D). The TCR clones on early pseudotime exhibited a distinguishable memory-like phenotype, while the TCR clones on later pseudotime displayed a distinct exhaustion state (Figure 5E). TCF7 and CCR7 underwent gradual decreases in expression levels along the pseudotime trajectory (Figure 5F). Conversely, representative exhaustion markers (TOX and LAG3) and markers associated with T cell activation (JUNB, CD69, and STAT1) progressively increased along the pseudotime trajectory (Figure 5F).

To potentially prove the antigenic specificity of those TdLN-derived T_{TSM}-like cells in HCC, we cloned TCR sequences

from top 6 expanded clones in cluster 1 (representing memory properties) (Figure 5A; Table S3), each of which was shared by CD8⁺ T cells in paired TME and TdLNs. We ectopically expressed the selected TCR sequences in the autologous blood-derived CD8⁺ T cells with lenti-virus transduction system. Then, the transduced CD8⁺ T cells were sorted and co-cultured with autologous tumor cells for 18–20 h (Figure 5G). We observed that over 80% of transfected CD8⁺ T cells expressed selected TCRs (Figure S5J), and 5 out of the 6 selected TCR clonotypes were proved to be specifically recognizing their autologous tumor cells, evidenced by IFN- γ production and increased expression of 4-1BB of these TCR-transduced cells when co-cultured with autologous tumor cells (Figures 5H–5I and S5K). Taken together, these multiple lines of evidence demonstrated the existence of TdLN-T_{TSM} cells in human cancer.

TdLN-T_{TSM} cells differentiate into TdLN-T_{PEX} cells

Next, we examined the differentiation relationship between TdLN-T_{TSM} cells and TdLN-T_{PEX} cells during tumor progression. To this end, TdLN-T_{TSM} P14 cells and TdLN-T_{PEX} P14 cells were separately transferred into tumor-matched B6 mice (Figure S6A). At D8 post cell transfer, we found that a fraction of transferred TdLN-T_{TSM} P14 cells differentiated into TdLN-T_{PEX} ones, but not vice versa, suggesting TdLN-T_{TSM} cells as precursors of TdLN-T_{PEX} cells (Figure S6B). Furthermore, more TdLN-T_{TSM} derived progeny cells were recovered within blood and TME of recipient mice than TdLN-T_{PEX} derived ones (Figure S6C). In blood, TdLN-T_{TSM} derived P14 cells maintained higher expression of memory markers, including TCF1, CD62L, CD127, and CD122, than the counterparts derived from TdLN-T_{PEX} subset; however, in the TME, most of the progeny P14 cells from donor-derived both TdLN-T_{TSM} and TdLN-T_{PEX} P14 cells finally differentiated into TCF1⁻TOX⁺T_{EX} cells (Figures S6D and S6E). Given TdLN-T_{TSM} cells as precursors of TdLN-T_{PEX} cells, these results together suggested a linear differentiation mode between TdLN-T_{TSM}, TdLN-T_{PEX}, TME-T_{PEX}, and T_{EX} subsets during tumorigenesis.

TdLN-T_{TSM} cells exhibit superior control of tumor growth when adoptively transferred

Next, we assessed anti-tumor therapeutic effects of TdLN-derived T_{TSM} cells when adoptively transferred. Toward this end, sorted TdLN-derived T_{TSM} OT1 cells, T_{PEX} OT1 cells (specifically recognizing H-2K^b OVA_{257–264}), and TME-derived T_{EX} OT1 cells were adoptively transferred into B16.OVA bearing Cd8^{-/-} mice, and tumor volume was monitored (Figure 6A). TdLN-T_{TSM} cells exhibited the most pronouncing capacity in tumor repression among these three populations, and TdLN-T_{PEX} OT1 cells showed relatively better anti-tumor efficacy than T_{EX} cells (Figures 6B and 6C), coincident with previous studies (Krishna et al., 2020; Kurtulus et al., 2018; Sade-Feldman et al., 2018; Siddiqui et al., 2019). Moreover, tumor-bearing mice receiving TdLN-T_{TSM} OT1 cells demonstrated a complete remission whereas their counterparts in other two groups were not able to survive at the endpoint of day 40 post tumor cell engraftment (Figure 6D). These results therefore highlighted that compared with TdLN-T_{PEX} or TME-T_{EX} cells, TdLN-T_{TSM} cells were superior in controlling tumor growth when adoptively

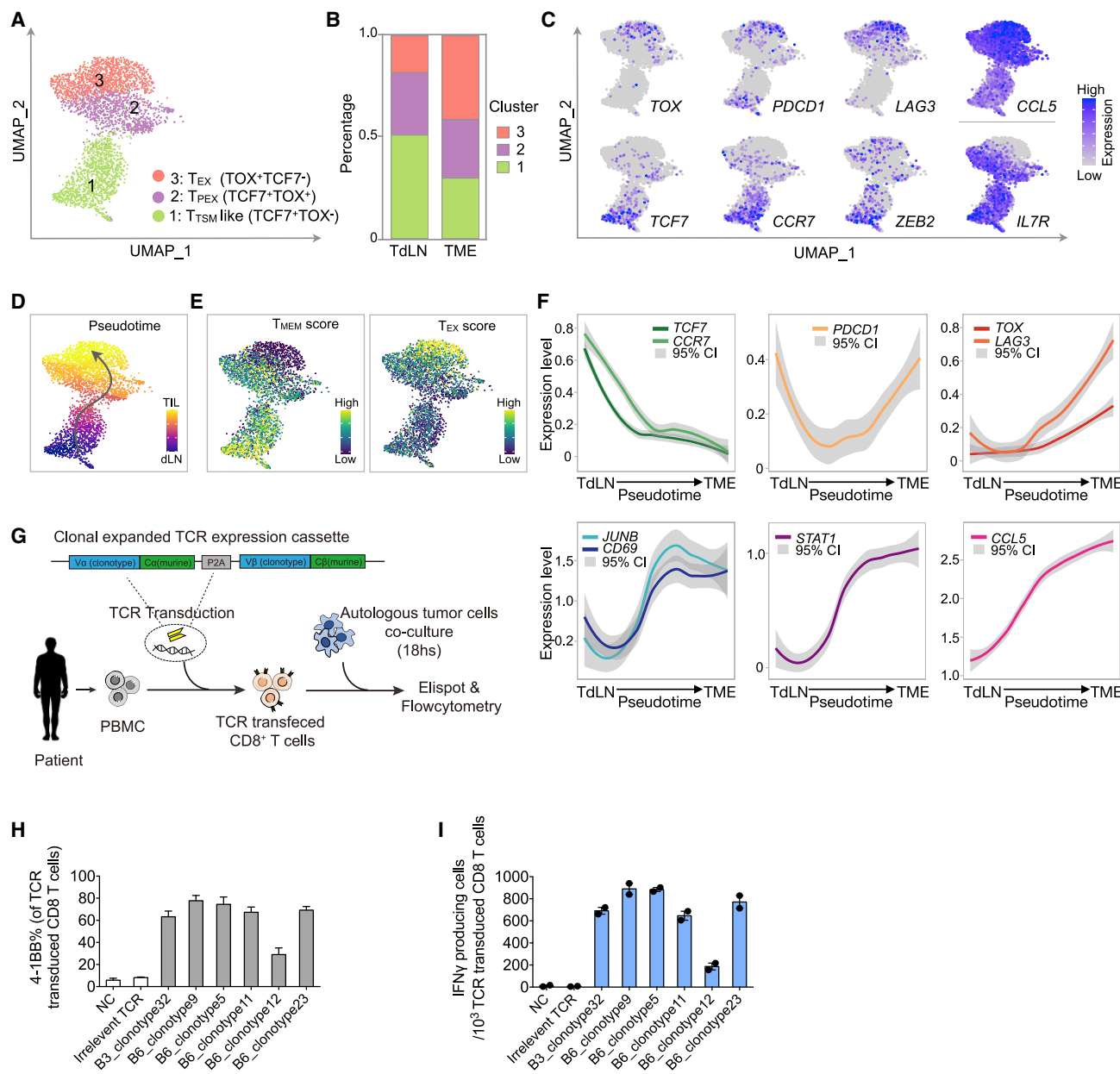


Figure 5. Identification and characterization of TdLN-derived tumor-reactive memory CD8⁺ T cells in HCC patients

(A) UMAP analysis of the scRNA-seq data of tumor-reactive CD8⁺ T cells with shared TCR clones ($n = 3,368$) from 6 HCC patients. Each dot represents an individual cell with a shared TCR clone. The shared clonotypes were listed in Table S2.

(B) Bar plot demonstrating percentages of TCR clones in clusters as a fraction of total clones for TdLN or TME, related to the UMAP plot in (A).

(C) Single-cell transcription levels of representative genes illustrated in the UMAP plot from (A). Transcription levels are color coded: gray, not expressed; blue, expressed.

(D) UMAP plot showing differentiation trajectory inferred by Monocle3 (STAR Methods). Arrow, differentiation trajectory.

(E) The memory property score (T_{MEM} score, left panel) and exhaustion score (T_{EX} score, right panel) illustrated in the UMAP plot from (A). See details in STAR Methods.

(F) Smoothed expression profiles of representative markers along pseudotime differentiation defined in (D). Error bars (gray) denote 95% confidence intervals (CI).

(G–I) Evaluating the tumor antigen specificity of TdLN-derived T_{TSM}-like cells in HCC patients. (G) Experiment design. The CDR3 sequence of each selected TCR clonotype were listed in Table S2. The nucleotide sequences of the six selected chimeric TCRs were listed in Table S3. (H) Statistic summary of 4-1BB expression in CD8⁺ T cells transduced with indicated TCR clonotype. (I) Summary of IFN- γ producing cells per 10³ CD8⁺ T cells transduced with indicated TCR clonotype. Error bars denote SEM.

See also Figure S5 and Tables S1–S3.

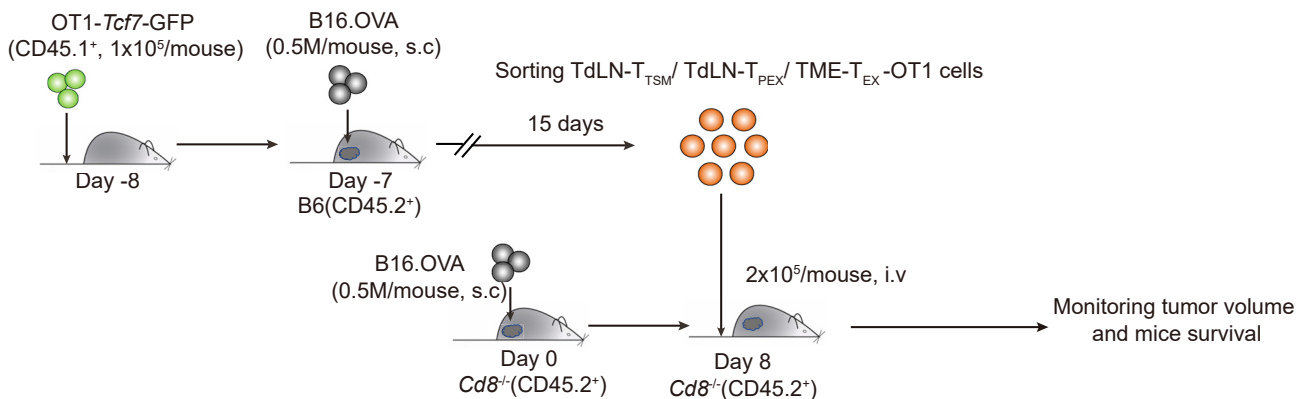
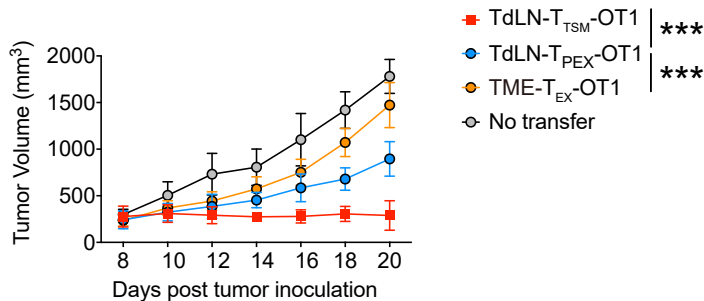
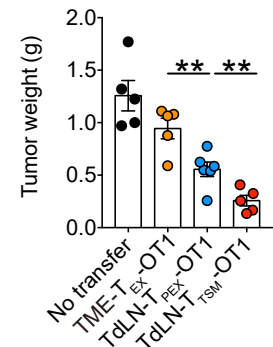
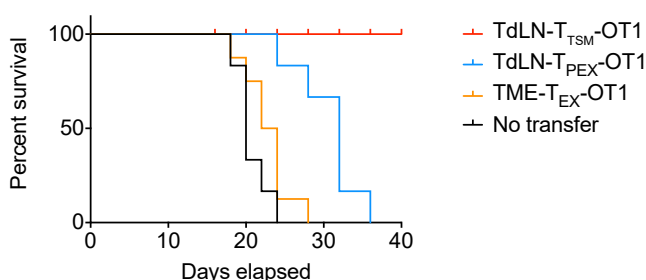
A**B****C****D**

Figure 6. TdLN-derived T_{TSM} cells exhibit superior control of tumor growth

(A) Experiment design.

(B) Tumor volume curves for mice receiving TdLN-T_{TSM}-OT1 cells (n = 5), TdLN-T_{PEX} (n = 6), and TME-T_{EX} OT1 cells transfer (n = 5) or without transfer (n = 5).

(C) Tumor weight of mice adoptively transferred with different OT1 cells as in (B) on day 12 post cell transfer.

(D) Survival curve for tumor-bearing mice from indicated groups describe in (A) (n ≥ 6/group).

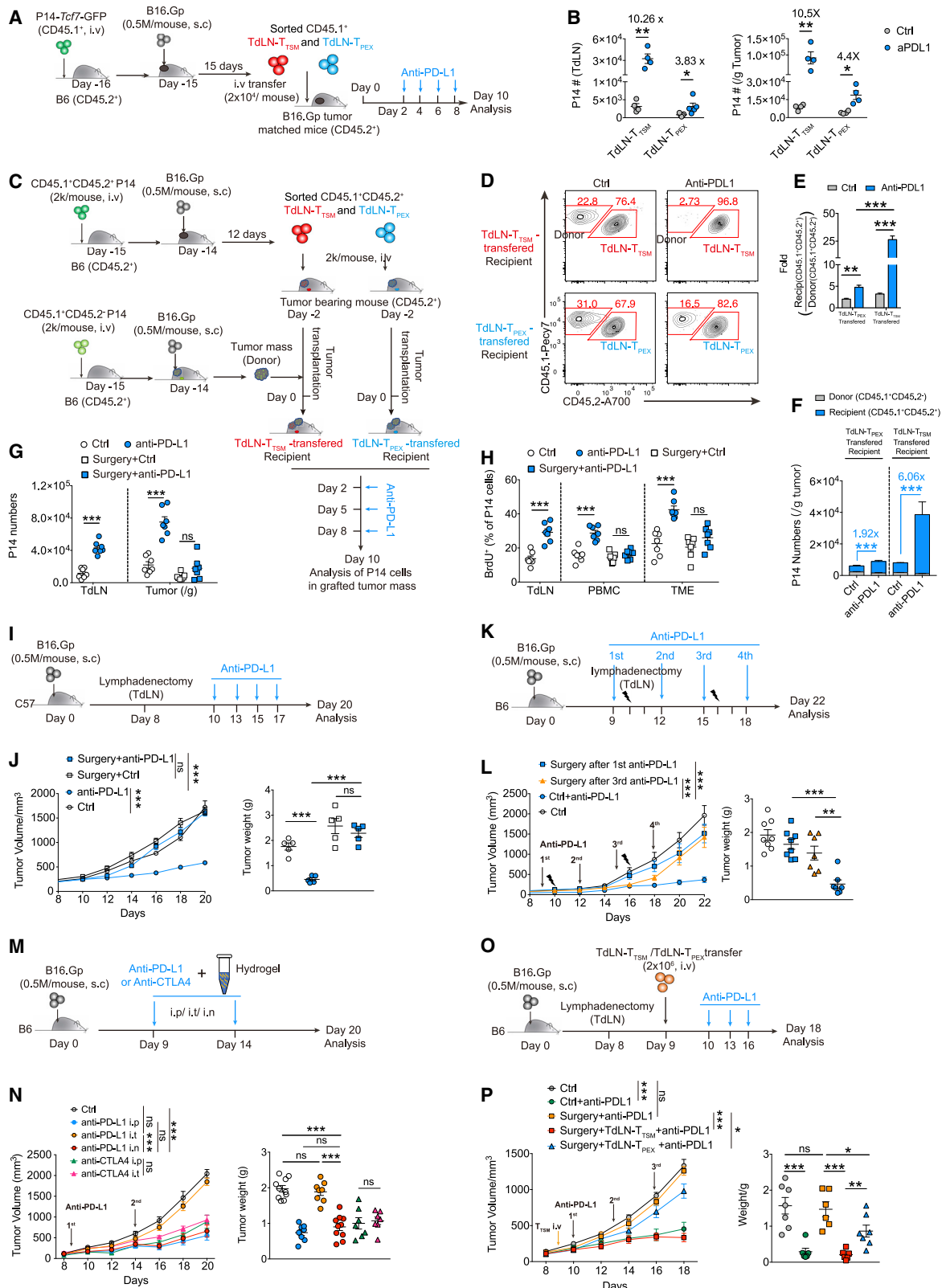
p < 0.01, *p < 0.001 versus control, one-way ANOVA (C), two-way ANOVA (B), or log-rank (Mantel-Cox) test (D). Data are representative of ≥2 independent experiments (mean ± SEM).

transferred and could be exploited as a promising strategy of adoptive T cell immunotherapy.

TdLN-T_{TSM} cells are bona fide responders to PD-1/PD-L1 blockade

Finally, we sought to define whether TdLN-T_{TSM} cells could respond to PD-1/PD-L1 ICB. To this end, an equal number of

sorted TdLN-T_{TSM} P14 cells and TdLN-T_{PEX} P14 cells were re-transferred to B16.Gp tumor-matched mice, respectively, followed by anti-PD-L1 treatment at indicated time points (Figure 7A). At day 10 post cell transfer, we observed more prominent expansion of TdLN-T_{TSM} derived-P14 cells than TdLN-T_{PEX} derived ones upon the administration of anti-PD-L1 mAb, in both TdLNs and TME of recipient mice (Figure 7B). Similarly,



(legend on next page)

TdLN-T_{TSM} derived P14 cells exhibited more significant augmentation in quantity and cytokine production than TdLN-T_{PEX} derived P14 cells upon treatment with anti-PD1 antibodies *in vitro* (Figures S7A–S7C), suggesting that TdLN-T_{TSM} cells, rather than TdLN-T_{PEX} P14 cells primarily responded to PD-1/PD-L1 ICB.

To further validate TdLN-T_{TSM} cells as the principal responders to PD-L1 ICB, tumor mass from day 14 B16.Gp tumor-bearing mice (initially CD45.1⁺CD45.2⁻ P14 cells transferred, donor) were surgically dissected and transplanted into TdLN-T_{TSM} or TdLN-T_{PEX} P14 cells (CD45.1⁺CD45.2⁺) adoptively transferred tumor-bearing mice (recipient) (Figure 7C). As expected, we observed much greater ratio of TdLN-T_{TSM}-derived P14 cells to donor-derived P14 cells than that of TdLN-T_{PEX} derived P14 cells to donor-derived P14 cells in grafted tumor mass post PD-L1 ICB; consistently, anti-PD-L1 treatment led to more efficiently expanded TdLN-T_{TSM}-cell-derived P14 cells than TdLN-T_{PEX} derived counterparts in transplanted tumor mass (Figures 7D–7F). These data together established TdLN-T_{TSM} cells as the principal responders to PD-L1 ICB.

Furthermore, we observed that PD-L1 ICB could not lead to enhanced number and BrdU incorporation of P14 cells in the TME when the dLNs were surgically removed (Figures S7D, S7G, and S7H). Provided TdLN-T_{TSM} cells as the principal responders of PD-L1 ICB, these results indicated that PD-L1 ICB may exert its effect at least partially via expanding T_{TSM} P14 cells in TdLNs. To further confirm this notion, B16.OVA bearing mice were first treated with one dose of anti-PD-L1 blocking antibody on day 3 after OT1 cell transfer, then these mice received intraperitoneal (i.p.) administration of BrdU. 3 h later, half of the mice received lymphadenectomy of TdLNs while others received sham-operation, and the kinetics of BrdU⁺ OT1 cells in TME were analyzed afterward at indicated time points (Figure S7E). Notably, we observed a continuous accumulation of BrdU-positive OT1 cells in the TME of mice received sham-operation upon anti-PD-L1 administration, while the proportion of BrdU⁺ OT1 cells in mice of TdLN removal remained unchanged (Figure S7F),

further supporting that PD-L1 ICB treatment expanded tumor-specific CD8⁺ T cells in TdLNs, rather than in TME. In line with these data, the tumor repressive capacity of anti-PD-L1 mAbs was almost abolished when TdLNs were surgically removed (Figures 7I and 7J). Remarkably, removal of TdLNs at any individual time point during anti-PD-L1 therapy almost abrogated the tumor-suppressive effects of anti-PD-L1 treatment in B16.Gp bearing mice (Figures 7K and 7L), which was further reproduced with MC38 tumor-bearing mice (Figures S7G and S7H). These results demonstrated that TdLN-residing tumor-specific CD8⁺ T cells were constantly required for the anti-tumor effectiveness of PD-L1 ICB.

To validate the importance of TdLN-residing tumor-specific CD8⁺ T cells in PD-L1 ICB, we treated B16.Gp tumor-bearing mice with ICBs through different routes, including i.p., intratumoral (i.t.), and intranodal (tumor-draining LN, i.n.) injection, by mixing blocking antibodies with Pluronic F127 hydrogel, which was proved to effectively limit encapsulated antibodies to exert therapeutic effects locally (Almoshari et al., 2020) (Figure 7M). We noticed that i.p. administration of anti-PD-L1 effectively restrained tumor growth, while the i.t. administration of anti-PD-L1 inefficiently restrained tumor growth; however, i.n. administration of anti-PD-L1 demonstrated comparable capacity in repressing tumor growth as i.p. administration. As a control, we found that i.t. administration of anti-CTLA4 effectively restrained tumor growth as i.p., consistent with published data (Melero et al., 2021) (Figure 7N). These data corroborated the notion that tumor-specific CD8⁺ T cells residing in TdLN were the predominant targets of PD-L1 ICB in exerting its therapeutic effects.

To further define the pivotal role of TdLN-T_{TSM} cells in responding to PD-L1 ICB, we transferred bulk TdLN-T_{TSM} cells into tumor-matched recipients that had undergone surgical excision of TdLNs. Following adoptive cell transfer, we treated these mice with anti-PD-L1 antibodies (Figure 7O). Consistently, lymphadenectomy abrogated the tumor-suppressive effects of PD-L1 ICB, while the adoptive transfer of TdLN-T_{TSM} cells, but not TdLN-T_{PEX} cells, efficiently rectified PD-L1 ICB mediated

Figure 7. TdLN-residing-T_{TSM} cells are genuine responders to PD-L1 ICB

(A and B) Examining the different responses of TdLN-T_{TSM}- and TdLN-T_{PEX}-P14 cells upon anti-PD-L1 treatment. (A) Experiment design. (B) Numeric analyses of transferred TdLN-T_{TSM}- and TdLN-T_{PEX}-P14 cells in the TdLNs ($n \geq 4$) and tumor (per gram, $n = 4$) of recipient mice from each group.

(C–F) Tumor transplantation assay. (C) Experiment design. (D) Flow-cytometry analyses of the proportions of P14 cells from different origins obtained from transplanted tumor mass. The numbers adjacent to the outlined areas indicate the percentage of P14 cells originated from donor (CD45.1⁺CD45.2⁻) or recipient group (CD45.1⁺CD45.2⁺). Gated on CD44⁺CD45.1⁺P14 cells. (E) Numeric analyses of the fold changes of receptor to donor-derived P14 cells ($n \geq 4$ /group) upon treatment of anti-PD-L1. (F) Statistic analyses of the cell number of P14 cells from different origins as described in (D) ($n \geq 4$ /group).

(G) Numeric analyses of total activated P14 cells in TdLNs ($n = 7$ /group) and tumor/g ($n = 7$ /group) of Ctrl and anti-PD-L1 treatment group, with or without lymphadenectomy as described in Figure S7J.

(H) Frequencies of BrdU⁺ CD44⁺ P14 cells derived from the TdLNs ($n = 7$ /group), PBMC ($n = 7$ /group), and TME ($n = 7$ /group) of tumor-bearing mice treated with Ctrl or anti-PD-L1 as described in Figure S7J.

(I and J) Anti-PD-L1 administration combined with lymphadenectomy (I). Tumor volume curve and tumor weight for indicated group ($n = 5$ /group) (J).

(K and L) Anti-PD-L1 administration combined with lymphadenectomy at indicated time points (K). Tumor volume curve and tumor weight for indicated group ($n = 7$ or 8/group) (L).

(M and N) Administration of anti-PD-L1 or anti-CTLA4 through different routes, including intraperitoneal (i.p.), intratumoral (i.t.), and intranodal (tumor-draining LN, i.n.) injection, at indicated time points (M). Tumor volume curve and tumor weight for indicated group ($n \geq 7$ /group) (N).

(O and P) Anti-PD-L1 administration combined with bulk TdLN-T_{TSM} or TdLN-T_{PEX} cells adoptive transfer in TdLNs removed mice (O). Tumor volume curve and tumor weight for indicated group ($n = 9$ or 10/group) (P).

* $p < 0.05$, ** $p < 0.01$, and *** $p < 0.001$ versus control, ns stands for not significant, one-way ANOVA (right panel of J, L, N, and P) and two-way ANOVA analysis (left panel of J, L, N, and P). Data are representative of ≥ 2 independent experiments (mean \pm SEM).

See also Figures S6 and S7.

anti-tumor efficacy in tumor-bearing mice with lymphadenectomy (Figure 7P). These results together illuminated the importance of T_{TSM} cells in responding to PD-L1 ICB in TdLNs.

DISCUSSION

In this study, we identified TCF1⁺TOX⁻ tumor-specific memory T (T_{TSM}) cells as a distinct subset of T_{MEM} cells specifically developed in the TdLN during tumorigenesis. The unique characteristics of primordial differentiation and epigenetic landscapes distinguished TdLN-T_{TSM} cells from conventional T_{MEM} cells.

Tumor-specific TCF1⁺TOX⁻T_{TSM} and TCF1⁺TOX⁺T_{PEX} cells were both found in TdLN in K/P LUAD models (Connolly et al., 2021; Schenkel et al., 2021), supporting conclusions with subcutaneous B16.Gp models. The proportion of TdLN-T_{TSM} cells seemed to be lower in K/P LUAD models than that in B16.Gp models, particularly at late stage of tumor progression, which may be attributed to the differential antigen priming or presentation in TdLN of different tumor models. In K/P LUAD models, tumorigenesis was induced by lentiviral administration of Cre recombinase to the lung tissues of K/P mice, which also concomitantly transduced antigen-presenting cells (APCs), resulting in antigen expression by these transduced APCs per se (DuPage et al., 2011; Fitzgerald et al., 2021) that directly presented tumor antigens to tumor-specific CD8⁺ T cells in TdLN prior to the onset of tumor lesions. Furthermore, at very late stage (like week 17) of tumor progression in K/P LUAD tumor model, tumor may metastasize to TdLN (Connolly et al., 2021; DuPage et al., 2011), which likely profoundly impact the differentiation and composition of tumor-specific CD8⁺ T cells in TdLN.

TdLN-residing T_{TSM} cells are fundamentally different from TdLN-T_{PEX} cells and TME-T_{PEX} and T_{EX} cells at the transcriptional and epigenetic levels. TdLN-T_{TSM} cells do not express exhaustion-specific TF TOX (Alfei et al., 2019; Khan et al., 2019; Scott et al., 2019; Yao et al., 2019). More remarkably, in contrast to TdLN-T_{PEX} cells, TdLN-T_{TSM} cells were free of epigenetic scars at the regions of key genes regulating T cell exhaustion, such as *Tox* and *Pdcdf* (Abdel-Hakeem et al., 2021; Tonnerre et al., 2021; Yates et al., 2021). Thus, TdLN-T_{TSM} cells could differentiate into fully competent effector T cells as canonical T_{MEM} cells. Together, these features establish TdLN-T_{TSM} cells as a bona fide T_{MEM} subset induced early during tumorigenesis. The molecular signals governing the primordial differentiation of T_{TSM} cells in the TdLN warrant further investigation.

This study provides compelling evidence to support the notion that TdLN-T_{TSM} cells function as primary responders for PD-1/PD-L1 ICB. First, PD-L1 ICB efficiently expanded TdLN-T_{TSM} cells, leading to the subsequent accumulation of T_{PEX} and T_{EX} cells in the TME. Second, i.n. administration of anti-PD-L1 mAb to the TdLN effectively restrained tumor growth, whereas i.t. injection of the PD-L1 mAb did not achieve appreciable tumor control. Third, surgical removal of the TdLN abolished the anti-tumor efficacy of PD-L1 ICB, while adoptive transfer of TdLN-T_{TSM} cells restored the tumor control in TdLN-resected recipients. Based on these points, we propose that PD-1/PD-L1 ICB may exert anti-tumor effects in a temporal and spatial manner: it first expands T_{TSM} cells and further drives these cells to differentiate into T_{PEX} cells in

TdLN; subsequently, TdLN-derived T_{PEX} cells migrate to the periphery and finally differentiate into T_{EX} cells in the TME, whereby ICB may sustain the effector function of these newly differentiated T_{EX} cells to effectively execute tumor cells. However, such hypothesis needs to be further validated in preclinical tumor models and ICB responding cancer patients.

In conclusion, we identified the primordially differentiated T_{TSM} subset in the TdLN, which served as bona fide responders to PD-1/PD-L1 ICB. These findings provide an important rationale for harnessing TdLN-T_{TSM} cells to potentiate ICB-based anti-tumor immunotherapy.

Limitations of the study

In this study, we did not characterize TdLN-T_{TSM} cells in non-HCC human cancers. Additionally, the mechanisms underlying primordial TdLN-T_{TSM} differentiation were not characterized. Furthermore, TdLN-T_{TSM} cells as responders to PD-1/PD-L1 ICB in human cancer patients were not investigated.

STAR★METHODS

Detailed methods are provided in the online version of this paper and include the following:

- **KEY RESOURCES TABLE**
- **RESOURCE AVAILABILITY**
 - Lead contact
 - Materials availability
 - Data and code availability
- **EXPERIMENTAL MODEL AND SUBJECT DETAILS**
 - Mice
 - Cell lines
 - Patients and tissue samples
 - Mouse tumor models
 - Infection models
- **METHOD DETAILS**
 - Cell sorting and adoptive T cell transfer
 - *In vivo* antibody treatment
 - Listeria monocytogenes (Lm) protection assay
 - Mice lymphadenectomy and tumor transplantation
 - Preparation of single cell suspensions from mouse samples
 - Cytokine detection, antibodies, dyes, flow cytometry and cell sorting
 - TCR validation and ELISpot assay
 - 3' single-cell RNA-seq library preparation for mouse T cells
 - ATAC-seq library preparation
 - Single cell dissociation from fresh human biopsies
 - Isolation of tumor reactive CD8⁺ T cells from the TME and TdLN
 - 5' single cell RNA-seq and immune profiling with patient cells
- **QUANTIFICATION AND STATISTICAL ANALYSIS**
 - Pre-processing of single cell RNA-seq data
 - Dimension reduction and unsupervised clustering
 - Identification of differentially expressed genes
 - Annotation of cell clusters

- Re-clustering of TdLN-CD8⁺ T cells and memory CD8⁺ T cells
- Identifying cells with active gene sets
- T cell receptor data analysis
- Reconstruction of TCR sequences from scRNA-seq data
- Building single-cell trajectory
- Analysis pipeline of bulk ATAC-seq data
- Gene ontology enrichment analysis
- Motif enrichment analysis
- Statistical analysis

SUPPLEMENTAL INFORMATION

Supplemental information can be found online at <https://doi.org/10.1016/j.cell.2022.09.020>.

ACKNOWLEDGMENTS

We thank Miss Jing Zhao at the core facility center of Third Military Medical University for performing cell sorting. Jiayin Biotechnology Ltd. (Shanghai, China) performed scRNA-seq and ATAC-seq. We appreciate the technical supports from Dr. Lin Chen, Dr. Shiping Jiao, and Dr. Ge Meng from the Department of Hepatobiliary Surgery, Affiliated Drum Tower Hospital of Medical School of Nanjing University. This work was in part supported by Beijing Changping Laboratory. This study was supported by grants from the Key Program of National Natural Science Foundation of China (no. 32030041 to L.Y.), the National Natural Science Fund for Distinguished Young Scholars (no. 31825011 to L.Y.), the National Key R&D Program of China (no. 2020YFA0803300 to Z.T.), National Science Foundation for Outstanding Young Scholars of China (no. 82122028 to L.X.), and the National Natural Science Foundation of China (no. 31900643 to Q.H. and no. 31900656 to Z.W.).

AUTHOR CONTRIBUTIONS

Q.H. and Z.W. performed the experiments and analyzed the data with X.C., L.W., Y.L., Q.L., H.L., J.G., S.W., X.Y., Z.Y., S.L., Q.W., L.R., L.Y.X., Y.W., L.G., Q.T., and X.Z.

X.W., D.X., W.D., Y.T., and Y.Y., supervised by Z.T., processed and analyzed scRNA-seq and ATAC-seq data. B.S., L.X., Z.T., and L.Y. conceived, designed, and supervised the project and contributed equally to this work. Q.H., X.W., L.X., Z.T., and L.Y. wrote the manuscript, with all authors contributing to the revision of the manuscript.

DECLARATION OF INTERESTS

L.X. has filed a patent on the therapeutic usage of TdLN-T_{TSM} cells for adoptive T cell therapy with National Intellectual Property Administration of China.

Received: October 18, 2021

Revised: July 8, 2022

Accepted: September 7, 2022

Published: October 7, 2022

REFERENCES

- Abdel-Hakeem, M.S., Manne, S., Beltra, J.C., Stelekati, E., Chen, Z., Nzanga, K., Ali, M.A., Johnson, J.L., Giles, J.R., Mathew, D., et al. (2021). Epigenetic scarring of exhausted T cells hinders memory differentiation upon eliminating chronic antigenic stimulation. *Nat. Immunol.* 22, 1008–1019.
- Ahmed, R., and Gray, D. (1996). Immunological memory and protective immunity: understanding their relation. *Science* 272, 54–60. <https://doi.org/10.1126/science.272.5258.54>.
- Aibar, S., González-Blas, C.B., Moerman, T., Huynh-Thu, V.A., Imrichova, H., Hulselmans, G., Rambow, F., Marine, J.C., Geurts, P., Aerts, J., et al. (2017). SCENIC: single-cell regulatory network inference and clustering. *Nat. Methods* 14, 1083–1086.
- Alfei, F., Kanev, K., Hofmann, M., Wu, M., Ghoneim, H.E., Roelli, P., Utzschneider, D.T., von Hoesslin, M., Cullen, J.G., Fan, Y., et al. (2019). TOX reinforces the phenotype and longevity of exhausted T cells in chronic viral infection. *Nature* 571, 265–269.
- Almoshari, Y., Ren, R., Zhang, H., Jia, Z., Wei, X., Chen, N., Li, G., Ryu, S., Lele, S.M., Reinhardt, R.A., and Wang, D. (2020). GSK3 inhibitor-loaded osteotropic pluronic hydrogel effectively mitigates periodontal tissue damage associated with experimental periodontitis. *Biomaterials* 261, 120293.
- Aran, D., Looney, A.P., Liu, L., Wu, E., Fong, V., Hsu, A., Chak, S., Naikawadi, R.P., Wolters, P.J., Abate, A.R., et al. (2019). Reference-based analysis of lung single-cell sequencing reveals a transitional profibrotic macrophage. *Nat. Immunol.* 20, 163–172.
- Becht, E., McInnes, L., Healy, J., Dutertre, C.A., Kwok, I.W.H., Ng, L.G., Ginhoux, F., and Newell, E.W. (2018). Dimensionality reduction for visualizing single-cell data using UMAP. *Nat. Biotechnol.* <https://doi.org/10.1038/nbt.4314>.
- Brahmer, J.R., Tykodi, S.S., Chow, L.Q., Hwu, W.J., Topalian, S.L., Hwu, P., Drake, C.G., Camacho, L.H., Kauh, J., Odunsi, K., et al. (2012). Safety and activity of anti-PD-L1 antibody in patients with advanced cancer. *N. Engl. J. Med.* 366, 2455–2465.
- Brochet, X., Lefranc, M.P., and Giudicelli, V. (2008). IMGT/V-QUEST: the highly customized and integrated system for IG and TR standardized V-J and V-D-J sequence analysis. *Nucleic Acids Res.* 36, W503–W508.
- Buchwald, Z.S., Nasti, T.H., Lee, J., Eberhardt, C.S., Wieland, A., Im, S.J., Lawson, D., Curran, W., Ahmed, R., and Khan, M.K. (2020). Tumor-draining lymph node is important for a robust abscopal effect stimulated by radiotherapy. *J. Immunother. Cancer* 8, e000867.
- Cao, J., Spielmann, M., Qiu, X., Huang, X., Ibrahim, D.M., Hill, A.J., Zhang, F., Mundlos, S., Christiansen, L., Steemers, F.J., et al. (2019). The single-cell transcriptional landscape of mammalian organogenesis. *Nature* 566, 496–502.
- Chamoto, K., Chowdhury, P.S., Kumar, A., Sonomura, K., Matsuda, F., Fagasan, S., and Honjo, T. (2017). Mitochondrial activation chemicals synergize with surface receptor PD-1 blockade for T cell-dependent antitumor activity. *Proc. Natl. Acad. Sci. USA* 114, E761–E770.
- Chang, J.T., Wherry, E.J., and Goldrath, A.W. (2014). Molecular regulation of effector and memory T cell differentiation. *Nat. Immunol.* 15, 1104–1115. <https://doi.org/10.1038/ni.3031>.
- Chaudhary, V., Bhatia, R.S., and Ahlawat, A.K. (2014). A novel self-organizing map (SOM) learning algorithm with nearest and farthest neurons. *Alex. Eng. J.* 53, 827–831.
- Chen, X., Cao, G., Wu, J., Wang, X., Pan, Z., Gao, J., Tian, Q., Xu, L., Li, Z., Hao, Y., et al. (2019). The histone methyltransferase EZH2 primes the early differentiation of follicular helper T cells during acute viral infection. *Cell. Mol. Immunol.* 17, 247–260.
- Chen, Z., Arai, E., Khan, O., Zhang, Z., Ngiow, S.F., He, Y., Huang, H., Manne, S., Cao, Z., Baxter, A.E., et al. (2021). In vivo CD8⁺ T cell CRISPR screening reveals control by Fli1 in infection and cancer. *Cell* 184, 1262–1280.e22.
- Cohen, C.J., Zhao, Y., Zheng, Z., Rosenberg, S.A., and Morgan, R.A. (2006). Enhanced antitumor activity of murine-human hybrid T-cell receptor (TCR) in human lymphocytes is associated with improved pairing and TCR/CD3 stability. *Cancer Res.* 66, 8878–8886.
- Connolly, K.A., Kuchroo, M., Venkat, A., Khatun, A., Wang, J., William, I., Hornick, N.I., Fitzgerald, B.L., Damo, M., Kasmani, M.Y., et al. (2021). A reservoir of stem-like CD8(+) T cells in the tumor-draining lymph node preserves the ongoing antitumor immune response. *Sci. Immunol.* 6, eabg7836. 78. <https://doi.org/10.1126/sciimmunol.abg7836>.
- Dammeijer, F., van Gulijk, M., Mulder, E.E., Lukkes, M., Klaasse, L., van den Bosch, T., van Nimwegen, M., Lau, S.P., Latupeirissa, K., Schetters, S., et al. (2020). The PD-1/PD-L1-checkpoint restrains T cell immunity in tumor-draining lymph nodes. *Cancer Cell* 38, 685–700.e8.

- Draper, L.M., Kwong, M.L., Gros, A., Stevanović, S., Tran, E., Kerkar, S., Raffeld, M., Rosenberg, S.A., and Hinrichs, C.S. (2015). Targeting of HPV-16+ epithelial cancer cells by TCR gene engineered T cells directed against E6. *Clin. Cancer Res.* 21, 4431–4439.
- DuPage, M., Cheung, A.F., Mazumdar, C., Winslow, M.M., Bronson, R., Schmidt, L.M., Crowley, D., Chen, J., and Jacks, T. (2011). Endogenous T cell responses to antigens expressed in lung adenocarcinomas delay malignant tumor progression. *Cancer Cell* 19, 72–85.
- DuPage, M., Dooley, A.L., and Jacks, T. (2009). Conditional mouse lung cancer models using adenoviral or lentiviral delivery of Cre recombinase. *Nat. Protoc.* 4, 1064–1072.
- Feng, X., Wang, H., Takata, H., Day, T.J., Willen, J., and Hu, H. (2011). Transcription factor Foxp1 exerts essential cell-intrinsic regulation of the quiescence of naive T cells. *Nat. Immunol.* 12, 544–550.
- Finak, G., McDavid, A., Yajima, M., Deng, J., Gersuk, V., Shalek, A.K., Slichter, C.K., Miller, H.W., McElrath, M.J., Prlic, M., et al. (2015). MAST: a flexible statistical framework for assessing transcriptional changes and characterizing heterogeneity in single-cell RNA sequencing data. *Genome Biol.* 16, 278.
- Fitzgerald, B., Connolly, K.A., Cui, C., Fagerberg, E., Mariuzza, D.L., Hornick, N.I., Foster, G.G., William, I., Cheung, J.F., and Joshi, N.S. (2021). A mouse model for the study of anti-tumor T cell responses in Kras-driven lung adenocarcinoma. *Cell Rep. Methods* 1, 100080.
- Francis, D.M., Manspeaker, M.P., Schudel, A., Sestito, L.F., O'Melia, M.J., Kissick, H.T., Pollack, B.P., Waller, E.K., and Thomas, S.N. (2020). Blockade of immune checkpoints in lymph nodes through locoregional delivery augments cancer immunotherapy. *Sci. Transl. Med.* 12, eaay3575. <https://doi.org/10.1126/scitranslmed.aay3575>.
- Fransen, M.F., Schoonderwoerd, M., Knopf, P., Camps, M.G., Hawinkels, L.J., Kneilling, M., van Hall, T., and Ossendorp, F. (2018). Tumor-draining lymph nodes are pivotal in PD-1/PD-L1 checkpoint therapy. *JCI Insight* 3, e124507.
- Hashimoto, M., Kamphorst, A.O., Im, S.J., Kissick, H.T., Pillai, R.N., Ramalingam, S.S., Araki, K., and Ahmed, R. (2018). CD8 T cell exhaustion in chronic infection and cancer: opportunities for interventions. *Annu. Rev. Med.* 69, 301–318.
- He, R., Hou, S., Liu, C., Zhang, A., Bai, Q., Han, M., Yang, Y., Wei, G., Shen, T., Yang, X., et al. (2016). Follicular CXCR5-expressing CD8(+) T cells curtail chronic viral infection. *Nature* 537, 412–428.
- Hudson, W.H., Gensheimer, J., Hashimoto, M., Wieland, A., Valanparambil, R.M., Li, P., Lin, J.X., Konieczny, B.T., Im, S.J., Freeman, G.J., et al. (2019). Proliferating transitory T cells with an effector-like transcriptional signature emerge from PD-1(+) stem-like CD8(+) T cells during chronic infection. *Immunity* 51, 1043–1058.e4.
- Ilicic, T., Kim, J.K., Kolodziejczyk, A.A., Bagger, F.O., McCarthy, D.J., Marioni, J.C., and Teichmann, S.A. (2016). Classification of low quality cells from single-cell RNA-seq data. *Genome Biol.* 17, 29. <https://doi.org/10.1186/s13059-016-0888-1>.
- Im, S.J., Hashimoto, M., Gerner, M.Y., Lee, J., Kissick, H.T., Burger, M.C., Shan, Q., Hale, J.S., Lee, J., Nasti, T.H., et al. (2016). Defining CD8+ T cells that provide the proliferative burst after PD-1 therapy. *Nature* 537, 417–421.
- Jadhav, R.R., Im, S.J., Hu, B., Hashimoto, M., Li, P., Lin, J.X., Leonard, W.J., Greenleaf, W.J., Ahmed, R., and Goronzy, J.J. (2019). Epigenetic signature of PD-1+ TCF1+ CD8 T cells that act as resource cells during chronic viral infection and respond to PD-1 blockade. *Proc. Natl. Acad. Sci. USA* 116, 14113–14118.
- Jin, B.Y., Campbell, T.E., Draper, L.M., Stevanović, S., Weissbrich, B., Yu, Z., Restifo, N.P., Rosenberg, S.A., Trimble, C.L., and Hinrichs, C.S. (2018). Engineered T cells targeting E7 mediate regression of human papillomavirus cancers in a murine model. *JCI Insight* 3, e99488.
- Kaech, S.M., and Cui, W. (2012). Transcriptional control of effector and memory CD8+ T cell differentiation. *Nat. Rev. Immunol.* 12, 749–761.
- Kaech, S.M., and Wherry, E.J. (2007). Heterogeneity and cell-fate decisions in effector and memory CD8+ T cell differentiation during viral infection. *Immunity* 27, 393–405.
- Kallies, A., Zehn, D., and Utzschneider, D.T. (2020). Precursor exhausted T cells: key to successful immunotherapy? *Nat. Rev. Immunol.* 20, 128–136.
- Khan, O., Giles, J.R., McDonald, S., Marne, S., Ngiov, S.F., Patel, K.P., Werner, M.T., Huang, A.C., Alexander, K.A., Wu, J.E., et al. (2019). TOX transcriptionally and epigenetically programs CD8+ T cell exhaustion. *Nature* 571, 211–218.
- Kim, M., Hosmane, N.N., Bullen, C.K., Capoferra, A., Yang, H.C., Siliciano, J.D., and Siliciano, R.F. (2014). A primary CD4(+) T cell model of HIV-1 latency established after activation through the T cell receptor and subsequent return to quiescence. *Nat. Protoc.* 9, 2755–2770.
- Korsunsky, I., Millard, N., Fan, J., Slowikowski, K., Zhang, F., Wei, K., Baglaenko, Y., Brenner, M., Loh, P.R., and Raychaudhuri, S. (2019). Fast, sensitive and accurate integration of single-cell data with harmony. *Nat. Methods* 16, 1289–1296. <https://doi.org/10.1038/s41592-41019-40619-41590>.
- Krishna, S., Lowery, F.J., Copeland, A.R., Bahadiroglu, E., Mukherjee, R., Jia, L., Anibal, J.T., Sachs, A., Adebola, S.O., Gurusamy, D., et al. (2020). Stem-like CD8 T cells mediate response of adoptive cell immunotherapy against human cancer. *Science* 370, 1328–1334.
- Kurtulus, S., Madi, A., Escobar, G., Klapholz, M., Nyman, J., Christian, E., Pawlak, M., Dionne, D., Xia, J., Rozenblatt-Rosen, O., et al. (2018). Checkpoint blockade immunotherapy induces dynamic changes in PD-1-CD8+ tumor-infiltrating T cells. *Immunity* 50, 181–194.e6.
- Leong, Y.A., Chen, Y., Ong, H.S., Wu, D., Man, K., Deleage, C., Minnich, M., Meckiff, B.J., Wei, Y., Hou, Z., et al. (2016). CXCR5+ follicular cytotoxic T cells control viral infection in B cell follicles. *Nat. Immunol.* 17, 1187–1196.
- Li, H., and Durbin, R. (2009). Fast and accurate short read alignment with Burrows-Wheeler transform. *Bioinformatics* 25, 1754–1760. <https://doi.org/10.1093/bioinformatics/btp1324>.
- Li, Y., Wang, Z., Lin, H., Wang, L., Chen, X., Liu, Q., Zuo, Q., Hu, J., Wang, H., Guo, J., et al. (2020). Bcl6 preserves the suppressive function of regulatory T cells during tumorigenesis. *Front. Immunol.* 11, 806.
- Love, M.I., Huber, W., and Anders, S. (2014). Moderated estimation of fold change and dispersion for RNA-seq data with DESeq2. *Genome Biol.* 15, 550.
- Machanick, P., and Bailey, T.L. (2011). MEME-ChIP: motif analysis of large DNA datasets. *Bioinformatics* 27, 1696–1697.
- Marçais, A., Tomkowiak, M., Walzer, T., Coupet, C.A., Ravel-Chapuis, A., and Marvel, J. (2006). Maintenance of CCL5 mRNA stores by post-effector and memory CD8 T cells is dependent on transcription and is coupled to increased mRNA stability. *Eur. J. Immunol.* 36, 2745–2754.
- Martinez, G.J., Pereira, R.M., Aijo, T., Kim, E.Y., Marangoni, F., Pipkin, M.E., Toher, S., Heissmeyer, V., Zhang, Y.C., Crotty, S., et al. (2015). The transcription factor NFAT promotes exhaustion of activated CD8+ T cells. *Immunity* 42, 265–278. <https://doi.org/10.1016/j.jimmuni.2015.01.006>.
- McLane, L.M., Abdel-Hakeem, M.S., and Wherry, E.J. (2019). CD8 T cell exhaustion during chronic viral infection and cancer. *Annu. Rev. Immunol.* 37, 457–495.
- McLean, C.Y., Bristor, D., Hiller, M., Clarke, S.L., Schaer, B.T., Lowe, C.B., Wenger, A.M., and Bejerano, G. (2010). GREAT improves functional interpretation of cis-regulatory regions. *Nat. Biotechnol.* 28, 495–501.
- Melero, I., Castanon, E., Alvarez, M., Champiat, S., and Marabelle, A. (2021). Intratumoural administration and tumour tissue targeting of cancer immunotherapies. *Nat. Rev. Clin. Oncol.* 18, 558–576.
- Miller, B.C., Sen, D.R., Al Abosy, R., Bi, K., Virkud, Y.V., LaFleur, M.W., Yates, K.B., Lako, A., Felt, K., Naik, G.S., et al. (2019). Subsets of exhausted CD8+ T cells differentially mediate tumor control and respond to checkpoint blockade. *Nat. Immunol.* 20, 326–336.
- Paley, M.A., Kroy, D.C., Odorizzi, P.M., Johnnidis, J.B., Dolfi, D.V., Barnett, B.E., Bikoff, E.K., Robertson, E.J., Lauer, G.M., Reiner, S.L., and Wherry, E.J. (2012). Progenitor and terminal subsets of CD8+ T cells cooperate to contain chronic viral infection. *Science* 338, 1220–1225.
- Philip, M., and Schietinger, A. (2022). CD8+ T cell differentiation and dysfunction in cancer. *Nat. Rev. Immunol.* 22, 209–223.

- Quinlan, A.R., and Hall, I.M. (2010). BEDTools: a flexible suite of utilities for comparing genomic features. *Bioinformatics* 26, 841–842. <https://doi.org/10.1093/bioinformatics/btq033>.
- Sade-Feldman, M., Yizhak, K., Bjorgaard, S.L., Ray, J.P., de Boer, C.G., Jenkins, R.W., Lieb, D.J., Chen, J.H., Frederick, D.T., Barzily-Rokni, M., et al. (2018). Defining T cell states associated with response to checkpoint immunotherapy in melanoma. *Cell* 176, 404. 10. <https://doi.org/10.1016/j.cell.2018.1010.1038>.
- Schenkel, J.M., Herbst, R.H., Canner, D., Li, A., Hillman, M., Shanahan, S.-L., Gibbons, G., Smith, O.C., Kim, J.Y., Westcott, P., et al. (2021). Conventional type I dendritic cells maintain a reservoir of proliferative tumor-antigen specific TCF1+ CD8+ T cells in tumor-draining lymph nodes. *Immunity* 54, 2338–2353.e6.
- Scott, A.C., Dündar, F., Zumbo, P., Chandran, S.S., Klebanoff, C.A., Shakiba, M., Trivedi, P., Menocal, L., Appleby, H., Camara, S., et al. (2019). TOX is a critical regulator of tumour-specific T cell differentiation. *Nature* 571, 270–274.
- Seo, H., Chen, J., Gonzalez-Avalos, E., Samaniego-Castruita, D., Das, A., Wang, Y.H., Lopez-Moyado, I.F., Georges, R.O., Zhang, W., Onodera, A., et al. (2019). TOX and TOX2 transcription factors cooperate with NR4A transcription factors to impose CD8+ T cell exhaustion. *Proc. Natl. Acad. Sci. USA* 116, 12410–12415. <https://doi.org/10.11073/pnas.1905675116>.
- Sharma, P., and Allison, J.P. (2015). The future of immune checkpoint therapy. *Science* 348, 56–61. <https://doi.org/10.1126/science.aaa8172>.
- Siddiqui, I., Schaeuble, K., Chennupati, V., Fuertes Marraco, S.A., Calderon-Copete, S., Pais Ferreira, D., Carmona, S.J., Scarpellino, L., Gfeller, D., Pradervand, S., et al. (2019). Intratumoral Tcf1+PD-1+CD8+ T cells with stem-like properties promote tumor control in response to vaccination and checkpoint blockade immunotherapy. *Immunity* 50, 195–211.e10. <https://doi.org/10.1016/j.immuni.2018.12.021>.
- Simoni, Y., Becht, E., Fehlings, M., Loh, C.Y., Koo, S.L., Teng, K.W.W., Yeong, J.P.S., Nahar, R., Zhang, T., Kared, H., et al. (2018). Bystander CD8+ T cells are abundant and phenotypically distinct in human tumour infiltrates. *Nature* 557, 575–579.
- Spitzer, M.H., Carmi, Y., Reticker-Flynn, N.E., Kwek, S.S., Madhireddy, D., Martins, M.M., Gherardini, P.F., Prestwood, T.R., Chabon, J., Bendall, S.C., et al. (2017). Systemic immunity is required for effective cancer immunotherapy. *Cell* 168, 487–502.e15.
- Stuart, T., Butler, A., Hoffman, P., Hafemeister, C., Papalexi, E., Mauck, W.M., 3rd, Hao, Y., Stoeckius, M., Smibert, P., and Satija, R. (2019). Comprehensive integration of single-cell data. *Cell* 177, 1888–1902.e21.
- Stubbington, M.J.T., Lönnberg, T., Proserpio, V., Clare, S., Speak, A.O., Dougan, G., and Teichmann, S.A. (2016). T cell fate and clonality inference from single-cell transcriptomes. *Nat. Methods* 13, 329–332.
- Tonnerre, P., Wolksi, D., Subudhi, S., Aljabban, J., Hoogeveen, R.C., Damasio, M., Drescher, H.K., Bartsch, L.M., Tully, D.C., Sen, D.R., et al. (2021). Differentiation of exhausted CD8(+) T cells after termination of chronic antigen stimulation stops short of achieving functional T cell memory. *Nat. Immunol.* 22, 1030–1041. <https://doi.org/10.1038/s41590-41021-00982-6>.
- Topalian, S.L., Hodi, F.S., Brahmer, J.R., Gettinger, S.N., Smith, D.C., McDermott, D.F., Powderly, J.D., Carvajal, R.D., Sosman, J.A., Atkins, M.B., et al. (2012). Safety, activity, and immune correlates of anti-PD-1 antibody in cancer. *N. Engl. J. Med.* 366, 2443–2454. <https://doi.org/10.1056/NEJMoa1200690>.
- Tvinnereim, A.R., Hamilton, S.E., and Harty, J.T. (2002). CD8+-T-cell response to secreted and nonsecreted antigens delivered by recombinant *Listeria monocytogenes* during secondary infection. *Infect. Immun.* 70, 153–162.
- Utzschneider, D.T., Charmoy, M., Chennupati, V., Pousse, L., Ferreira, D.P., Calderon-Copete, S., Danilo, M., Alfei, F., Hofmann, M., Wieland, D., et al. (2016). T cell factor 1-expressing memory-like CD8(+) T cells sustain the immune response to chronic viral infections. *Immunity* 45, 415–427.
- Wang, L., Wang, Z., Guo, J., Lin, H., Wen, S., Liu, Q., Li, Y., Wu, Q., Gao, L., Chen, X., et al. (2021). Tumor transplantation for assessing the dynamics of tumor-infiltrating CD8+ T cells in mice. *J. Vis. Exp.*, e62442.
- Wang, Y., Hu, J., Li, Y., Xiao, M., Wang, H., Tian, Q., Li, Z., Tang, J., Hu, L., Tan, Y., et al. (2019). The transcription factor TCF1 preserves the effector function of exhausted CD8 T cells during chronic viral infection. *Front. Immunol.* 10, 169.
- Wherry, E.J. (2011). T cell exhaustion. *Nat. Immunol.* 12, 492–499.
- Woo, E.Y., Chu, C.S., Goletz, T.J., Schlienger, K., Yeh, H., Coukos, G., Rubin, S.C., Kaiser, L.R., and June, C.H. (2001). Regulatory CD4(+)CD25(+) T cells in tumors from patients with early-stage non-small cell lung cancer and late-stage ovarian cancer. *Cancer Res.* 61, 4766–4772.
- Wu, T., Ji, Y., Moseman, E.A., Xu, H.C., Mangani, M., Kirby, M., Anderson, S.M., Handon, R., Kenyon, E., Elkahloun, A., et al. (2016). The TCF1-Bcl6 axis counteracts type I interferon to repress exhaustion and maintain T cell stemness. *Sci. Immunol.* 1, eaai8593. <https://doi.org/10.1126/sciimmunol.aai8593>.
- Wu, T.D., Madireddi, S., de Almeida, P.E., Banchereau, R., Chen, Y.J., Chitre, A.S., Chiang, E.Y., Iftikhar, H., O'Gorman, W.E., Au-Yeung, A., et al. (2020). Peripheral T cell expansion predicts tumour infiltration and clinical response. *Nature* 579, 274–278.
- Xiong, Q., Peng, C., Yan, X., Yan, X., Chen, L., Sun, B., and Jiao, S. (2020). Characteristics of SARS-CoV-2-specific cytotoxic T cells revealed by single-cell immune profiling of longitudinal COVID-19 blood samples. *Signal Transduct. Target. Ther.* 5, 285.
- Yao, C., Sun, H.W., Lacey, N.E., Ji, Y., Moseman, E.A., Shih, H.Y., Heuston, E.F., Kirby, M., Anderson, S., Cheng, J., et al. (2019). Single-cell RNA-seq reveals TOX as a key regulator of CD8+ T cell persistence in chronic infection. *Nat. Immunol.* 20, 890–901.
- Yates, K.B., Tonnerre, P., Martin, G.E., Gerdemann, U., Al Abosy, R., Comstock, D.E., Weiss, S.A., Wolksi, D., Tully, D.C., Chung, R.T., et al. (2021). Epigenetic scars of CD8+ T cell exhaustion persist after cure of chronic infection in humans. *Nat. Immunol.* 22, 1020–1029.
- Yost, K.E., Satpathy, A.T., Wells, D.K., Qi, Y., Wang, C., Kageyama, R., McNamara, K.L., Granja, J.M., Sarin, K.Y., Brown, R.A., et al. (2019). Clonal replacement of tumor-specific T cells following PD-1 blockade. *Nat. Med.* 25, 1251–1259.
- Zhang, Y., Liu, T., Meyer, C.A., Eeckhoute, J., Johnson, D.S., Bernstein, B.E., Nusbaum, C., Myers, R.M., Brown, M., Li, W., and Liu, X.S. (2008). Model-based analysis of ChIP-Seq (MACS). *Genome Biol.* 9, R137.
- Zhao, D.M., Yu, S., Zhou, X., Haring, J.S., Held, W., Badovinac, V.P., Harty, J.T., and Xue, H.H. (2010). Constitutive activation of Wnt signaling favors generation of memory CD8 T cells. *J. Immunol.* 184, 1191–1199.
- Zhao, X., Shan, Q., and Xue, H.H. (2022). TCF1 in T cell immunity: a broadened frontier. *Nat. Rev. Immunol.* 22, 147–157.
- Zhou, X., Yu, S., Zhao, D.M., Harty, J.T., Badovinac, V.P., and Xue, H.H. (2010). Differentiation and persistence of memory CD8(+) T cells depend on T cell factor 1. *Immunity* 33, 229–240.

STAR★METHODS

KEY RESOURCES TABLE

REAGENT or RESOURCE	SOURCE	IDENTIFIER
Antibodies		
Rat monoclonal Anti-Mouse CD8a (clone 53-6.7)	BD Biosciences	Cat# 553036; RRID: AB_394573
Rat monoclonal anti-mouse CD44 (clone IM7)	Thermofisher	Cat# 25-0441-82; RRID: AB_469623
Mouse (A.SW) monoclonal anti-mouse CD45.1 (clone A20)	Biolegend	Cat# 110714; RRID: AB_313503
Mouse (SJL) monoclonal anti-mouse CD45.2 (clone 104)	Biolegend	Cat# 109808; RRID: AB_313445
Rat monoclonal anti-mouse CD279 (PD-1) (clonDe RMP1-30)	Thermofisher	Cat# 48-9981-82; RRID: AB_11150068
Rat monoclonal anti-mouse CD366 (Tim3) (clone RMT3-23)	Biolegend	Cat# 119704; RRID: AB_345378
Rat monoclonal anti-mouse CD223 (Lag3) (clone C9B7W)	Biolegend	Cat# 125212; RRID: AB_2561517
Mouse monoclonal anti-mouse CD244.2 (2B4) (clone m2B4(B6) 458.1)	Biolegend	Cat# 133514; RRID: AB_2564341
Rat monoclonal anti-mouse CD39 (clone 24DMS1)	Thermofisher	Cat# 50-0391-82; RRID: AB_11149300
Mouse monoclonal anti-mouse CD159a (NKG2A) (clone 16A11)	Biolegend	Cat# 142804; RRID: AB_10965542
Mouse monoclonal anti-mouse Slamf6 (Ly-108) (clone 13G3-19D)	Thermofisher	Cat# 12-1508-80; RRID: AB_763616
Mouse monoclonal anti-mouse CX3CR1 (clone SA011F11)	Biolegend	Cat# 149006; RRID: AB_2564315
Syrian Hamster monoclonal anti-mouse KLRG1 (clone 2F1)	Biolegend	Cat# 138414; RRID: AB_2565613
Armenian Hamster monoclonal anti-mouse CD69 (clone H1.2F3)	BD Biosciences	Cat# 553236; RRID: AB_396675
Mouse monoclonal anti-mouse CCL5 (clone 2E9)	Biolegend	Cat# 149104; RRID: AB_2564406
Rat monoclonal anti-mouse CD62L (clone MEL-14)	Thermofisher	Cat# 17-0621-82; RRID: AB_469410
Rat monoclonal anti-mouse CD127 (IL-7R α) (clone A7R34)	Biolegend	Cat# 135027; RRID: AB_2563103
Rat monoclonal anti-mouse CD122 (IL-2R β) (clone TM- β 1)	Biolegend	Cat# 123210; RRID: AB_940617
Armenian Hamster monoclonal anti-mouse/Rat/human CD27 (clone LG.3A10)	Biolegend	Cat# 124218; RRID: AB_2561546
Mouse monoclonal anti-mouse/human T-bet (clone 4B10)	Biolegend	Cat# 644816; RRID: AB_10959653
Rat monoclonal anti-mouse Eomes (clone Dan11mag)	Thermofisher	Cat# 12-4875-82; RRID: AB_1603275
Rat monoclonal anti-mouse/human TOX (clone TXRX10)	Thermofisher	Cat# 50-6502-82 RRID: AB_2574265
Mouse monoclonal anti-mouse Bcl-2 (clone BCL/10C4)	Biolegend	Cat# 633508; RRID: AB_2290367

(Continued on next page)

Continued

REAGENT or RESOURCE	SOURCE	IDENTIFIER
Mouse monoclonal anti-mouse/human Bcl-xL (clone 7B2.5)	Thermofisher	Cat# MA5-28638; RRID: AB_2745597
Rat monoclonal anti-mouse Ki67 (clone 16A8)	Biolegend	Cat# 652404; RRID: AB_2561525
Rat monoclonal anti-mouse CD107a/CD107b (clone 1D4B; clone M3/84)	BD Biosciences	Cat# 553793/ Cat# 553323; RRID: AB_395057/AB_394781
Rat monoclonal anti-mouse IFN-γ (clone XMG1.2)	Biolegend	Cat# 505830; RRID: AB_2563105
Rat monoclonal anti-mouse TNFα (clone MP6-XT22)	Thermofisher	Cat# 25-7321-82; RRID: AB_11042728
Armenian Hamster monoclonal anti-mouse TCR β chain (clone MP6-XT22)	Biolegend	Cat# 109208; RRID: AB_313431
Mouse monoclonal anti-mouse granzyme B (clone QA16A02)	Biolegend	Cat# 372220; RRID: AB_2728387
H-2K ^b OVA-Tetramer-SIINFEKL	MBL	Cat# TS-5001-2C
Rabbit monoclonal anti-mouse/human TCF1 (clone C46C7)	Cell Signalling Technology	Cat# 2206S; RRID: AB_2199300
Donkey anti-Rabbit Polyclonal IgG (H+L) Highly Cross-Adsorbed Secondary Antibody	Thermofisher	Cat# A-21206; RRID: AB_2535792
Mouse monoclonal anti-human CD45RA (clone HI100)	Biolegend	Cat# 304123; RRID: AB_2174122
Mouse monoclonal anti-human PD-1 (clone EH12.2H7)	Biolegend	Cat# 329906; RRID: AB_940483
Mouse monoclonal anti-human CD8a (clone HIT8a)	Biolegend	Cat# 300912; RRID: AB_314116
Mouse monoclonal anti-human CD197(CCR7) (clone G043H7)	Biolegend	Cat# 353242; RRID: AB_2564546
Mouse monoclonal anti-human CD39 (clone A1)	Biolegend	Cat# 328212; RRID: AB_2099950
Mouse monoclonal Anti-Human CD137(4-1BB)	Biolegend	Cat# 309810; RRID: AB_830672
<i>InVivoMAb</i> anti-mouse PD-L1 (B7-H1) (clone 10F.9G2)	BioXCell	Cat# BE0101; RRID: AB_10949073
<i>InVivoMAb</i> anti-mouse PD-1 (CD279) (clone RMP1-14)	BioXCell	Cat# BP0146; RRID: AB_10949053

Bacterial and virus strains

LCMV Armstrong	R. Ahmed	Grew up in house
LCMV Clone 13	R. Ahmed	Grew up in house
<i>Listeria Monocytogenes</i> -GP33-41 (Lm-GP)	Xinyuan Zhou	Grew up in house

Biological samples

Resected tumor-draining lymph nodes of 6 hepatocellular carcinoma patients	Nanjing Drum Tower Hospital, the Affiliated Hospital of Nanjing University Medical School, China	N/A
Resected tumors of 6 hepatocellular carcinoma patients	Nanjing Drum Tower Hospital, the Affiliated Hospital of Nanjing University Medical School, China	N/A

Chemicals, peptides, and recombinant proteins

Cell Proliferation Dye 450	Thermofisher	Cat# 65-0842-90
Cell Trace Violet	Thermofisher	Cat# C34557
Cyclophosphamide (CTX)	Sigma	Cat# PHR1404
Collagenase I	Worthington Biochemical	Cat# LS004197
Collagenase II	Diamond	Cat# A004174
DNase I	Sigma	Cat# 10104159001

(Continued on next page)

Continued

REAGENT or RESOURCE	SOURCE	IDENTIFIER
Golgi Plug	BD Biosciences	Cat# 555028; RRID: AB_2869013
Golgi Stop	BD Biosciences	Cat# 554724; RRID: AB_2869012
Phorbol-12-myristate-13-acetate (PMA)	EMD Millipore	Cat# 524400
Ionomycin Calcium Salt	Sigma	Cat# 13909
Poloxamer 407 (for hydrogel)	Sigma	Cat# 16758
Peptide: KAVYNFATM(GP ₃₃₋₄₁)	Chinese Peptide	Custom
ImmunoCult™ Human CD3/CD28 T Cell Activator	STEMCELL Technologies	Cat# 10971; RRID: AB_2827806
ImmunoCult™-XF T Cell Expansion Medium	STEMCELL Technologies	Cat# 10981
Human Recombinant IL-2	Sigma-Aldrich	Cat# SRP6170
Poly(I:C) (HMW) VacciGrade™	InvivoGen	Cat# vac-pic
Lipofectamine 3000 Transfection Reagent	Invitrogen	Cat# L3000015
Critical commercial assays		
Cytotix/Cytoperm Fixation/Permeabilization Kit	BD Biosciences	Cat# 554714; RRID: AB_2869008
LIVE/DEAD Fixable Near-IR Dead Cell Stain Kit	Thermo Fisher	Cat# L34975
PE Annexin V Apoptosis Detection Kit	Thermo Fisher	Cat# 88-8102-72; RRID: AB_257518
BrdU APC Flow Kit	BD Biosciences	Cat# 552598; RRID: AB_2861367
RevertAid H Minus First Strand cDNA Synthesis Kit	Thermo Fisher	Cat# K1632
RNeasy Micro Kit	QIAGEN	Cat# 74004
QuantiNova SYBR Green PCR Kit	QIAGEN	Cat# 208054
Chromium Next GEM Single Cell 5' Kit v2	10x genomics	Cat# 1000265
Chromium Single Cell Human TCR Amplification Kit	10x genomics	Cat# 1000252
Dual Index Kit TT Set A	10x genomics	Cat# 1000215
Human IFN-γ ELISpot PRO kit (HRP)	MABTECH	Cat# 3420-2HPW-2
Deposited data		
Mouse TdLN-D16 scRNA-seq	This paper	GEO: GSE180095
Mouse PBMC-D16 scRNA-seq	This paper	GEO: GSE180095
Mouse Arm-D200 scRNA-seq	This paper	GEO: GSE180095
Mouse TdLN-D4 ATAC-seq	This paper	GEO: GSE180095
Mouse TdLN-D8 ATAC-seq	This paper	GEO: GSE180095
Mouse TdLN-D21 ATAC-seq	This paper	GEO: GSE180095
Mouse TdLN-T _{PEX} ATAC-seq	This paper	GEO: GSE180095
Mouse TdLN-T _{TSM} ATAC-seq	This paper	GEO: GSE180095
Mouse CL13-D28 scRNA-seq	PMID: 30778252	GEO: GSE122713 (GSM3483809 d28_Clone13_1; GSM3483810 d28_Clone13_2)
Mouse Arm-D28 scRNA-seq	PMID: 31606264	GEO: GSE131535 (GSM3785518 D8 Arm)
Mouse TIL-D16 scRNA-seq	Unpublished	GEO: GSE152628
Mouse LN-8W scRNA-seq	PMID: 34597124	GEO: GSE182509
Mouse LN-17W scRNA-seq	PMID: 34597124	GEO: GSE182509
Mouse T _{PEX} ATAC-seq	PMID: 31227606	NCBI: PRJNA546023
Mouse T _{EX} ATAC-seq	PMID: 31227606	NCBI: PRJNA546023
Mouse T _{EFF} ATAC-seq	PMID: 31227606	NCBI: PRJNA546023
Mouse T _{MP} ATAC-seq	PMID: 31227606	NCBI: PRJNA546023
Mouse T _{MEM} ATAC-seq	PMID: 31227606	NCBI: PRJNA546023
Mouse T _{REC} ATAC-seq	PMID: 34312545	NCBI: PRJNA631919
Human TdLN scRNA-seq	This paper	CNCB-NGDC: PRJCA005518
Human TME scRNA-seq	This paper	CNCB-NGDC: PRJCA005518

(Continued on next page)

Continued

REAGENT or RESOURCE	SOURCE	IDENTIFIER
Experimental models: Cell lines		
B16F10 cells	ATCC	Cat# CRL-6475; RRID: CVCL_0159
B16.Gp cells	Beijing Biocytogen Co.Ltd, China	Custom
B16.OVA cells	ATCC	Cat# CRL-6322
MC38 cells	ATCC	RRID: CVCL_B288
HEK293T	ATCC	Cat# CRL-3216; RRID: CVCL_0063
Experimental models: Organisms/strains		
Mouse: C57BL/6J(CD45.2)	Jackson Laboratory	Stock No: 000664
Mouse: B6.SJL-Ptprc ^a Pepc ^b /BoyJ (CD45.1)	Jackson Laboratory	Stock No: 002014
Mouse: B6.129S2-Cd8a ^{tm1Mak} /J (CD8 KO)	Jackson Laboratory	Stock No: 002665
Mouse:C57BL/6-Tg(TcraTcrb)1100Mjb/J(OT-1)	Jackson Laboratory	Stock No: 003831
Mouse: B6. Tcf7-GFP knock-in mice	This paper	N/A
Mouse: B6.Cg-Tcra ^{tm1Mom} Tg(TcrLCMV)327Sdz/ TacMmjx	R. Ahmed (Emory University)/ Jackson Laboratory	Stock No: 37394
Mouse: B6.129S4-Kras ^{tm4Tyj} /J	Bo Zhong (Wuhan University)/ Jackson Laboratory	Stock No: 008179
Mouse: B6.129P2-Trp53 ^{tm1Brn} /J	Bo Zhong (Wuhan University)/ Jackson Laboratory	Stock No: 008462
Oligonucleotides		
Pdcld1 qPCR primer Forward: gcaggtaacctggtcattca	Synthesized by Invitrogen	N/A
Pdcld1 qPCR primer Reverse: caggctggtagaaaggtag	Synthesized by Invitrogen	N/A
Actb qPCR primer Aatcgctcggtacatcaaag	Synthesized by Invitrogen	N/A
Actb qPCR primer ggattccataccccaaagaagg	Synthesized by Invitrogen	N/A
Recombinant DNA		
Plasmid: Lenti-LucOS	Addgene	Cat# 22777; RRID: Addgene_22777
Plasmid: psPAX2	Addgene	Cat# 12260; RRID: Addgene_1226
Plasmid: pMD2.G	Addgene	Cat# 12259; RRID: Addgene_12259
Plasmid: pHr_PGK	Addgene	Cat# 79120; RRID: Addgene_79120
Software and algorithms		
CellRanger	10X Genomics	Version 3.1.0 https://support.10xgenomics.com/single-cell-gene-expression/software/overview/welcome
Seurat	Stuart et al., 2019	Version 3.2.3 https://cran.r-project.org/web/packages/Seurat/index.html
Harmony	Korsunsky et al., 2019	Version 1.0 https://portals.broadinstitute.org/harmony
MAST algorithm	Finak et al., 2015	http://bioconductor.org/packages/release/bioc/html/MAST.html
SingleR	Aran et al., 2019	https://bioconductor.org/packages/release/bioc/html/SingleR.html
AUCell	Aibar et al., 2017	Version 1.7.2 https://github.com/aertslab/AUCell
Bwa	Li and Durbin, 2009	Version 0.7.15 http://bio-bwa.sourceforge.net/

(Continued on next page)

Continued

REAGENT or RESOURCE	SOURCE	IDENTIFIER
Picard	Broad Institute	Version 1.107 http://broadinstitute.github.io/picard/
MACS2	Zhang et al., 2008	https://pypi.org/project/MACS2/
Bedtools	Quinlan and Hall, 2010	Version 2.25.0 https://bedtools.readthedocs.io/en/latest/index.html
DEseq2	Love et al., 2014	Version 1.30.1 https://bioconductor.org/packages/release/bioc/html/DESeq2.html
Self-Organizing Map algorithm (SOM)	Chaudhary et al., 2014	Version 0.3 https://cran.r-project.org/web/packages/som/index.html
GREAT	McLean et al., 2010	http://great.stanford.edu/public/html/
MEME-ChIP	Machanick and Bailey, 2011	https://meme-suite.org/meme/doc/meme-chip.html?man_type=web
FlowJo (Tree Star)	https://www.flowjo.com/ RRID: SCR_008520 solutions/flowjo	RRID: SCR_008520

RESOURCE AVAILABILITY**Lead contact**

Further information and requests for resources and reagents should be directed to and will be fulfilled by the lead contact, Prof. Lilin Ye (yelilinlcmv@tmmu.edu.cn).

Materials availability

Reagents generated in this study will be made available by reasonable request to the lead contact.

Data and code availability

The scRNA-seq and ATAC-seq data generated from mouse models have been deposited with the Gene Expression Omnibus (GEO: GSE180095). The accession number for the scRNA-seq data of HCC samples (sequencing raw data and processed data) in this paper are GSA (Genome Sequence Archive in BIG Data Center, Beijing Institute of Genomics, Chinese Academy of Sciences): HRA002595 (PRJCA005518). This paper additionally included analyses of publicly available scRNA-seq and ATAC-seq datasets. The accession numbers for all these datasets are listed in the [key resources table](#). Other relevant data are available from the corresponding authors upon reasonable request.

EXPERIMENTAL MODEL AND SUBJECT DETAILS**Mice**

C57BL/6J (referred as B6 mice), Cd8^{-/-} mice, OTI transgenic mice (expressing a TCR specific for the OVA₂₅₇₋₂₆₄ peptide in the context of H-2K^b), CD45.1⁺ and CD45.2⁺ congenic mice (strain B6.SJL-Ptprc^aPepc^b/BoyJ) were purchased from the Jackson Laboratories. K-ras^{LSL-G12D/+} mice and p53^{f/f} mice were gifted from Dr. Bo Zhong from Wuhan University. K-ras^{LSL-G12D/+} were crossed with p53^{f/f} mice to generate K-ras^{LSL-G12D/+}p53^{f/f} mice. P14 transgenic mice (carrying a transgenic T cell antigen receptor that recognizes H-2D^b GP₃₃₋₄₁ epitope of LCMV virus) were gifted from Dr. Rafi Ahmed (Emory University). Tcf7-GFP knock-in mice were obtained with the strategy as we previously reported ([He et al., 2016](#)). In brief, an IRES-GFP construct was inserted after the open reading frame of Tcf7 (encoding TCF-1) by homologous recombination. A Neo cassette and diphtheria toxin were used as positive and negative selection markers in the targeting vector, respectively. Targeted embryonic stem clones were injected into C57BL/6J blastocysts to generate chimeras. Tcf7-GFP knock-in reporter mice were obtained after deletion of Neo cassette by crossing with Cre-deleter mice, then bred to P14 or OT1 mice to generate P14-Tcf7-GFP or OT1-Tcf7-GFP reporter mice. All mice were kept on a C57BL/6J background. All the mice used were analyzed at 6–10 weeks of age, and both genders were included without randomization or “blinding”. All mice were housed in specific-pathogen free (SPF) condition. All mouse experiments and breeding conditions were performed in accordance with the guidelines of the Institutional Animal Care and Use Committees of the Third Military Medical University.

Cell lines

B16F10/B16.OVA cells and MC38 cells were purchased from ATCC. The LCMV CI13 glycoprotein gene knock-in B16F10 cell line (herein referred as B16.Gp) was constructed by Beijing Biocytogen Co.Ltd, China. In brief, B16.Gp was generated by

CRISPR/Cas9-mediated insertion of LCMV Clone-13 glycoprotein gene sequence into the genome of B16F10 cell line. Cells were selected in puromycin. All tumor cell lines were grown in complete DMEM-10 medium: DMEM (Gibco), 10% FBS (Gibco), 1% penicillin/ streptomycin (Gibco) and 1% L-glutamine (Gibco). For B16.Gp melanoma cells, additional 100U/ml puromycin is supplemented. T cell *in vitro* culture assays were performed with complete RPMI-1640 medium, supplemented with 10% FBS, 1% penicillin/streptomycin, 0.1% β-mercaptoethanol (Gibco) and 10 ng/ml recombinant human IL-2, otherwise indicated.

Patients and tissue samples

Six liver cancer patients (B1-B6) were enrolled and pathologically diagnosed with hepatocellular carcinoma (HCC) at Nanjing Drum Tower Hospital, the Affiliated Hospital of Nanjing University Medical School. Prior to the procedure, patients were provided informed consent for the collection of research biopsies. Fresh tumor and tumor-draining lymph nodes (TdLN) were surgically obtained from the above-described patients, following the ethical regulations approved by the Research and Ethical Committee of Nanjing Drum Tower Hospital (The Affiliated Hospital of Nanjing University Medical School). None of these patients had been diagnosed as hepatitis B, or was treated with chemotherapy or radiation before the tumor resection. The tumor stages of these patients were classified according to the guidance of Edmonson-Steiner grade. This project was conducted in accordance with the Declaration of Helsinki. The available clinical information and metadata for the samples are summarized in [Table S1](#).

Mouse tumor models

To set up mouse tumor cells, generally, the right flank of mice was shaved and half million of (0.5M) B16F10/B16.Gp cells (5×10^5), B16.OVA (5×10^5) or MC38 (5×10^5) were injected subcutaneously (s.c.). Tumors were measured every 2 days to estimate the tumor size in two dimensions with a caliper. The tumor volume was calculated according to the formula (length × width²)/2. Mice were sacrificed at the indicated time points or when the estimated tumor volume reached 2000 mm³ (endpoint) and the weight of the excised tumor mass was determined.

Besides, to generate autochthonous lung tumors in a spatiotemporally controlled fashion, we utilized a model of lung adenocarcinoma driven by the conditional expression of oncogenic K-ras^{G12D} in combination with the loss of p53. Briefly, Lung tumors were induced in K-ras^{LSL-G12D/+}-p53^{f/f} mice by intranasal inhalation of lentivirus expressing Cre recombinase as reported (hereafter called as K/P model) ([DuPage et al., 2009](#)). The lentiviral backbone Lenti-LucOS has been described previously ([DuPage et al., 2009](#)) and was purchased from Addgene (Plasmid#22777). Lentiviruses were produced by transfection of 293T cells with Lenti-LucOS, psPAX2 (gag/pol), and pMD2.G vectors at a 4:3:1 ratio ([DuPage et al., 2009](#); [Schenkel et al., 2021](#)). For tumor induction, 5×10^6 TU of Lentivirus was intranasally administrated to one mouse between 10-12 weeks of age. Generally, the induced lung tumor could be histologically confirmed at 8 weeks post lentivirus infection.

Infection models

The lymphocytic choriomeningitis virus (LCMV) Armstrong (Arm⁺) and Clone 13 (Cl13) strains were kindly provided by Dr. R. Ahmed at Emory University and propagated in our lab. Mice were intraperitoneally infected (i.p.) with 2×10^5 PFU (plaque-forming units) Armstrong or intravenously (i.v.) with 2×10^6 PFU Cl13 virus ([Wang et al., 2019](#)). Attenuated Listeria. monocytogenes expressing LCMV glycoprotein₃₃₋₄₁ (Lm-Gp) was a gift from Dr. Xinyuan Zhou (Third Military Medical University) and was created by introducing an in-frame deletion in the actA gene as described ([Tvinneim et al., 2002](#); [Zhao et al., 2010](#)) (referred to as Lm-Gp). Bacteria were grown and quantified by optical density (OD) after overnight culture in brain heart infusion (BHI) media (1 OD refers to 8×10^8 CFU (colony-forming units)) as previously reported ([Chen et al., 2021](#)). All mouse experiments and breeding conditions were performed in accordance with the guidelines of the Institutional Animal Care and Use Committees of the Third Military Medical University.

METHOD DETAILS

Cell sorting and adoptive T cell transfer

For LCMV virus infection models, 5×10^4 (for acute viral infection) or 1000 (for chronic viral infection) CD45.1⁺ naïve splenic P14-Tcf7-GFP cells were adoptively transferred into recipient mice with different congenic markers (CD45.2⁺) one day before infection.

For tumor models, tumor-bearing recipient mice were first intraperitoneally administrated with 4 mg cyclophosphamide (CTX, Sigma, PHR1404) at 6-8 days after tumor implantation when the tumor is palpable (about 3-5 mm in diameter), then 5×10^5 (otherwise indicated) naïve CD45.1⁺ splenic P14-Tcf7-GFP cells were adoptively transferred into B16.Gp tumor-bearing mice. For B16.OVA tumor model, 1×10^5 naïve CD45.1⁺ splenic OT1-Tcf7-GFP cells were adoptively transferred. For another strategy, naïve CD45.2⁺ recipient mice received CTX treatment firstly, then transferred with the same amounts of P14 or OT1 cells as above mentioned one day before tumor challenge. Otherwise indicated.

In experiments tracing cell proliferation patterns, P14 cells were labeled with proliferating-indicating dye (3 mM Celltrace Violet, 65-0842; eBioscience) according to the manufacturer's guide before adoptively transferred into recipient mice.

For sorting T_{MEM} P14 cells, CD45.1⁺CD44⁺GFP⁺CD8 T cells were generally sorted from the spleens of Armstrong infected mice at ≥ Day 60. TdLN-P14 and TME-P14 cells were sorted as CD45.1⁺CD44⁺CD8⁺GFP⁺ and CD45.1⁺CD44⁺CD8⁺PD1⁺, respectively, from B16.Gp cell-inoculated mice on Day 15 post P14-Tcf7-GFP cell transfer.

For sorting TdLN-T_{TSM}, TdLN-T_{PEX}, TME-T_{PEX} and TME-T_{EX} cells, B6 mice were first transferred with naïve CD45.1⁺ splenic P14-Tcf7-GFP (5×10^5) or OT1-Tcf7-GFP (1×10^5) cells and then inoculated with B16.Gp/B16.OVA tumor cells the next day. 15 days later, CD45.1⁺CD44⁺CD8⁺GFP⁺PD1^{lo} TdLN-T_{TSM} and CD45.1⁺ CD44⁺ CD8⁺ GFP⁺ PD1^{int} TdLN-T_{PEX} cells were sorted from the TdLNs of tumor-bearing mice. TME-T_{PEX} and TME-T_{EX} P14/OT1 cells were sorted as CD45.1⁺CD44⁺GFP(TCF1)⁺ PD1⁺Tim3⁻ and CD45.1⁺CD44⁺ GFP(TCF1)⁻ PD1⁺Tim3⁺ CD8⁺ T cells, respectively, from tumor.

To assess tumor repressive capacity of CD8⁺ T cells from different compartments, 2×10^5 TdLN-T_{TSM}/TdLN-T_{PEX}/TME-T_{EX} OT1 cells, or 2×10^6 TdLN derived bulk TdLN-T_{TSM} (CD44⁺GFP(TCF1)⁺PD1^{lo}CD8⁺) or TdLN-T_{PEX} (CD44⁺CD8⁺GFP(TCF-1)⁺PD1^{int}) cells were transferred into B16.OVA or B16.Gp tumor-bearing mice respectively.

To evaluate the long-term maintenance and homeostatic proliferation of antigen-specific CD8⁺ T cells, 1×10^5 P14 cells from different origins were mixed at 1:1 ratio and co-transferred into naive B6 mice (2×10^6 P14 cells per mouse). And recipient mice were sacrificed at indicated timepoints to test the frequency and proliferation pattern of each population.

For recall experiments, 2×10^4 P14 cells from different origins were transferred into naive B6 recipients respectively, which were challenged with LCMV-Arm⁺ or Lm-Gp and sacrificed at indicated timepoint to test the re-expansion of each population.

To evaluation the conversion between TdLN-T_{TSM} and TdLN-T_{PEX} cells, these two subsets were sorted from day 15 B16.Gp bearing mice and transferred separately into CD45.2⁺ tumor-bearing mice (2×10^4 /mouse). T_{TSM} or TdLN-T_{PEX} derived P14 progenies in TdLNs of recipient mice were assessed 8 days later. In ICB treatment, TdLN-T_{TSM} and TdLN-T_{PEX} cells (2×10^4 /mouse) were transferred to CD45.2⁺ B16.Gp tumor bearing mice, then anti-PD-L1 or control immunoglobulin were administrated intra-peritoneally at indicate time points. Then, TdLN-T_{TSM}⁻ and TdLN-T_{PEX}⁻ derived P14 cells in the TdLNs and TME were analyzed on Day 10 post cell transfer.

In vivo antibody treatment

For immune-checkpoint blockade experiments, mice were intraperitoneally (i.p.) treated with 150 or 300 (Figure S7E) μ g of anti-PD-L1 (10F.9G2, BioXCell), 150 μ g of anti-CTLA4 (9H10, BioXCell) or control immunoglobulin (BioXCell, Rat IgG2b) at indicate time points. For intratumoral or intranodal administration of immune-checkpoint blockade, mice received 25 μ g of anti-CTLA4 or anti-PD-L1 mAb administration in 20 μ l of Pluronic F127 hydrogel (mixed thoroughly, working concentration: 20-25% (w/v)) (Francis et al., 2020).

Listeria monocytogenes (Lm) protection assay

For this part, Cd8^{-/-} recipient mice were intravenously infected with 1×10^5 CFU (colony-forming unit) Lm-Gp one day post adoptive cell transfer. At Day 5 post infection, mice were sacrificed for calculating bacteria loads in tissues. Spleen and liver of infected mice were smashed in 1 ml BHI media with 70 μ m cell strainer and 10-20 μ l of the cell suspension were taken out for serial dilution in 96-wells round bottom plate. 1:10², 1:10³, 1:10⁴, 1:10⁵, 1:10⁶, 1:10⁷ and 1:10⁸ dilution of the infected organ BHI media were made and plated on the BHI agarose (2%) plates. Colonies are counted after 12-16 hours incubation of the plates in a 37°C incubator.

Mice lymphadenectomy and tumor transplantation

Before surgical operations, mice were anesthetized with 8 mg/ml avertin (500 μ l /mouse) to full muscle relaxation. For lymphadenectomy, the anesthetized mice were placed onto the sterilized surgery table and apply the drying preventive ointment on mouse eyes. Skin on lateral flanks was shaved and disinfected with alcohol prep pads. Small incisions were made on lateral flanks and both sides of inguinal lymph nodes were carefully removed. Then sew up the incision and disinfect skin around the cut with povidone-iodine swabs.

Tumor transplantation was conducted as we previously reported (Wang et al., 2021). In brief, B16.Gp cells were inoculated into one side of the inguinal angel of B6 mice, and then P14 cells expressing different congenic markers (CD45.1⁺CD45.2⁺, CD45.1⁺CD45.2⁻ or CD45.1⁻CD45.2⁺) were transferred into tumor-bearing mice respectively. After 8 days (or 14 days, as indicated in related Figures), tumor (hereafter referred as donor) was surgically dissected from P14 cells transferred mice (an average of 5 mm³ in size) and transplanted into tumor-matched recipients (with P14 in different congenic marker transferred) subcutaneously at the same flank of tumor inoculation. Then, P14 cells from donor and recipient were analyzed at indicated timepoints. In Figure 7C, we sorted (CD45.1⁺CD45.2⁺) TdLN-T_{TSM} P14 cells and TdLN-T_{PEX} P14 cells from day 12 B16.Gp tumor bearing mice, and transferred them with equal number to D8 B16.Gp tumor bearing recipients, respectively; subsequently, tumor mass from another D14 B16.Gp tumor bearing mice with P14 cells (CD45.1⁺CD45.2⁻) adoptive transfer prior to tumor cell inoculation were transplanted to above mentioned recipient mice receiving either (CD45.1⁺CD45.2⁺) TdLN-T_{TSM} cells or TdLN-T_{PEX} P14 cells; 2 days after tumor mass transplantation, recipient mice were treated with anti-PD-L1 antibodies and ratios of TdLN-T_{TSM} or TdLN-T_{PEX} derived P14 cells to donor derived P14 cells in TME were determined.

Preparation of single cell suspensions from mouse samples

Splenocytes, lymph node cells, PBMC and TME cell (tumor microenvironment infiltrating lymphocytes) isolation were acquired as previously described (Li et al., 2020). In brief, tumors were excised, manually dissociated. For MC38 model, tumor mass (or liver) was enzymatically digested with 1 mg/mL collagenase I and 0.02 mg/ml DNase I at 37°C. For K/P LUAD model, lung was first cut into tiny pieces with scissors and then enzymatically digested with 150 u/mL collagenase II (supplemented with 1mM

MgCl₂ +1mM CaCl₂) and 0.02 mg/ml DNase I at 37°C. Digested tumors were then mashed through 70µm filters. Hematopoietic cells and lung lymphocytes were further purified using a discontinuous Percoll gradient (GE Healthcare). Cells at the interface were harvested and washed twice before further use. Suspensions of spleen and lymph node cells were obtained by mashing the spleen or lymph nodes through a 70µm nylon cell strainer (BD Falcon).

Cytokine detection, antibodies, dyes, flow cytometry and cell sorting

The antibodies and reagents used for flow cytometry staining are listed in [key resources table](#). Surface staining was performed in PBS containing 2% BSA or FBS (w/v). For the detection of cytokine production and CCL5, lymphocytes were stimulated for 5 h in the presence of the indicated peptide (0.2 µg/ml of GP₃₃₋₄₁ or GP₂₇₆₋₂₈₄, 0.4 µg/ml of KSPWFTIL), Golgi Plug, Golgi Stop, anti-CD107a and anti-CD107b antibodies (BD Biosciences). In B16.Gp, B16.OVA or OVA-expressing autochthonous tumor model (K/P), H-2D^bGP₃₃₋₄₁ tetramer or H-2K^b OVA-tetramer (SIINFEKL) were respectively used to detecting antigen-specific CD8⁺ T cells. Intracellular cytokine staining (ICS) for CD107a/b, IL-2, IFN-γ, TNF-α, granzyme B, CCL5, Bcl2 and Ki67 were performed with the Cytofix/Cytoperm Fixation/Permeabilization Kit (554714, BD Biosciences). Staining of Bcl2, TCF-1, T-bet, Eomes and TOX was performed with the Foxp3/Transcription Factor Staining Buffer Set (00-5523; eBioscience). Annexin V staining were performed with Annexin V Kit (88-8102-72; eBioscience) according to the manufacturer's instructions. CellTrace Violet (C34557; Thermo Fisher) was stained according to the manufacturer's instructions. To effectively block PD-1signaling *in vitro*, P14 cells were cultured in the presence of anti-PD-1(10 µg/ml), IL-2 (20 U/ml), anti-CD3 (2 µg/ml, 100302; Biolegend) and anti-CD28 (0.5 µg/ml, 102102; Biolegend) for 72 hours in a 37°C incubator (5% CO₂). When necessary, cells were sorted on a BD FACSAria III (BD Biosciences) to obtain greater than 95% purity. In BrdU incorporation assay, mice were injected with a BrdU working solution at a dosage of 1.5 mg per mouse via intraperitoneal route daily prior to tissue harvest and analysis as previously reported ([Paley et al., 2012](#)). For experiment design shown in [Figure S7E](#), mice received only one dose of 3 mg BrdU. BrdU incorporation was assessed by the BrdU Flow Kit according to manufacturer's instructions (BD Biosciences). Flow-cytometry data were acquired by FACSCanto II (BD Biosciences) and analyzed using FlowJo (Tree Star).

TCR validation and ELISpot assay

To validate the specificity of TCR clones to tumor antigens, paired α and β chains were annotated based on single-cell TCR sequencing data, and TCR sequences were selected from TdLN-derived top 6 expanded clones in Cluster 1 (see in [Figure 5A; Table S2](#)). Construction of the TCRs was done by fusing the V-D-J of the Vβ regions to the mouse TCRβ constant chain, and the TCRα V-J regions to the mouse TCRα constant chains as previously reported ([Draper et al., 2015; Jin et al., 2018](#)). The chains were separated by a furin-P2A linker ([Table S3](#)). The chains were then synthesized and sub-cloned into the pHR_PGK lentiviral vector (Addgene).

Autologous PBMCs were plated at 1 × 10⁶ cells/ml in 24-well plates in ImmunoCultTM-XF T Cell Expansion Medium (Stemcell Catalog #10981) supplemented with 20 ng/ul of HumanRecombinant IL-2 (Proleukin). T cells were activated with ImmunoCultTM Human CD3/CD28 T Cell Activator (Stemcell #10991) at a concentrate of 25 µL/mL. After 3 days of incubation at 37 °C and 5% CO₂, CD3/CD28 T Cell Activator were removed through centrifugation and activated T cells were resuspend at cell density of 1 × 10⁶ cells/mL by adding fresh complete ImmunoCultTM-XF T Cell Expansion Medium (containing 20ng/ml of IL-2).

For the generation of lentiviral supernatants, pHR_PGK encoding the TCRs (5 µg/well), the envelope-encoding plasmid pMD2.G (3 µg/well) and helper plasmid psPAX2 (5 µg/well) were co-transfected using Lipofectamine 3000 (Life Technologies) into the lentiviral packaging cell line HEK293T (1 × 10⁶ cells per well of 10 cm poly-D-lysine-coated dishes, plated the day prior to transfection in the absence of antibiotics). Lentiviral supernatants were collected and concentrated at 48 hours after transfection as previously reported ([Kim et al., 2014](#)).

For the transfection of TCRαβ pairs into T cells, the Lentivirus transduction system was used. Briefly, activated PBMC cells were seeded in 24-well plate with 1×10⁶ cells/well and 'spin-infected' for 90 min at 37 °C by centrifugation (1000g) with lentivirus supernatants, together with 8 g/ml polybrene (H9268; Sigma-Aldrich). Transduced cells were further cultured for 3 days (37 °C and 5% CO₂) and GFP⁺ CD8 T cells (representing TCR ectopically expressed CD8 T cells) were sorted through FACS for further examination.

For the validation of antigen specificity, ELISpot assay was performed. Briefly, 2 × 10⁴ TCR-transduced T cells were first serially diluted (3 fold); then co-cultured with poly(I:C)-treated autologous tumor cells were (at a ratio of 2:1) in pre-coated 96-well IFN-γ ELISpot plates (Mabtech). After 20h of incubation, cells were harvested from ELISpot plates to assess 4-1BB expression, and plates were developed according to the manufacturer's instructions and counted with a ChampSpot EliSpot Analysis System.

3' single-cell RNA-seq library preparation for mouse T cells

The following mouse T cells were sorted for single-cell RNA-seq: live/dead-CD8⁺CD44⁺GFP⁺CD45.1⁺ P14 cells from spleens of Day 200 LCMV Arm-infected mice; live/dead-CD8⁺CD44⁺CD45.1⁺ P14 cells from dLNs and PBMC of B16.Gp tumor-bearing mice on Day 16 post P14 cell transfer. TME-derived live/dead-CD8⁺CD44⁺PD1⁺CD45.1⁺ P14 cells (Day 16 post P14 cell transfer) were also included (GEO: GSE152628). The scRNA-seq libraries were generated using Chromium Single Cell 3' Library & Gel Bead Kit v.2 (10x Genomics) according to the manufacturer's protocol. Briefly, 1–1.5 × 10⁴ FACS-sorted live cells were used to generate single-cell gel-beads in emulsion for a target recovery of 6,000 single cells. After reverse transcription, gel-beads in emulsion were disrupted. Barcoded complementary DNA was isolated and amplified by PCR (12 cycles). Following fragmentation, end repair and

A-tailing, sample indexes were added during index PCR (8 cycles). The purified libraries were sequenced on a NovaSeq 6000 (Illumina) with 26 cycles of read 1, 8 cycles of i7 index and 98 cycles of read 2. Total RNA extraction and quantitative real-time PCR assay are conducted as previously reported (Wang et al., 2019).

ATAC-seq library preparation

The following cells were sorted for ATAC-seq: live/dead⁻CD8⁺CD44⁺GFP⁺CD45.1⁺ P14 cells from TdLN at Day 4, 8 and Day 21 B16.Gp tumors, TdLN-T_{TSM} (CD45.1⁺CD44⁺GFP⁺PD1^{lo}) and TdLN-T_{PEX} (CD45.1⁺CD44⁺GFP⁺PD1^{int}) P14 cells from TdLN of Day 23 B16.Gp tumor bearing mice with P14 transferred one day prior to tumor inoculation. The ATAC-Seq libraries were prepared as previously described (Chen et al., 2019). Briefly, 50,000 target cells were washed with PBS and then treated with lysis buffer, followed by labeling with the Nextera enzyme (15027865; Illumina). The labeled samples were immediately amplified by 9–10 cycles of polymerase chain reaction (PCR) with barcoded primers and sequenced with a NovaSeq 6000 instrument in a 150 bp/150 bp paired-end run or a NextSeq500 instrument in a 76 bp/76 bp paired-end run.

Single cell dissociation from fresh human biopsies

Single-cell suspensions from collected biopsies were obtained using a modified version of a previously published protocol (Woo et al., 2001). Briefly, the fresh biopsies were processed by sterile mechanical dissection and stirred 1–2 hours at 37 °C shaker (50 rpm) in an enzymatic bath containing RPMI-1640 supplemented with penicillin/streptomycin (50 IU/ml–50 mg/ml; Mediatech), collagenase type I (1 mg/ml; Sigma Chemical Co., St. Louis, MO), DNase type IV (30 units/ml; Sigma Chemical Co.), and hyaluronidase type V (0.01% (v/v); Sigma Chemical Co.). Digested tissues were filtered through 70 µm strainer to achieve single cell suspension, which was proceeded to 44%–67% discontinuous Percoll gradient (GE Healthcare) centrifuge to enrich lymphocytes at the interface. Lymphocytes were harvested and washed twice in PBS-2% FBS (v/v) before frozen in FBS supplemented with 10% DMSO (Sigma) (v/v) at -80 °C for overnight and then in liquid nitrogen until further usage.

Isolation of tumor reactive CD8⁺ T cells from the TME and TdLN

To isolate the tumor specific CD8⁺ T cells, the single cell lymphocyte suspensions from the tumors and tumor draining lymph nodes of the five patients were thawed and cultured for 3 hours at 37 °C in RPMI-1640 medium supplemented with 10% human serum (human AB serum, Gemini Bioproducts). The lymphocyte cells were then stained in PBS-0.5% BSA (w/v) with live/dead (L/D)-APC/CY7, CD45RA-PB, PD1-PE, CD8-PE-CY7, CCR7-PERCP and CD39-FITC (for tumor cells) before subjected to FACS. Due to the limitation of cell numbers obtained from tumor tissues and the low level of live cell ratio, tumor and lymph node lymphocyte cells from two and three patients were mixed, respectively, for cell sorting. L/D⁻CD45RA⁻CCR7⁺PD-1^{dim}CD8⁺ T cells from TdLN and L/D⁻CD45RA⁻CD39⁺PD1⁺CD8⁺ T cells from tumor (TME) were collected, respectively, in RPMI-1640 medium supplemented with 10% human BSA in 15 mL tubes. According to the sorter records, ~7,500 to 6.3 × 10⁵ cells were collected from TdLN and ~3,600 to 5.8 × 10⁵ were enriched from tumor samples. The information of the patients was listed in Table S1.

5' single cell RNA-seq and immune profiling with patient cells

The 5' single cell RNA-seq and immune profiling libraries were generated using Chromium Single Cell 5' Library & Gel Bead Kit v. 1 or v. 2 (10x Genomics) according to the manufacturer's protocol. Briefly, after the above-mentioned patient CD8⁺ cells were sorted into RPMI-1640 medium in 15 mL tubes, the tubes were centrifuged with flying rotor at 450 g at room temperature (RT) for 8 min. The supernatant was carefully removed with pipette and ~30 µL residue media with cells were left undisturbed in the tube bottom. Then, the cells in the residue were gently and thoroughly mixed and were kept on ice until ready for single-cell library construction. Cells from the four samples (\leq 16,500 cells per sample) were loaded separately into 10x Chromium Next GEM Chip K to prepare single cell emulsion according to the manufacturer's instructions. The reverse transcription and cDNA amplification were performed according to the manufacturer's manual. Size distribution and DNA concentration of amplified cDNA were measured with Qsep (BiOptic) and Qubit HS dsDNA kit (Thermofisher), respectively. Aliquots of cDNA from each sample were proceeded to construction of expression libraries and TCR libraries according to the manufacturer's manual. All libraries were sequenced with Illumina Novaseq under the 2 × 150 bp model, obtaining ~58,000 reads/cell and ~24,000 reads/cell for each expression library and TCR library, respectively.

QUANTIFICATION AND STATISTICAL ANALYSIS

Pre-processing of single cell RNA-seq data

Raw 3' and 5' single-cell RNA data from this project and published datasets (listed in key resources table) were processed using 10X Genomics Cell Ranger Suite (v3.1.0), including aligning the demultiplexed FASTQ reads to the reference genome (mm10, v3.0.0 for mouse data; GRCh38 for patient data, from 10X Genomics) and counting the unique molecular identifier (UMI) for each cell barcode by using the 'cellranger count' function. For each sample, data sets from individual libraries were aggregated using the 'cellranger aggr' function of Cell Ranger Suite without sequencing depth normalization. Accordingly, a gene expression matrix for digital cells was generated, containing the number of UMI for each gene detected in each cell. The raw gene expression matrix was filtered using the following criteria. First, we removed cells with over 20% of mitochondrial gene expression in UMI counts because dead and

damaged cells often exhibit extensive mitochondrial contamination (Ilicic et al., 2016). Second, we removed cells for which less than 200 genes were detected. The number of retained cells for each sample was summarized in Figure S2A. In the end, we obtained a total of 28,958 mouse and 40,847 patient, respectively, single cells for further analysis.

Dimension reduction and unsupervised clustering

The processed gene expression matrix with all retained cells for each sample was imported to the Seurat R package (v3.2.3) for downstream analyses (Stuart et al., 2019). The mitochondrial genes were ruled out from the gene expression matrix in each sample, and then the matrix was normalized using the ‘NormalizeData’ function, in which UMI counts for each gene were divided by the total UMI counts in each cell and multiplied by the scale factor of 1000, following by natural-log transformation with adding a pseudo count of 1 for each gene. Based on the normalized expression matrix, 2,000 most variable genes were identified for each sample using the ‘FindVariableFeatures’ function with the ‘vst’ method. To avoid the dominant effect of Ribosomal protein-coding genes, which usually show very abundant expression levels in subpopulation of cells, those Ribosomal protein coding genes were removed from the list of the variable genes. The remained variable genes from each sample were combined to obtain a unique list for the high variable genes (7,071) in the set of gene expression matrixes. The unique list for the high variable genes was applied for the next principal component analysis (PCA). Before PCA, the gene expression matrixes from each sample were merged into a whole gene expression matrix for all cells, and the ‘ScaleData’ function was then used to scale and center the gene expression matrix after regressing out the heterogeneity associated with the mitochondrial contamination. PCA was performed on the selected variable genes to identify the top 50 principal components using the ‘RunPCA’ function of Seurat. Substantial variability between cells has been obtained from different samples, reflecting a combination of technical and biological variations. These batch effects in some cases may lead to cluster cells first by sample heterogeneity, rather than cell types or cell states. To eliminate the batch effects, we used the Harmony (v1.0) (Korsunsky et al., 2019) to integrate seven datasets into a shared space for unsupervised clustering. Briefly, we fed the calculated PCA matrix into the ‘RunHarmony’ function implemented in Seurat. As the Harmony algorithm can integrate categorical covariates, we set sample and 10X library construction protocol (Chromium Single Cell 3’ Reagent Kit v2 and v3) as two covariates for batch effect correction. For those two covariates, the corresponding theta parameters were set as 2 and 1.2, respectively. The batch-effect-corrected Harmony embeddings were then applied to dimension reduction using the ‘RunUMAP’ function in Seurat. After the Harmony integration, Uniform Manifold Approximation and Projection (UMAP) (Becht et al., 2018) visualization indicated cells from different samples were well mixed into the shared space. To perform the clustering analysis, we applied Harmony reduction as input for building the Shared Nearest Neighbor (SNN) graph using Principal components (PCs) 1 to 50 and $k=25$ nearest neighbors, and then the Louvain clustering algorithm was used to group the cells into different clusters. These parameters were chosen for SNN graph construction to ensure cells from distinct compartments were not grouped.

Identification of differentially expressed genes

Differentially expressed genes in different clusters were identified by the ‘FindAllMarkers’ function in Seurat using the ‘MAST’ test and setting min.pct=0.25. MAST algorithm fits a hurdle model to the expression of each gene, consisting of logistic regression for the zero values (the undetectable expression level) and linear regression for the non-zero values (the expression level) (Finak et al., 2015). The cell subset representing cell cycle states (cluster 7 in Figure 3A) was excluded for identifying differentially expressed genes. The UMAP was applied to visualize the transcriptional profiles of the differentially expressed genes in 2D space based on the SNN graph described above (Figures 3E and S2D). Other dot plots and heatmaps for the differentially expressed genes were generated by customized R code using ggplot2 (v3.3.3, R package).

Annotation of cell clusters

We applied two complementary methods to annotate the characteristics of different cell clusters in Figure 3A. We first checked whether the well-characterized marker genes of different T cells were in the top rank of differentially expressed genes of query clusters and then assigned the most likely identity to the query cluster. If the query cluster without the support of signature genes, we then applied the SingleR (Aran et al., 2019), which leverages reference transcriptomic datasets of known cell types for annotation, to determine whether the predicted annotation for a query cluster based on different reference datasets were consistent, and then assigned that query cluster as the predicted cell-type annotation. Alternatively, we annotated a query cluster with genes in the top rank of differentially expressed gene list of the query cluster.

Re-clustering of TdLN-CD8⁺ T cells and memory CD8⁺ T cells

Antigen specific TdLN-CD8⁺ T cells were largely grouped into two subsets, T_{MEM} 1 (*Ilr7⁺Sel7⁺*) and T_{MEM} 2 (*Tcf7⁺Cd69⁺*) clusters, during the unsupervised clustering as described above. To systematically characterize the transcriptional differences between TdLN CD8⁺ T cells and memory CD8⁺ T cells, we extracted the annotated T_{MEM} 1 (*Ilr7⁺Sel7⁺*) and T_{MEM} 2 (*Tcf7⁺Cd69⁺*) subsets from TdLN and Arm-D200 (memory T cells) datasets for re-clustering analysis. The selected subpopulations of cells then were applied with the pipeline as described above for re-clustering, with the modification that the SNN graph defined using PCs 1 to 30 and $k=50$ nearest neighbors. These parameters allowed to yield relatively fewer subclusters, enabling the detection of the major differences between the two subclusters (Figure 3F). We then searched for differentially expressed genes that could accurately distinguish between cells in each subcluster versus all other cells using ‘FindAllMarkers’ function in Seurat with parameters described

above. Sub-clusters containing significantly discriminative marker genes were flagged for further analyses (Figure S2H). We found that over 160 genes were differentially expressed between Subclusters 1 and 2 (Figures S2H and S2I). Because well-studied marker genes are inadequate to characterize the sub-clusters, we used the top discriminative marker genes to annotate the identity of the sub-clusters (Figures 3H and S2K–S2O).

Identifying cells with active gene sets

In order to evaluate whether a hallmark or critical gene set was enriched within the expressed genes for each cell, we calculated a gene set activity score for each gene set using an Area Under the Curve (AUC) method named AUCell (v1.7.2, R package) (Aibar et al., 2017). A collection of annotated gene sets was downloaded from the MSigDB database (v7.1). For each query gene set, we built the AUC of recovery curve for each cell based on the ranking of the top 5,000 genes in every single cell. In the recovery curve, the x-axis represents the ranking of expressed genes from high to low based on their expression values, and the y-axis is the number of genes recovered from the query gene set. We used the ‘AUCell_calcAUC’ function to calculate an AUC score for each query gene set in each cell. Each cell can be colored based on their AUC scores with UMAP embedding for visualization. The distribution of AUC scores across all cells allows exploring the relative expression of signatures in cell subpopulations (Figures S2E and S2J).

T cell receptor data analysis

Raw CD8⁺ T cell receptor (TCR) sequencing data were processed using the ‘multi’ function in the 10X Genomics Cell Ranger Suite (v5.0.0). The sequencing reads from each TCR sequencing library were aligned to human GRCh38 V(D)J reference genome (v5.0.0, from 10X Genomics), resulting in the assembly of V(D)J sequences and CD8⁺ clonotypes. On average, approximately 24,000 read pairs were obtained for each cell in the 12 TCR sequencing libraries (6 from TdLN and the other 6 from TME). We used the default settings in the ‘multi’ function to discard cells with low-confidence or non-detectable TCR contigs. The assembled TCR contigs from all TCR libraries were combined to identify clonal TCRs and clonal CD8⁺ T cells shared between TdLN and TME. For cells with two or more TRA (TCR α) or TRB (TCR β) chains assembled, the TRA–TRB pair showing the highest UMI count was defined as the dominant TRA–TRB pair in the corresponding cell. If two or more cells had identical dominant TRA–TRB pairs, the dominant TRA–TRB pair were identified as clonal TCRs, and these T cells were identified as clonal CD8⁺ T cells. In order to characterize the cell states of clonal CD8⁺ T cells shared between TdLN and TME, we required the clonal CD8⁺ T cells to be detected at least twice in TIL. According to the criteria described above, we recovered 1165 and 2211 clonal CD8⁺ T cells from TdLN and TME, respectively, representing 209 clonal TCRs (Figure 5A). The detailed TRA and TRB sequences and clone counts are shown in Table S2. Those recovered clonal CD8⁺ T cells were integrated with their matched scRNA-seq data to perform the unsupervised clustering and identify differentially expressed genes as previously described.

Reconstruction of TCR sequences from scRNA-seq data

We used TraCeR to reconstruct human TCR sequences from scRNA-seq data with minor modification (Stubbington et al., 2016). The V gene in each TCR sequence was identified by V-QUEST tool in IMGT database (Brochet et al., 2008). The human TCR constant regions were exchanged for mouse TCR constant regions to reduce mispairing with endogenous TCR chains as previously reported (Cohen et al., 2006; Jin et al., 2018; Xiong et al., 2020).

Building single-cell trajectory

We constructed cell trajectories with Monocle 3 using scRNA-seq data (Cao et al., 2019). The dimensionality of the scRNA-seq data was reduced by PCA with 50 components and UMAP was applied to visualize the result of data dimensionality reduction. We chose the cell derived from TdLN and with the highest expression level of *TCF7* as the ‘root’ of the trajectory. Monocle 3 ordered each cell along a learned trajectory according to its transcriptional progress. The default parameters in Monocle 3 were used for the analysis.

Analysis pipeline of bulk ATAC-seq data

Bulk ATAC-seq sequencing reads downloaded from the Sequence Read Archive from the study of Jadhav et al. (Jadhav et al., 2019) (GEO: PRJNA546023) were aligned to the mouse reference genome (mm10) using ‘mem’ function in bwa (v0.7.15) (Li and Durbin, 2009). Mapped reads were filtered for mapping quality (-q 20), and duplicates were removed using the MarkDuplicates tool in Picard (v1.107). Reads aligned to scaffolds and chrM or chrY were excluded for downstream analyses. Biological replicates were combined to call peaks using MACS2 (Zhang et al., 2008) with parameters –call-summits –nomodel –shift -100 –extsize 200 –keep-dup all. Resulting peaks from different cell types were pooled, and overlapping peaks were merged using the ‘merge’ function in bedtools (v2.25.0) (Quinlan and Hall, 2010). This approach yielded a total of 59,992 merged peaks in the analyses relative to Figure S3. We then counted sequencing reads in each merged peak from each dataset to generate a count matrix and the matrix was applied for PCA analysis in Figure S3A. In order to profile the state-specific epigenetic landscape of TdLN CD8⁺ T cells in Figure S3, we applied DEseq2 (v1.30.1) to identify differential chromatin accessibility regions between TdLN CD8⁺ T cells and other types of CD8⁺ T cells, including stem-like exhausted CD8⁺ T cells, terminal exhausted CD8⁺ T cells, terminal effector CD8⁺ T cells, memory CD8⁺ T cells and memory precursor CD8⁺ T cells. Totally, we identified 6,316 chromatin accessibility regions showing significant differences ($|\log_2(\text{FC})| > 2.5$, FDR < 0.01) between TdLN CD8⁺ T cells and other CD8⁺ T cells. Read counts were generated for each differential chromatin accessibility region, normalized with DEseq2 (v1.0.3, R package) (Love et al., 2014), and clustered into six distinct

groups using the Self-Organizing Map algorithm (SOM, v0.3, R package) (Chaudhary et al., 2014). Differential chromatin accessibility regions were centered by their summits with 2 kb extension at both sides to visualize the enrichment of ATAC-seq signals in details (Figure S3B).

To characterize the epigenetic landscape of TdLN-T_{TSM}, TdLN-T_{PEX}, and CI13-T_{PEX}, bulk ATAC-seq data from the three samples were analyzed similar as above. We obtained 44,484 merged peaks for the PCA analysis in Figure S4C and 12,746 significantly differential chromatin accessible regions ($|\log_2(\text{FC})| > 1$, FDR < 0.01) between each two samples.

Gene ontology enrichment analysis

Many ATAC-seq peaks locate at non-coding genomic regions, which are not overlapping with transcription start sites of genes and typically lack functional annotations. GREAT is broadly used to assign biological meaning to a set of non-coding genomic regions by analyzing the annotations of their nearby genes (McLean et al., 2010). We obtained the genomic coordinates of differential chromatin accessibility peaks from each cluster in Figures S3B and S4D, and then performed enrichment for gene ontology terms using the GREAT online tool (<http://great.stanford.edu/public/html/>). The P-value cutoff of 0.01 after multiple hypothesis correction using the Benjamini-Hochberg method was applied to select the significantly enriched gene ontology terms in each cluster in Figures S3B and S4D, respectively (Figures S3C and S4E).

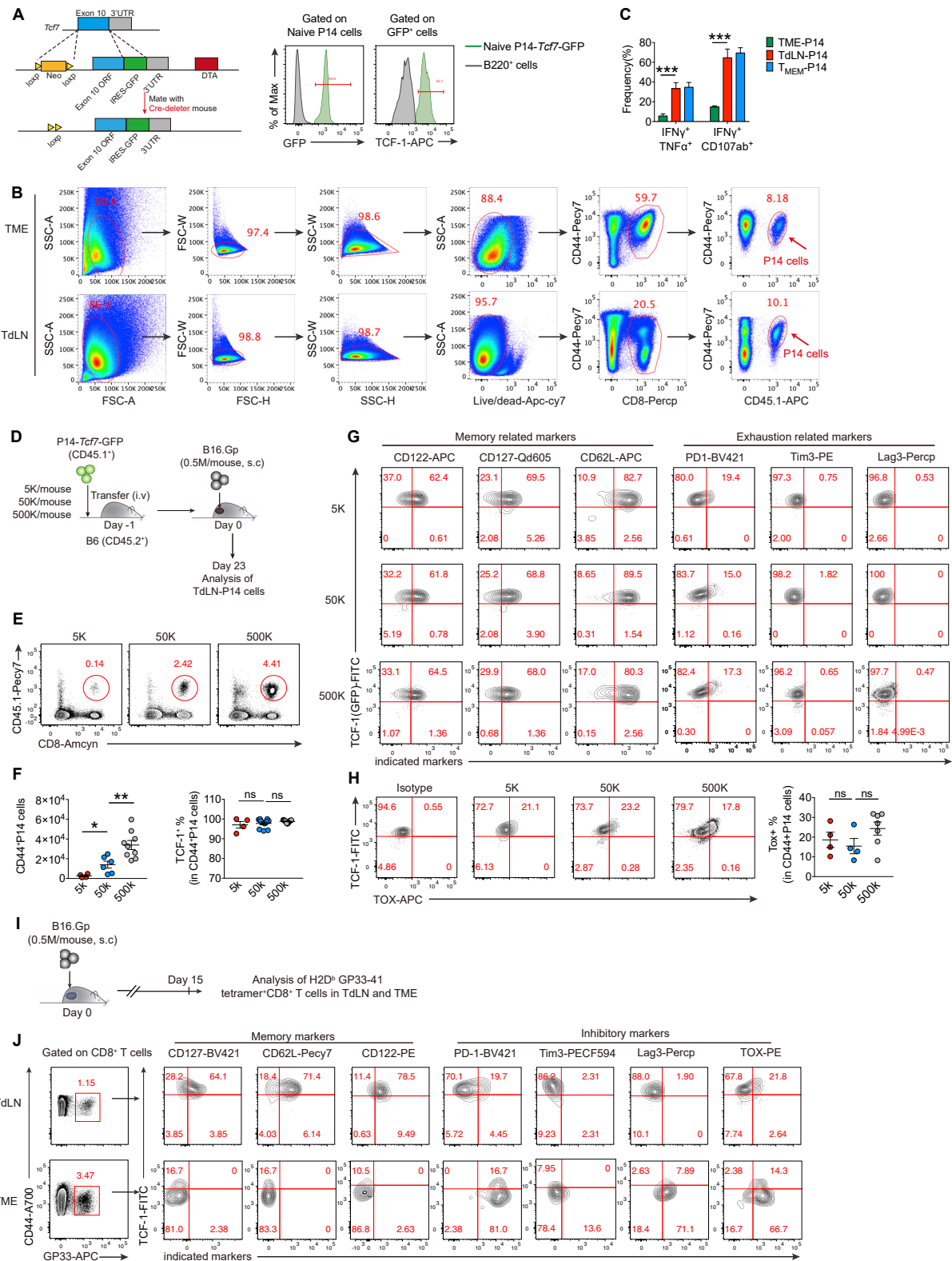
Motif enrichment analysis

Genomic regions surrounding ATAC-seq peaks typically are enriched for binding sites of transcription factors (TFs). We applied the MEME-ChIP tool in MEME Suite (Machanick and Bailey, 2011) to comprehensively determine which TF binding motifs were most centrally enriched at the ATAC-seq peaks from each cluster in Figures S3B and S4D. we extracted 250 bp DNA sequences centered by ATAC-seq peak summits and fed them to MEME-ChIP online tool (<https://meme-suite.org/meme/tools/meme-chip>). The 'JASPAR CORE (2014)' motif database was used for scanning binding motifs of TFs both from human and mouse. The E-value indicating significant enrichment was applied to generate motif enrichment heatmap in Figures S3D and S4F.

Statistical analysis

Statistical analysis was performed with Prism 7.0 (GraphPad) by two-tailed paired Student's t-test, two-tailed unpaired Student's t-test, or one-way ANOVA with Newman-Keuls's test. Two-way ANOVA was performed for comparing tumor growth curves. The log-rank (Mantel-Cox) test was performed for comparing mouse survival curves. n represents the number of mice used in the experiment, with the number of individual experiments listed in the legend. Graphs show individual samples and center values indicate mean. p values < 0.05 were considered significant (*: p < 0.05; **: p < 0.01; ***: p < 0.001); ns: not significant, p-values > 0.05).

Supplemental figures



(legend on next page)

Figure S1. *Tcf7-GFP* knockin reporter mice construction, flow cytometric analyses of TdLN-derived tumor-specific CD8⁺ T cells, related to Figures 1 and 2

(A) Left: schematic strategy showing the construction of *Tcf7-GFP* knockin reporter mice. Right: expression of a *Tcf7-GFP* fusion gene (green) in naive P14 cells (left) or TCF-1 protein staining (green) in GFP⁺ P14 cells (right) as compared with B220⁺ B cells (gray fill).

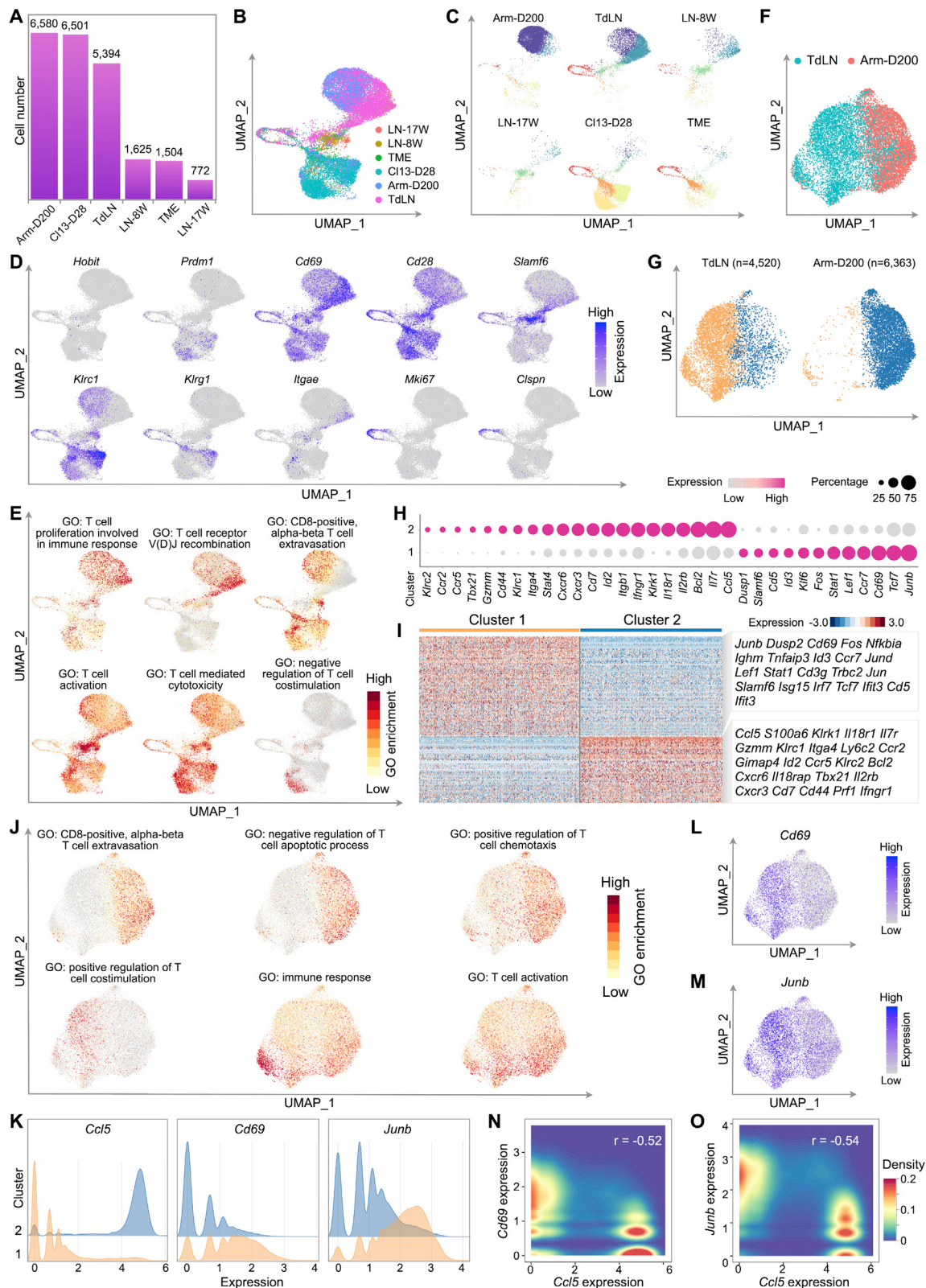
(B) Gating strategy of activated P14 cells in the TME (upper) and TdLNs (down).

(C) Statistical analyses of the frequencies of IFN- γ ⁺TNF- α ⁺ and IFN- γ ⁺CD107a/b⁺ P14 cells in Lm-Gp infected recipients transferred with TME-, TdLN- (15 days post P14 transfer, n = 3), or T_{MEM}-P14 cells (spleen of Arm⁺ infected mice, day 60 post infection, n = 3), following 5 h of stimulation *in vitro* with LCMV GP_{33–41} peptide (seen in STAR Methods).

(D–H) C57BL/6J mice (CD45.2⁺) were transferred with 5 × 10³ (5k), 50k, or 500k naive CD45.1⁺ P14-*Tcf7-GFP* cells. 1 day later, mice were s.c. implanted with B16.Gp tumor cells. P14 cells in the TdLNs were analyzed on day 23 post cell transfer. (D) Experimental design. (E) Representative plots of CD44⁺CD45.1⁺ P14 cells in TdLN of mice received 5k, 50k, or 500k naive CD45.1⁺ P14-*Tcf7-GFP* cells as in (D). (F) Left: statistical analyses of the cell number of CD45.1⁺CD44⁺ P14 cells in TdLN of recipients received either 5k (n = 4), 50k (n = 6), or 500k (n = 9) naive CD45.1⁺ P14-*Tcf7-GFP* cells as in (D). Right: summary of frequencies of TCF1⁺ cells in CD44⁺ P14 cells from TdLN of indicated recipients (n ≥ 4) as in (D). (G) Flow-cytometry analyses of memory markers (CD122, CD127, and CD62L) and inhibitory receptors (PD-1, Tim3, and Lag3) relative to GFP (TCF-1) expression in CD44⁺ P14 cells from the TdLNs of mice received 5k, 50k, or 500 k naive CD45.1⁺ P14-*Tcf7-GFP* cells as in (D). Numbers are frequencies. (H) Left: representative plots of the co-expression pattern of TCF-1 and TOX in CD45.1⁺CD44⁺ P14 cells. Numbers are frequencies. Right: summary of the frequencies of TOX⁺ cells in CD44⁺ P14 cells from TdLNs of indicated recipients (n ≥ 4).

(I and J) Analysis of endogenous tumor-specific CD8⁺ T cells in the TdLNs. Mice were inoculated with B16.Gp tumor cells and sacrificed at day 15 post tumor implantation. Lymphocytes in the TME and TdLNs were harvested and stained with H2D^b GP_{33–41} tetramer for further analyses. (I) Experiment design. (J) Representative plots of GP33-specific CD8⁺CD44⁺ T cells in TdLN and TME by H-2D^b peptide-MHC tetramer staining (left) and the co-expression pattern of TCF-1 and indicated markers in tetramer-specific CD8⁺CD44⁺ T cells as in (A). Numbers are frequencies.

*p < 0.05, **p < 0.01, and ***p < 0.001 versus control, one-way ANOVA analysis (C, F, right panel of H). Data are representative of ≥2 independent experiments (mean ± SEM).



(legend on next page)

Figure S2. Transcriptomic comparisons of TdLN-derived tumor-specific CD8⁺ T cells with antigen-specific memory and exhausted CD8⁺ T cells at single-cell level, related to Figure 3

(A) Histogram showing number of cells in each sample applied for scRNA-seq clustering analysis. TME, tumor microenvironment derived P14 cells from B16.Gp bearing mice; TdLNs, tumor-draining lymph node P14 cells of B16.Gp tumor-bearing mice; LN-8/17W, tumor-draining lymph node Gp33⁺CD44⁺CD8⁺ T cells of LUAD tumor-bearing mice at 8 or 17 weeks post tumor induction; Arm-D200, memory P14 cells at day 200 post LCMV-Arm infection; Cl13-D28, Gp33⁺CD44⁺PD1⁺CD8⁺ T cells at day 28 post LCMV-Cl13 infection, related to [Figures 3A](#) and [3B](#).

(B) UMAP plot of 22,376 antigen-specific CD8⁺ T cells from 6 samples with cells color-coded from different samples, related to the combined UMAP plot in [Figure 3A](#).

(C) The UMAP plot for each sample split from the combined plot in [Figure 3A](#). The number of cells for each sample analyzed in the UMAP projection was indicated in (A). Each dot denotes an individual cell, and colors represent cluster origins. The color coding was shown in [Figure 3A](#).

(D) Single-cell transcription levels of selected genes illustrated in the combined UMAP plot from [Figure 3A](#). Each dot represents an individual cell. Transcription levels are color coded: gray, not expressed; blue, expressed.

(E) UMAP plot showing the enrichment of gene sets within expressed genes for each cell. The gene signatures associated with gene ontology (GO) items were listed on the top of each plot. The enrichment score indicated the relative expression level of gene signatures in individual cells. The enrichment score indicating the relative expression level of gene signatures in individual cells is color coded from not enriched (gray) to highly enriched (red). AUCell algorithm was applied to obtain the enrichment scores of gene signatures (see details in the [STAR Methods](#)).

(F) UMAP plot showing unsupervised clustering of TdLN (B16.Gp model) and Arm-D200 cells selected from clusters 1 to 2 in the combined UMAP plot in [Figure 3A](#). Each cell was colored according to sample origins, related to [Figures 3F–3H](#).

(G) UMAP plots for sample TdLN and Arm-D200 separately. The number of cells in each sample was listed on the top of each plot, related to [Figures 3F–3H](#).

(H) Dot plot showing the relative average expression of a subset of marker genes (x axis) across the clusters (y axis). As indicated on the legend, dot size denotes the percentage of cells in a cluster expressing each gene. Dot color represents the relative average expression levels.

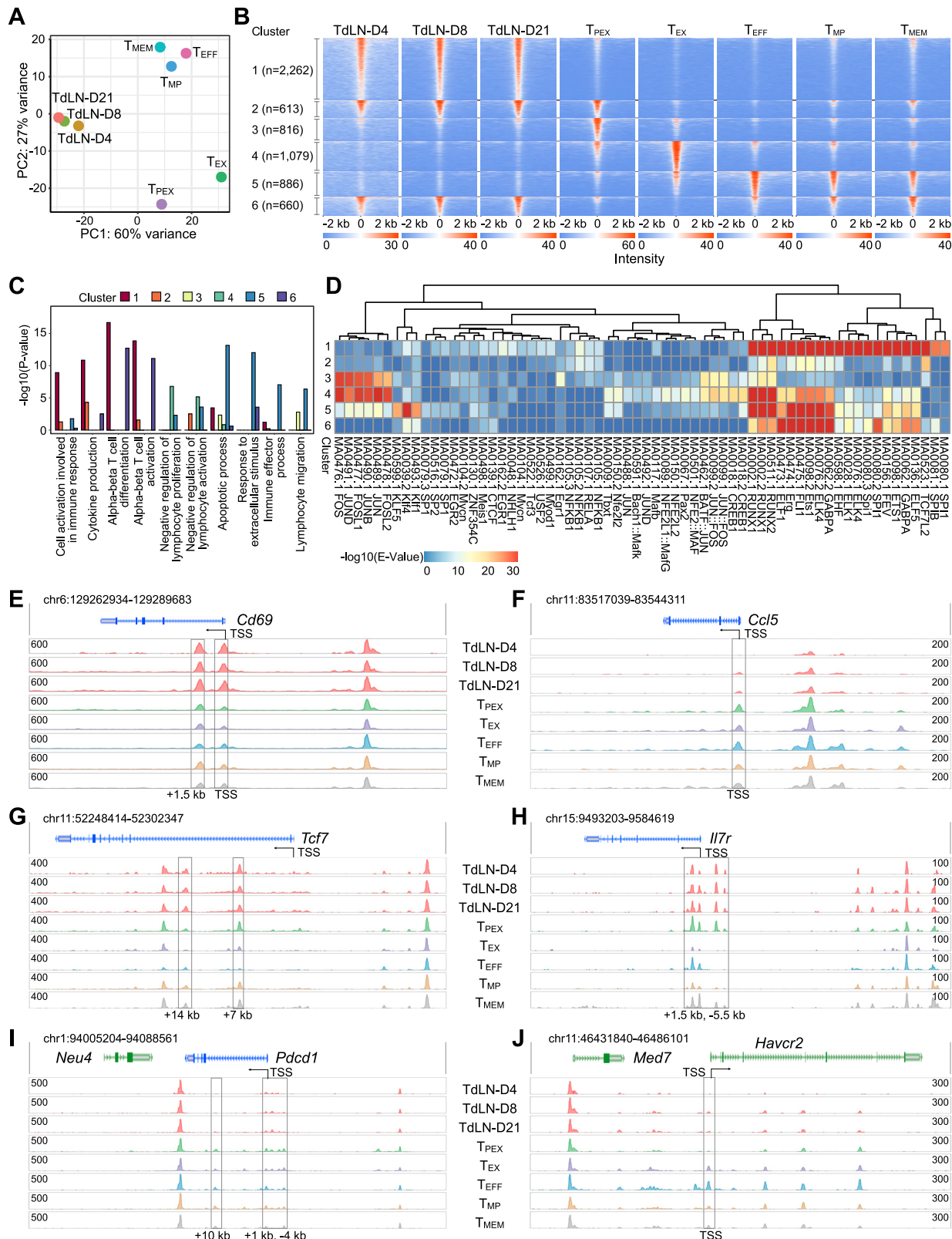
(I) Heatmap showing expression patterns of differentially expressed genes in each cluster defined in [Figure 3F](#). Genes were grouped by clusters, and 500 cells were randomly selected in each cluster for the plot. The relative expression level for each gene was scaled to a Z score distribution from -3 to 3. Representative genes for each cluster were listed on the right side of the heatmap, related to [Figures 3F–3H](#).

(J) UMAP plot showing the enrichment of gene sets within expressed genes for each cell. The enrichment score indicating the relative expression level of gene signatures in individual cells is color coded from not enriched (gray) to highly enriched (red). The gene signatures associated with GO items were listed on the top of each plot. The color scale indicated the enrichment scores from not enriched (gray) to highly enriched (red).

(K) Ridge plots representing relative gene expression levels of marker genes *Ccl5*, *Cd69*, and *Junb* in each cluster, related to [Figure 3H](#).

(L and M) Single-cell transcription level of *Cd69* (L) and *Junb* (M) illustrated in the UMAP plot, as defined in [Figure 3F](#).

(N and O) Contour plot showing co-expression patterns of *Ccl5*-*Cd69* (N) and *Ccl5*-*Junb* (O) in cells applied for the UMAP plot in [Figure 3F](#). *Ccl5* and *Cd69*/*Junb* exhibited a mutually antagonistic expression pattern at the single-cell level with a Pearson correlation coefficient (*r*) of -0.52 (*p* < 0.001) for *Ccl5*-*Cd69* and -0.54 (*p* < 0.001) for *Ccl5*-*Junb*, respectively.



(legend on next page)

Figure S3. Epigenetic landscape of TdLN-derived P14 cells revealed by ATAC-seq, related to Figure 3

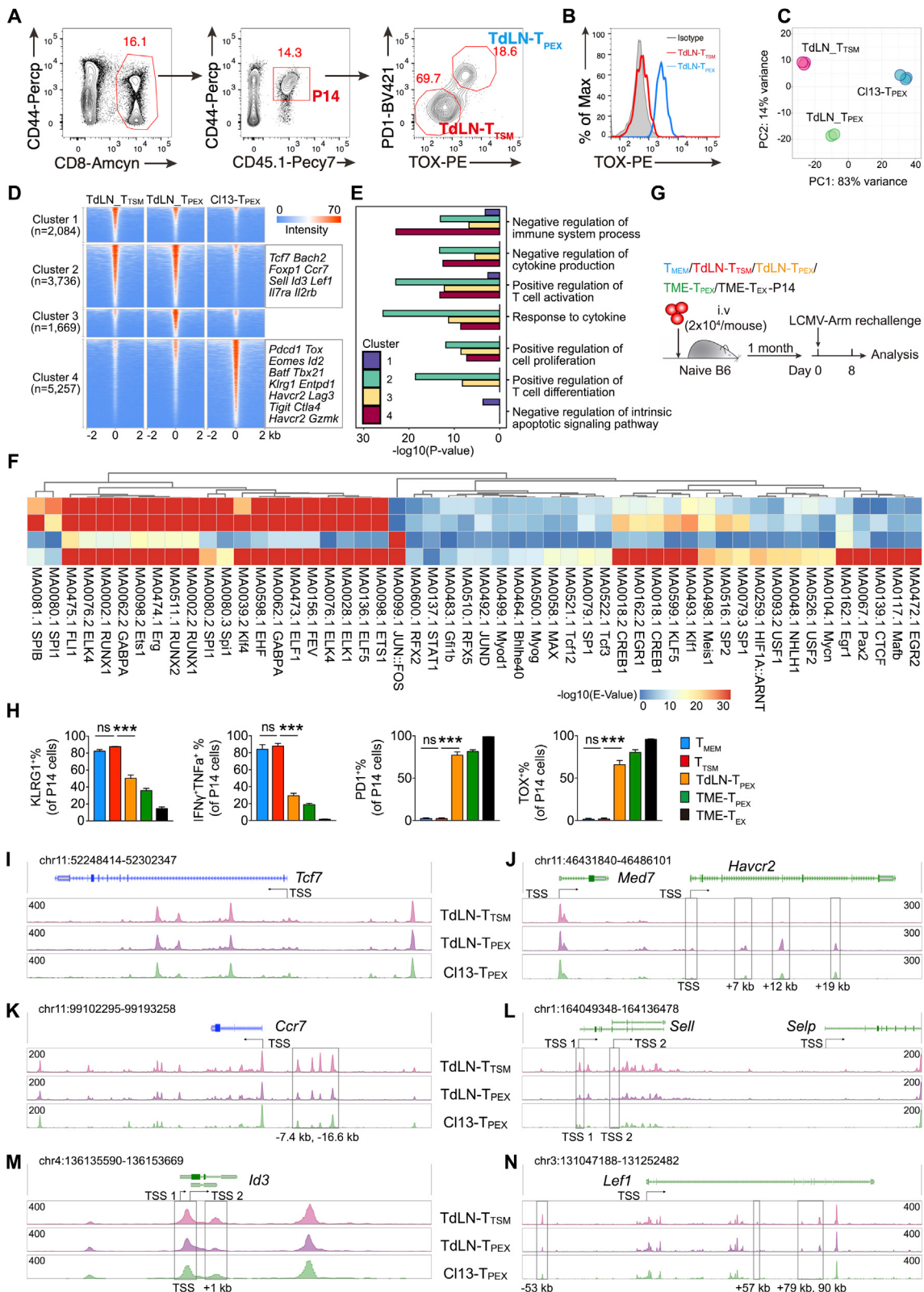
(A) PCA plot of bulk ATAC-seq data. T_{MEM} , memory CD8⁺ T cells; T_{MP} , memory precursor CD8⁺ T cells; T_{EFF} , terminal effector CD8⁺ T cells; T_{PEX} , progenitor exhausted CD8⁺ T cells; T_{EX} , terminal exhausted CD8⁺ T cells.

(B) Heatmap showing the chromatin accessibility scores across ± 2 kb region of the accessible peaks identified by ATAC-seq data. The peak regions are aligned at the center of the peaks and grouped based on K-means clustering of the accessibility scores. The color code represents the ATAC-seq signal coverage. The number of regions within each cluster was denoted in the bracket.

(C) Representative gene ontology (GO) items enriched in the clusters defined in (B).

(D) Enrichment of known motifs of DNA binding proteins in the accessible regions for each cluster defined in (B). The color codes for the enrichment of each motif (see details in [STAR Methods](#)). Each column represents a motif corresponding protein (both human and mouse), with motif ID indicated.

(E–J) ATAC-seq signals in the representative regions showing differentially accessible status across different cell types. Genomic coordinate of each region is indicated at top left of each plot. The transcription starting site (TSS) and transcription direction of interested genes are illustrated with the black arrow. The gray rectangles mark regions with differential accessibility signatures in cell types. A differential accessible region is denoted as “TSS” when overlapping a gene’s TSS; otherwise, the genomic distance to the TSS of the interested gene is marked underneath the rectangle. The maximum score of normalized ATAC-seq intensity is shown on the left/right of each track.



(legend on next page)

Figure S4. TdLN-T_{TSM} exhibited a unique epigenetic program comparing with TdLN-T_{PEX}, related to Figure 4

(A) Representative plots of the co-expression pattern of PD-1 and TOX in TdLN-derived CD45.1⁺CD44⁺CD8⁺ P14 cells. TOX expression was positively correlated with PD-1 expression.

(B) Histogram denoting the expression level of TOX between TdLN-T_{TSM} and TdLN-T_{PEX} cells as in (A).

(C) PCA plot showing the similarity between cell types from genome-wide chromatin states by ATAC-seq profiling. TdLN-T_{TSM}, CD44⁺GFP⁺PD1^{lo}CD8⁺ P14 cells from dLN of B16.GP bearing mice; TdLN-T_{PEX}, CD44⁺GFP⁺PD1^{hi}CD8⁺ P14 cells from dLN of B16.GP-bearing mice; CL13-T_{PEX}, PD-1⁺CXCR5⁺Tim3⁻ P14 cells from CL13 infected mice.

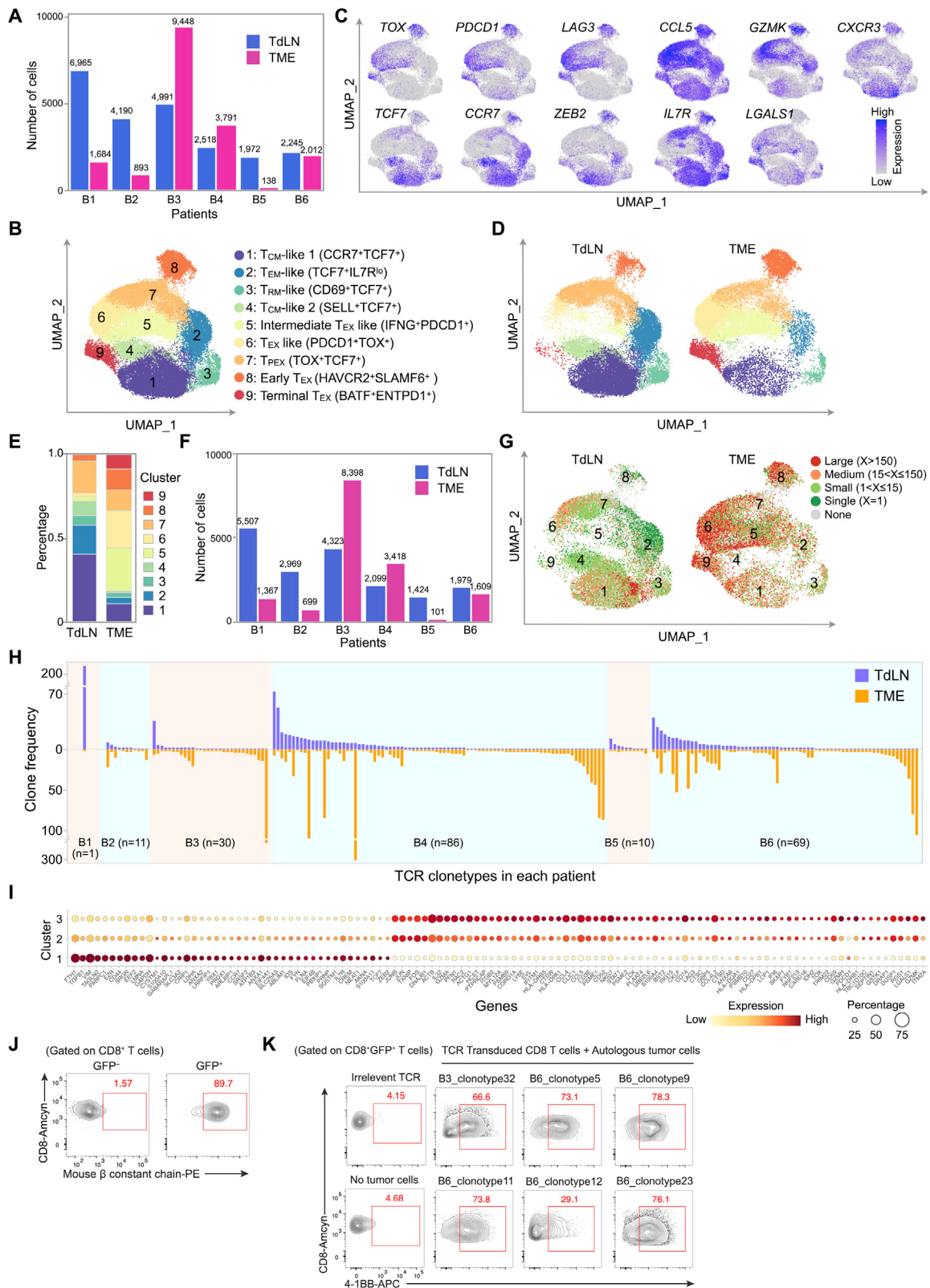
(D) Heatmap showing the chromatin accessibility scores across ± 2 kb region of the accessible peaks identified by ATAC-seq data. The peak regions are aligned at the center of the peaks and grouped based on K-means clustering of the accessibility scores. The color code represents the ATAC-seq signal coverage. The number of regions within each cluster was denoted in the bracket.

(E) Bar plot summarizing the representative GO items enriched in the clusters defined in (D).

(F) Heatmap showing motif enrichments of transcription factors in each cluster defined in (D). The color represents the enrichment scores. The motif IDs in JASPAR database (<https://jaspar.genereg.net/>) are shown at the bottom of the plot.

(G and H) T_{MEM}⁺, TdLN-T_{TSM}⁺, TdLN-T_{PEX}⁺, TME-T_{PEX}⁺, and TME-T_{EX}-P14 cells were sorted and separately transferred to B6 recipient mice (2×10^4 cells/mouse). After resting for 1 month, the recipient mice were rechallenged with LCMV-Arm⁺ (2×10^5 PFU/mouse) infection (G), and the proportions of KLRG1⁺, IFN- γ ⁺ TNF- α ⁺, PD1⁺, and TOX⁺ P14 cells from each group were summarized in (H). n = 5, ***p < 0.001 versus control (one-way ANOVA analysis). Data are representative of ≥ 2 independent experiments (mean \pm SEM).

(I–N) ATAC-seq track views for representative genes in the representative regions showing differentially accessible status across different cell types. Genomic coordinate of each region is indicated on top left of each plot. Genomic coordinate of each region is indicated at top left of each plot. The transcription starting site (TSS) and transcription direction of interested genes are illustrated with the black arrow. The gray rectangles mark regions with differential accessibility signatures in cell types. A differential accessible region is denoted as “TSS” when overlapping a gene’s TSS; otherwise, the genomic distance to the TSS of the interested gene is marked underneath the rectangle. The maximum score of normalized ATAC-seq intensity is shown on the left/right of each track.



(legend on next page)

Figure S5. Identification and characterization of TdLN-derived tumor-reactive memory CD8⁺ T cells in HCC patients, related to Figure 5

(A) Histogram showing numbers of TdLN- and TME-derived putative tumor-reactive CD8⁺ T cells obtained from scRNA-seq experiments for each hepatocellular carcinoma (HCC) patient (B1–B6, [Table S1](#)).

(B) Tumor-reactive CD8⁺ T cells (n = 40,847) from 6 HCC patients projected into UMAP analysis showing nine significant clusters. The number of cells for each sample analyzed in the UMAP projection was indicated in (A). Each dot denotes an individual cell, and each dot color represents an annotated cluster. T_{CM}-like, central memory-like T cells; T_{EM}-like, effector memory-like T cells; T_{RM}-like, tissue resident memory-like T cells; T_{PEX}, progenitor exhausted T cells; T_{EX}, exhausted T cells.

(C) Single-cell transcription levels of representative genes illustrated in the UMAP plot from (B). Transcription levels are color coded: gray, not expressed; blue, expressed.

(D) UMAP plot showing TdLN- and TME-derived tumor-reactive CD8⁺ T cells, separately, related to the UMAP plot in (B).

(E) Bar plot demonstrating percentages of cells in each cluster as a fraction of total cells for each sample position, related to the UMAP plot in (B).

(F) Histogram showing number of cells with identified TCRs from TdLN and TME in each patient sample.

(G) UMAP plot showing TdLN- and TME-derived tumor-reactive CD8⁺ T cells overlaid with frequency of clonotypes, respectively.

(H) Bar plot showing the numbers of TCR clones shared between paired dLN- and TME-derived tumor-reactive CD8⁺ T cells from HCC patients, related to the UMAP plot in [Figure 5A](#). The shared clonotypes representing at least two clones in the TME were included for this plotting. The numbers of shared clonotypes for each patient are listed at the bottom of the plot. The paired TCR sequences of shared clonotypes are listed in [Table S2](#).

(I) Dot plot representing the relative average activity of a selected subset of marker genes across all clusters in [Figure 5A](#). Dot color represents the average gene expression level relative to all clusters and dot size corresponds to the percentage of cells with detected activity of indicated genes for each cluster, related to [Figure 5A](#).

(J and K) Representative FACS plots of mouse β chain expression (indicating the expression of selected TCR clones) in TCR-transduced (GFP⁺) CD8⁺ T cells (left) and the expression pattern of 4-1BB in TCR-transduced (GFP⁺) CD8⁺ T cells (right) as in [Figure 5G](#). Numbers are frequencies.

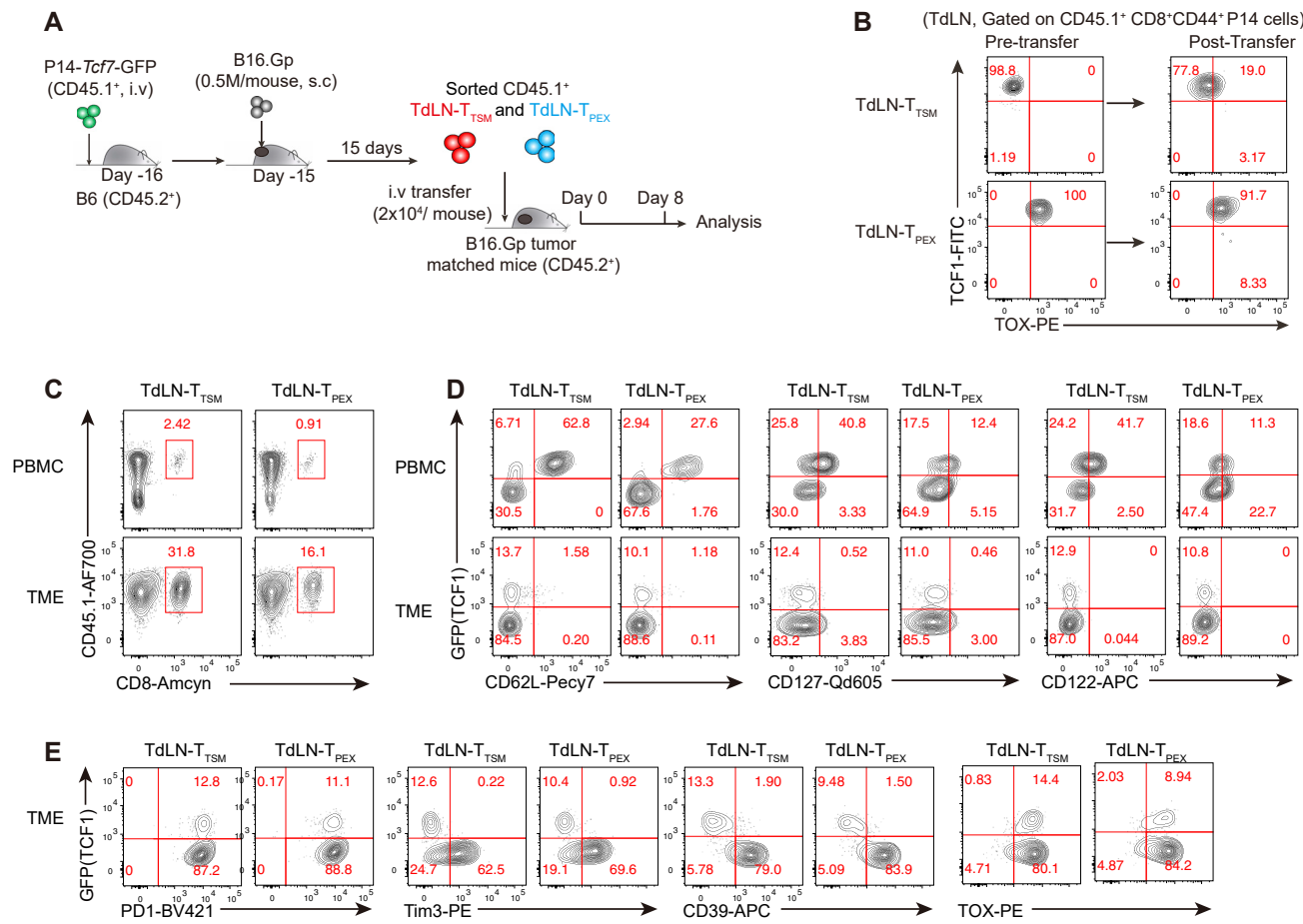


Figure S6. TdLN-derived T_{TSM} cells differentiate into TdLN-T_{PEX} cells, related to Figure 7

(A-E) Naive P14-Tcf7-GFP (CD45.1⁺CD44⁻) cells were adoptively transferred to CD45.2⁺B6 mice, then recipient mice were inoculated with B16.Gp tumor cells. At day 15, CD45.1⁺CD8⁺CD44⁺GFP⁺PD1^{lo} TdLN-T_{TSM}-P14 and CD45.1⁺CD8⁺CD44⁺GFP⁺PD1^{int} TdLN-T_{PEX}-P14 cells were isolated and further transferred (2 × 10⁴ cells/mouse, i.v.) to recipient mice inoculated with B16.Gp previously. P14 cells from the TdLN, PBMC, and tumor mass (TME) were analyzed at day 8 post transfer. (A) Experiment design. (B) The co-expression pattern of TCF-1 and TOX of TdLN-T_{TSM} or TdLN-T_{PEX} derived P14 progenies before transfer (left) or in TdLN of recipient mouse 8 days after transfer (right). (C) Representative flow cytometric plots of transferred CD45.1⁺ P14 cells in PBMC and TME of recipient mice. (D and E) Flow-cytometry analyses of GFP (TCF-1) versus the expression of indicated memory markers (D) or inhibitory markers (E) in CD45.1⁺CD44⁺ donor-derived P14 cells in different compartments of host mice.

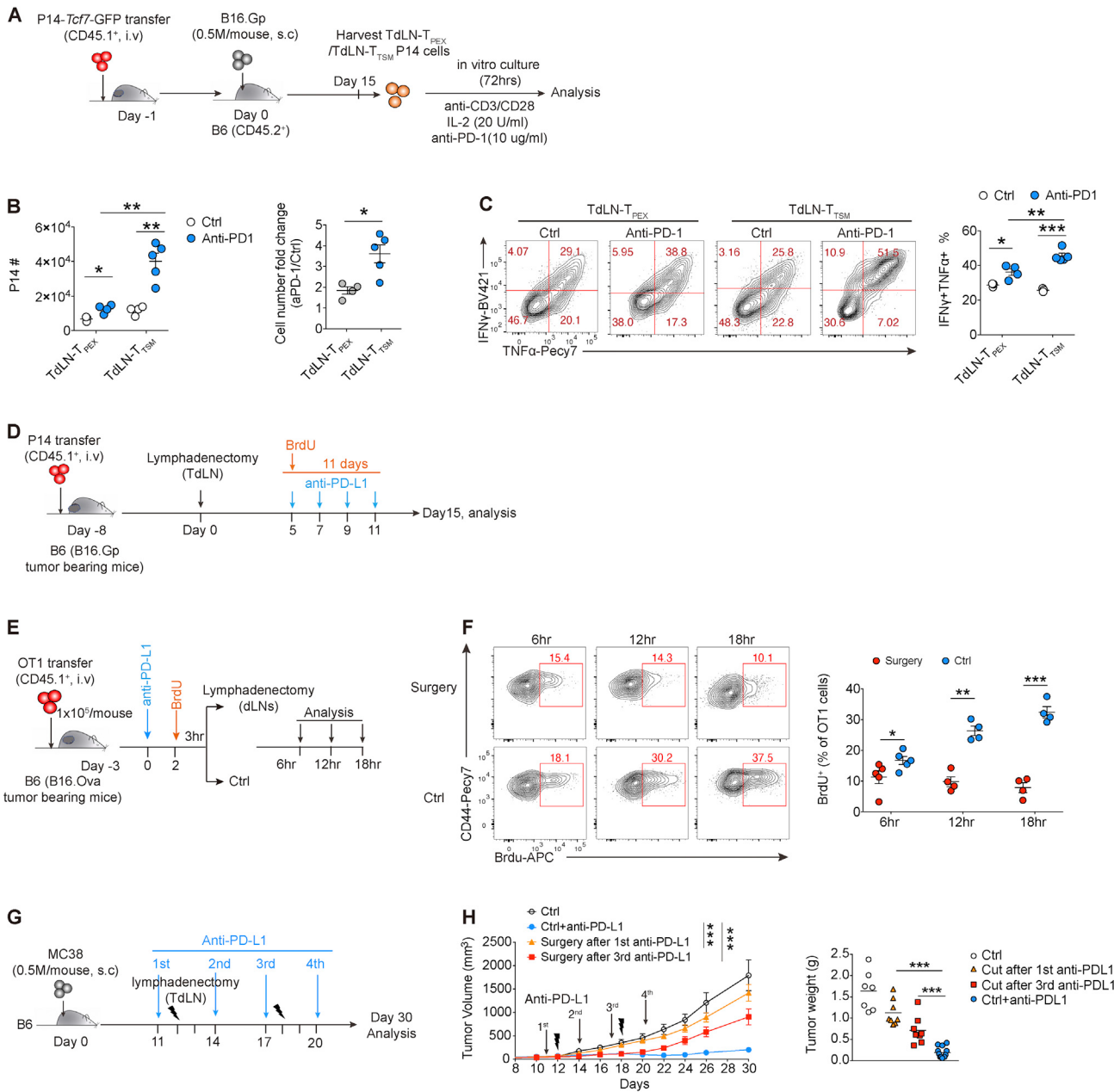


Figure S7. T_{TSM} cells in TdLN are the predominant targets of PD-1/PD-L1 ICB in exerting its therapeutic effects, related to Figure 7

(A–C) Naive *Tcf7*-GFP P14 cells were transferred to B6 mice, inoculated with B16.Gp tumor cells 1 day later. On D15, TdLN-T_{TSM} and TdLN-T_{PEX} cells were sorted and cultured *in vitro* with the presence of anti-CD3 (2 µg/ml)/CD28 (0.5 µg/ml), IL2 (20 U/ml), and anti-PD-1 antibody (10 µg/ml) for 72 h. (A) Experiment design. (B) Statistical analysis of the number of TdLN-T_{TSM} and TdLN-T_{PEX} P14 cells treated with or without anti-PD-1 ($n \geq 3$ /group). (C) Flow-cytometry analyses of the co-expression of IFN- γ and TNF- α in cultured P14 cells from indicated groups. The frequencies of IFN- γ ⁺TNF- α ⁺ P14 cells were summarized beside. $n \geq 3$ /group.

(D) Experiment design: P14 cells were transferred to B16.Gp tumor-bearing mice, 8 days later, both sides of inguinal lymph nodes of recipient mice were removed through lymphadenectomy, then anti-PD-L1 or control immunoglobulin were administrated intra-peritoneally at indicate time points. Mice were treated with 1.5 mg of BrdU i.p. daily since day 5 for 11 days prior to tissue harvest and analysis. P14 cells in the dLNs, PBMC, and TME were analyzed on day 15 post lymphadenectomy surgery, related to Figures 7G and 7H.

(E and F) B16.OVA bearing B6 mice were first treated with one dose of anti-PD-L1 blocking antibody (300 µg/mouse) 3 days after OT1 cell transfer, then these mice received i.p. administration of BrdU 2 days after anti-PD-L1 treatment. 3 h later, half of the mice received lymphadenectomy of bilateral dLNs (surgery) while others received sham-operation (Ctrl), and BrdU⁺ OT1 cells in TME were analyzed afterward at indicated time points. (E) Experiment design. (F) Left: flow-cytometry analyses of BrdU⁺ cells in TME-derived CD44⁺ OT1 cells from indicated group as described in (E). Numbers are frequencies of indicated population. Right: statistical analysis of the proportion of BrdU⁺ OT1 cells in TME of mice from surgery or control group at indicated time points ($n \geq 4$ /group).

(legend continued on next page)

(G and H) MC38 cells were s.c. implanted to B6 mice, followed by 4 shots of anti-PD-L1 administration from day 11 to day 20 (every 3 days). Lymphadenectomy surgery was conducted after 1st or 3rd shot of anti-PD-L1 as indicated. Tumor volume were measured every 2 days. Mice were sacrificed, and tumor weight were measured at day 30 (endpoint) (G). Tumor volume curve and tumor weight for indicated group are summarized in (H) ($n \geq 6/\text{group}$). * $p < 0.05$, ** $p < 0.01$, and *** $p < 0.001$ versus control, unpaired two-tailed Student's t test (B, right panel of C, right panel of F), one-way ANOVA (right panel of H), or two-way ANOVA analysis (left panel of H). Data are representative of ≥ 2 independent experiments (mean \pm SEM).